A45-Shielded UAS Operations: Detect and Avoid (DAA): Task 3 Analysis of DAA Requirements and Obstacle Avoidance Requirements

March 27, 2024

NOTICE

LEGAL DISCLAIMER

Technical Report Documentation Page

1. Report No. A45_A11L.UAS.87	2. Government Accession No.	3. Recipient's Catalog No.
4. Title and Subtitle A45-Shielded UAS Operations: Detect and Avoid (DAA): Task 3 Analysis of DAA Requirements and Obstacle Avoidance Requirements		5. Report Date March 27, 2024 6. Performing Organization Code
7. Author(s) Naima Kaabouch: https://orcid.org/0000-0002-1333-3352 Hever Moncayo: https://orcid.org/0000-0001-5088-9715		8. Performing Organization Report No.
9. Performing Organization Name and Address University of North Dakota (4201 James Ray Dr. Stop 8367, Grand Forks, ND 58202) Kansas State University () Embry Riddle Aeron. Univ. (1 Aerospace Boulevard, Daytona Beach, FL 32114)		10. Work Unit No. (TRAIS) 11. Contract or Grant No. 15-C-UAS
12. Sponsoring Agency Name and Address U.S. Department of Transportation Federal Aviation Administration Washington, DC 20591		13. Type of Report and Period Covered Interim Report 14. Sponsoring Agency Code 5401

15. Supplementary Notes
Conducted in cooperation with the U.S. Department of Transportation, Federal Highway Administration, ASSURE UAS Center of Excellence.

16. Abstract
The demand for Beyond Visual Line Of Sight (BVLOS) operations using Uncrewed Aircraft Systems (UASs) is high because they produce numerous benefits. These benefits have driven increased pursuit of BVLOS capabilities, with much of the focus being on small UAS (sUAS) owing to reduced risks (air and ground collision risks) associated with such aircraft. One approach that can enable sUAS BVLOS operations is shielded operations, wherein a sUAS is operated near objects such as buildings, powerlines, etc. Such operations are expected to produce a safety benefit since Crewed Aircraft (CA) will generally maintain separation from such objects. They can also involve increased risks, however, that are associated with operation near shielding objects.
Electric and Magnetic Fields (EMF), airflow, and GPS hazards are evaluated using multiple models. The EMF model produces solutions to Maxwell's equations, while the airflow models utilize AirSim, which includes airflow impacts on aircraft. GPS hazards were modeled using a framework comprised of seven primary components.
Estimated safe distances are provided for single powerlines, multiple powerlines, short circuits, and transformers. Safe distances are generally less than ~11 m, but can be as large as 50 m for short circuits.
A multicopter's ability to maintain course or at least resist further displacement after the initial onset of wind effects is predictable and enables provision of guidelines on minimum distances from hazardous areas. Exceedance of a mutlicopter's wind limit results, as expected, in undesirable outcomes. Wake vortex effects for multicopters are small except when interacting with very large CA.
Autonomous missions requiring high levels of navigation accuracy require healthy Global Positioning System (GPS) satellite geometries, which generally means connection with more than seven satellites. Numerical simulations revealed that among the various GPS signal degradation types, those posing the highest risks, in descending order, were dropouts, jamming, and a reduced number of satellites (down to four). Thus, GPS integrity should be monitored and addressed for operations where these effects may be realized. Given the scenario considered herein, this is especially true for operations at low altitudes ($\leq$ 16 m) and close to buildings (e.g., within 6 m).

17. Key Words	18. Distribution Statement
Detect and Avoid Powerline inspections Transformer inspections Wind impacts Wake vortex GPS degradation	This document is available to the U.S. public through the National Technical Information Service (NTIS), Springfield, Virginia 22161. This document is also available from the Federal Aviation Administration William J. Hughes Technical Center at actlibrary.tc.faa.gov.

19. Security Classif. (of this report)	20. Security Classif. (of this page)	21. No. of Pages	22. Price
Unclassified	Unclassified	102	

Form DOT F 1700.7 (8-72) Reproduction of completed page authorized

TABLE OF CONTENTS

TABLE OF FIGURES

TABLE OF TABLES

TABLE OF ACRONYMS

Acronym	Meaning
2D	Two Dimensional
3D	Three Dimensional
ASSURE	Alliance for System Safety of UAS Through Research Excellence
BVLOS	Beyond Visual Line Of Sight
CA	Crewed Aircraft
CAD	Computer-Aided Design
CDF	Cumulative Distribution Function
CMC	Code-Minus-Carrier
CONOPS	Concept Of Operations
DAA	Detect and Avoid
DOP	Dilution of Precision
EHV	Extra-High Voltage
EKF	Extended Kalman Filter
EM	electromagnetic
EMF	Electric and Magnetic Field
EMI	ElectroMagnetic Interference
EPA	Environmental Protection Agency
ESA	European Space Agency
FAA	Federal Aviation Administration
FEM	Finite Element Method
FTP	Flight Test Plan
GNSS	Global Navigation Satellite System
GPS	Global Positioning System
HS	Harmonized Steel
KE	Kinetic Energy
NASA	National Aeronautics and Space Administration
PDF	Probability Density Function
PDOP	Position Dilution of Precision
RF	Radiofrequency
ROS	Robot Operating System
sAAT	sUAS Airworthiness Assessment Tool
SE	Simulation Environment
sUAS	Small Uncrewed Aircraft System
SW	Shield Wires
UA	Uncrewed Aircraft
UAS	Uncrewed Aircraft System
UEE	User Equivalent Error

EXECUTIVE SUMMARY

The demand for Beyond Visual Line Of Sight (BVLOS) operations using Uncrewed Aircraft Systems (UAS) is high. Associated benefits have driven increased pursuit of BVLOS capabilities, with much of the focus being on small UAS (sUAS). One approach that can enable sUAS BVLOS operations is shielded operations, wherein a sUAS is operated near objects such as buildings, powerlines, etc. Operation near such objects is assumed to produce a safety benefit relative to encounters with Crewed Aircraft (CA) since CA will generally maintain separation from such objects. Such operations can involve increased risks, however. These include Global Positioning System (GPS) degradation, Electric and Magnetic Fields (EMFs) that cause system failures, turbulent flow that results in loss of controlled flight, etc.

EMF, airflow, and GPS hazards are evaluated using multiple models. The EMF model produces solutions to Maxwell's equations using the Finite Element Method (FEM), while the airflow models utilize AirSim, a model that incorporates, among other physical effects, airflow impacts on aircraft. GPS hazards were modeled using a framework comprised of seven components. In this, Matlab and Simulink were interfaced with Gazebo for visualization.

The minimum safe distance to a powerline depends on the UAS' ability to withstand electromagnetic interference and can be derived from results in Section **Error! Reference source not found.**. For example, the estimated safe distances for single powerlines were less than ~11 m in both the horizontal and vertical directions for the lowest dangerous electric and magnetic field thresholds. Depending upon UAS EMF tolerance, they could be flown much closer (e.g., within 5 m). The presence of a second line generally reduced the strength of the magnetic field near one of the powerlines, although increases can occur between powerlines (see Section **Error! Reference source not found.**). During short circuits, EMFs can be much larger than during normal operations, resulting in safe distance estimates that can range from 15-50 m (can be derived in a similar fashion as for single powerlines using the results in Section **Error! Reference source not found.**). For transformers considered herein, estimated safe distances are < 5 m in the horizontal and vertical directions (see Section **Error! Reference source not found.**).

A multicopter's ability to maintain course or at least resist further displacement after the initial onset of wind effects depends upon its configuration, performance, and autopilot. In the case of the simulated multicopter, it is predictable and enables provision of safety guidelines (the amount of acceptable displacement for the tested configuration can be derived from the results in Section **Error! Reference source not found.**). Exceedance of a multicopter's wind limit results in undesirable outcomes. Wake vortex effects for multicopters are small except when interacting with very large CA (see Section **Error! Reference source not found.**).

Autonomous missions requiring high levels of navigation accuracy require healthy GPS satellite geometries, which generally means connection with more than seven satellites. Numerical simulations revealed that among the various GPS signal degradation types, those posing the highest risks, in descending order, were dropouts, jamming, and a reduced number of satellites (down to four). Thus, GPS integrity should be monitored and addressed for operations where these effects may be realized. Given the scenario considered herein, this is especially true for operations at low altitudes (≤ 16 m) and close to buildings (e.g., within 6 m).

The presence of multiple hazards should be addressed in a combined standoff distance and may usually be found by just summing the individual distances. The EMF safe distances represent the base distance offsets, to which is added distances resulting from GPS uncertainty and deviations due to wind or wake vortices.

1 INTRODUCTION

The demand for Beyond Visual Line Of Sight (BVLOS) operations using Uncrewed Aircraft Systems (UAS) is high. Such operations produce numerous benefits, including humanitarian and economic (e.g., UAS BVLOS Aviation Rulemaking Committee 2022). Humanitarian benefits include improving health outcomes (including saving lives), while economic benefits include reduced costs and increased efficiency associated with numerous use cases (inspection, package delivery, etc.). These benefits have resulted in increased pursuit of BVLOS capabilities, with much of the focus being upon small UAS (sUAS) owing to reduced risks (air and ground collision risks) associated with such aircraft.

One approach that can enable sUAS BVLOS operations is shielded operations, wherein a sUAS is operated near objects such as buildings, powerlines, etc. Operation near such objects is assumed to produce a safety benefit relative to encounters with Crewed Aircraft (CA) since CA will generally maintain separation from such objects. Such operations can involve increased risks, however, that are associated with operation near shielding objects. These include Global Positioning System (GPS) data degradation that result in collisions with objects such as buildings, Electric and Magnetic Fields (EMFs) that cause system failures and subsequent collisions, turbulent flow that results in loss of controlled flight and potential collisions with people, etc.

The Alliance for System Safety of UAS Through Research Excellence (ASSURE) project A45-Shielded UAS Operations: Detect and Avoid (DAA) (A45) involves numerous tasks associated with shielded operations. Herein, the focus is on analysis of DAA requirements and obstacle avoidance requirements. More specifically, this effort involves development of simulation environments that enable assessment of risks associated with shielded operations and potential solutions for those risks.

2 TASKS

Tasks in A45 include:

0. Project Management:
   Management of the overall project, including project kick-off, the project research task plan, technical interchange meetings, program management reviews, leadership briefings, and project close out.
1. Literature Review and Risk Identification
   A comprehensive literature review of shielding research, including terminology, shielding benefits, and identification of risks associated with shielded operations.
2. Shielding Classes, Risk Assessments, and Listing of Mitigations
   a. Shielding Classes/Categories
   b. Hazard Analysis

   Identification/creation of shielding classes/categories and completion of a hazard analysis in which risks and risk mitigations are identified.
3. Analysis of DAA Requirements and Obstacle Avoidance Requirements
   Development of a simulation environment that will allow assessment of risks and potential solutions identified in Tasks 1 and 2. Numerical simulations will be performed to analyze the competing shielding requirements to manage risks with flight near

obstacles and to manage risks with CA. Risks evaluated include those associated with the type of operation, UAS characteristics, type of obstacle, and type of intruder.

4. Flight Test Plans
   Development of Flight Test Plans (FTPs) for the most promising types of shielded operations. Operations are based upon industry needs, need to evaluate performance based on previous findings, and the viability of performing such tests.
5. Tests and Reports
   Tests and demonstrations conducted using the developed FTPs from Task 4 and documentation of the approach and outcomes. Reports interpret the significance of tests and outcomes and the degree to which results refine and validate previous shielding recommendations.
6. Standards Development
   Participation in relevant standards development efforts. Results from A45 will be used to enhance those efforts by providing relevant research results.
7. Final Briefing and Final Report
   Summarization of all of the previous papers and reports (excluding meeting notes) into a final report package for the overall project.
8. Peer Review
   A peer review of the final report.

The focus herein is Task 3. In this task, the A45 team developed simulation environments that enable assessment of risks and potential mitigations for these risks. These were developed to evaluate

- Impacts of the type of shielded environment (e.g., urban vs rural)
- Impacts of the type of UAS (fixed- vs rotary-wing)
- Impacts of shielding obstacle type (buildings, powerlines, etc.)
- Impacts of intruder (CA) type
- DAA strategies (exit shielded operations to maneuver, maneuver while staying within shielded environment, etc.)
- Legal questions (liability and legal impacts)

Legal questions were addressed in the A45 literature review (Sugumar et al. 2021). Thus, the focus herein is on the other five topics.

3 CONCEPT OF OPERATIONS (CONOPS)

For this analysis, important CONOPS were identified to provide context for simulations. This also served to bound the effort, as simulation/evaluation of all possible combinations (environment + type of UAS + shielding obstacle type + intruder encounter scenarios + DAA strategies) exceeds the resources allocated to this effort.

3.1 Linear Infrastructure

Significant effort has been directed at using Unmanned Aircraft (UA) to perform tasks associated with linear infrastructure, such as powerlines and pipelines. While these tasks can be varied, the focus is generally on inspection.[1] The desire, generally, is to fly BVLOS over significant distances to capture data related to infrastructure (e.g., Bruggeman et al. 2011; Matikainen et al. 2016). Given that the EMF hazard associated with flight near powerlines is an additional hazard relative to other operations associated with linear infrastructure (e.g., pipeline inspection), flights near powerlines are a focus herein.

3.2 Package Delivery

Package delivery has also received significant attention.[2] Much of the focus for this use case is in urban and suburban environments (Benarbia and Kyamakya 2022). Thus, flights in these types of environments are considered herein.

4 LINEAR INFRASTRUCTURE—POWERLINES

4.1 Electromagnetic Fields and Safe distances

UAS are used for aerial inspections of power distribution infrastructure to assess their conditions and to detect physical damage to components such as conductors, wires, towers, and insulators. These power elements emit a certain level of low-frequency EMFs. Among these elements, powerlines and distribution transformers emit considerably higher EMFs than other grid components. Inspecting these elements put UAS in EMFs that can cause errors in GPS receivers, magnetometers, transmitted data, etc. As an example of a significant hazard outcome, GPS and magnetometer errors could cause a UAS to crash into transformers and possibly create explosions, as these transformers are mostly oil-immersed.

The objective is to develop a simulation environment that assesses risks associated with flights during the inspection of power systems, Extra-High Voltage (EHV) transmission lines, and transformers. This is performed in normal operations and in the presence of faults, wind, and wake vortices created by CA.

4.1.1 Single Powerlines

Significant research has been conducted over the last decade to understand the effects of EMFs on UAS during power line inspections. For example, Kim et al. (2022) highlighted that different UAS brands and models were susceptible to various ElectroMagnetic Interference (EMI). The authors concluded that the onboard sensor package is the most susceptible to EMI compared to other parts of the UAS. Zhang et al. (2019) established that electric fields above 50 kV m^{-1} led to UAS instability, suggesting a threshold for stable UAS operation. They also highlighted the qualitative effects of EMFs on UASs, pointing to the need for quantitative data for safety measures. They stated that magnetic fields over 180 μT made UASs drift towards power lines, affecting the magnetometer function; however, their research did not address the response of different UAS models to these disturbances or their operational implications. Furthermore, the United States Department of Homeland Security cited a similar threshold of 50 kV m^{-1} (National Coordinating Center for Communications 2019) for modeling infrastructure resilience against electromagnetic pulses.

[1] A Google Scholar search on 29 December 2022 using the words “infrastructure inspection drones” produced ~8,700 results since the year 2021.
[2] A Google Scholar search on 29 December 2022 using the words “drone package delivery” produced ~11,200 results since the year 2021.

Lusk and Monday (2017) studied small UASs in the electric utility industry and reported EMI disruptions within 2–4 m of active equipment but none beyond 10 m. This study highlighted that various UASs, sensors, and infrastructure combinations can show distinct EMF behaviors affecting missions. They did not, however, specify the type of sensor susceptible to EMI interference or the movement of the UAS during the inspection. Chen et al. (2020) simulated the effects of a 500 kV tower EMFs on UASs. They found significant electric field changes, with UASs withstanding up to 300 kV m^{-1} before failure. Based on their simulations, they concluded that for distances of 4.5 m or greater, the UAS flight control system will work normally. Park et al. (2020) assessed EMI effects on UASs during inspections of 345 kV and 765 kV power lines in South Korea. Their tests revealed interference within 15 m for 345 kV lines and 30 m for 765 kV lines; therefore, they set 30 m and 45 m safety distances, respectively, to avoid GPS and sensor disruptions.

Estimating EM fields around powerlines has been mostly performed a few meters from the ground. Little work has been performed on EM environments around EHV transmission lines when performing UAS inspections. In this work, the design and development of a robust simulation environment was performed to assess safe distances during UAS inspections of EHV transmission lines.

4.1.1.1 Methodology

For this investigation, three-phase EHV 345, 500, and 765 kV powerlines with ground wires were considered, as shown in Figure 1. The 345 kV line comprises two identical 3-phase circuits with two conductors per phase. The phase-conductors were type 636 CAA-26/7 MCM (e.g., https://www.induscabos.com.br/portfolio-item/fios-e-cabos-de-aluminio-nu-caa-acsr/?lang=en), 240 mm^2 each, and the Shield Wires (SW1 and SW2) were made of 7-wire Harmonized System (HS) galvanized steel.[3] The 500 kV and 765 kV lines had a single horizontal circuit with two 32.2 mm-spaced conductors per phase and four 32 mm-spaced conductors per phase, respectively. The phase-conductors were type 795 MCM, and the shield wires (SW1 and SW2) were made of 9-wire HS galvanized steel (Brown 2013; El Dein 2013; Bühringer 2010).

[3] MCM is a measurement for wire gauge that stands for thousands of circular mils (1 mil = 1/1000 in). 1 MCM = 0.5067 mm^2.

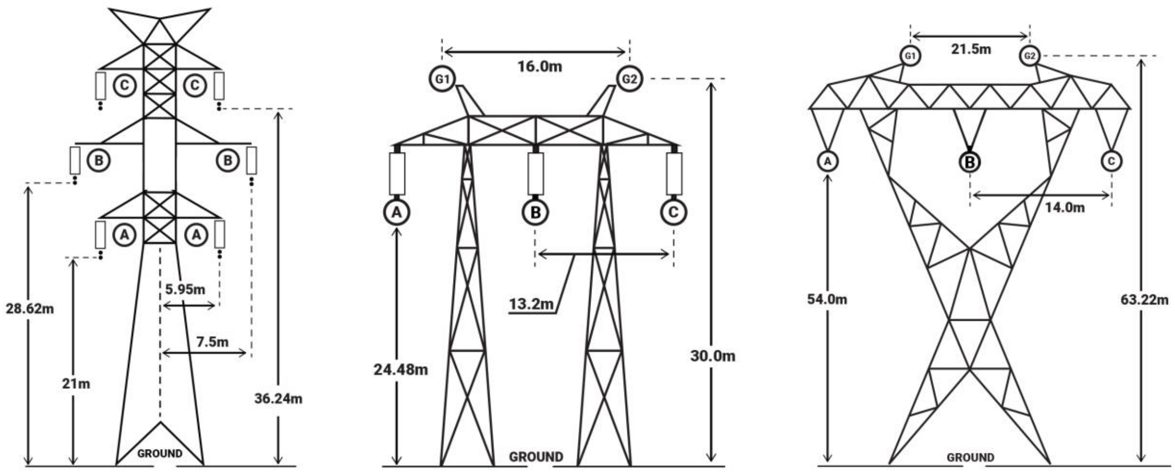

Figure 1. Standard dimensions for 345, 500, and 765 kV powerlines (Brown 2013; El Dein 2013; Bühringer 2010).

Table 1 lists the characteristics of each power line, including voltage and current. The most common 345 kV conductor configuration, which was used for this work, is termed "Untransposed."

Table 1. Characteristics of the EHV transmission lines (Siemans 2017, chapter. 3).

Nominal Voltage Level (kV)	345	500	765
Highest system current rating at 80C (kA)	1.29	2.58	4.16
Phase angle (deg.)	C-C: 0-240	A: 0	A: 0
	B-B: 120-120	B: 120	B: 120
	A-A: 240-0	C: 240	C: 240
	SW: 0	SW: 0	SW: 0
Nominal cross-section (mm²)	Bundle 2×240	Bundle 2×560	Bundle 4×560
Conductor diameter (mm)	2×21.9	2×32.2	4×32.2
Shield wires diameter (mm)	6	9	9

The mutual relationship and properties of electric fields and magnetic fields can be described by Maxwell's four basic equations (Lunca et al. 2021). These equations are based on Ampere's law, Faraday's law of induction, Gauss' law, and Gauss' law for magnetism:

$$\nabla \times \bar{E} = -\frac{\partial \bar{B}}{\partial t}, \tag{1}$$

$$\nabla \times \bar{H} = \bar{J} + \frac{\partial \bar{D}}{\partial t}, \tag{2}$$

$$\nabla . \bar{D} = \rho, \tag{3}$$

and

$$\nabla . \bar{B} = 0, \tag{4}$$

where $\bar{E}$, $\bar{H}$, $\bar{J}$, $\bar{D}$, $\bar{B}$, and ρ are the electric field strength, magnetic field strength, current density, dielectric flux density, magnetic flux density, and electric charge density, respectively. Taking the curl on both sides of (2) produces the electromagnetic wave equation in terms of only $\bar{H}$

$$\nabla^2\bar{H} - \varepsilon\mu\frac{\partial^2\bar{H}}{\partial t^2} = -\nabla\times\bar{J}, \tag{5}$$

where μ is the magnetic permeability and ε is the dielectric permittivity of the media.

Herein, each transmission line can be considered as a linear, homogeneous, isotropic, lossy dielectric medium with conductivity σ and no free charges, such as ρ=0 and $\bar{J} = \sigma\bar{E}$ (Lunca et al. 2021); therefore, (5) can be expressed as

$$\nabla^2\bar{H} - \varepsilon\mu\frac{\partial^2\bar{H}}{\partial t^2} - \sigma\mu\frac{\partial\bar{H}}{\partial t} = 0. \tag{6}$$

Equation (6) is a vector wave equation in a conducting medium. The magnetic potential field distribution can be acquired through the numerical solution of (6) with methods such as the Finite Element Method (FEM).

To calculate the electromagnetic fields, the team used QuickField, which is a finite element analysis software package for EM fields, stress, and thermal analysis (Tera Analysis Ltd. 2018). This software solves Maxwell's equations to calculate EM fields near transmission lines. QuickField divides the problem into several smaller parts, known as finite elements, characterized by their simple structure compared to the original system. The FEM solving process begins with dividing the solution region into finite-number subregions known as region discretization. Each subregion or element is then analyzed, and an equation is developed. The next step is element assemblage, which involves assembling all of the equations from each subregion. Finally, the generated equation system is solved. The gradient expression is used to calculate the electric field intensity within each element using

$$E_m = (-\nabla.V)_m = -\sum_{j=1}^{n} V_j f_j^m, \tag{7}$$

where V_j is the electric potential of node j, r is any point on the proposed region, and f_j is the shape function with the property that any $f_j(r)$ is equal to 1 at the location of node j and zero at all other nodes (Virjoghe et al. 2012).

For this simulation, the transmission line conductors were assumed as infinitely long, straight, parallel to each other, and parallel to the ground. The active conductors were modeled as simple copper cylinders with an electrical conductivity of 6 S m^{-1}. The scalar electric potential along the semicircular boundary and at the ground level was zero. The transmission line was placed above ground with a soil electrical conductivity of 0.02 S m^{-1} and magnetic permeability of 1. The applied boundary condition was half balloon type (R = 320 m), which attempts to simulate space extending to infinity (Virjoghe et al. 2012). Each powerline simulation required more than a half-million mesh elements for satisfactory analysis and good symmetry.

4.1.1.2 Results

The EM fields were calculated for three types of flights: vertical (*y*), horizontal (*x*), and circular (*R*) (Figure 2). The figure on the left depicts the UAS moving in the *x* or *y* direction, and the figure on the right depicts the UAS moving around the transmission line at a fixed radius *R*.

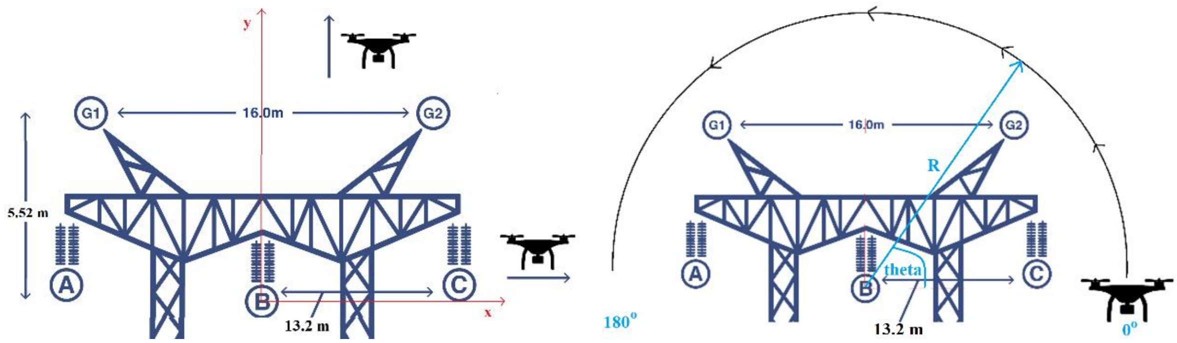

Figure 2. Direction of motion for *x, y,* and radius scenarios.

4.1.1.2.1 Electric Field

Simulation results are illustrated in Figures 3-6. Figures 3a and 3b depict the electric field as a function of *x* and *y*, respectively, for the three powerline types. As expected, the electric field is very high around the phase conductors, and decrease exponentially as the UAS moves away from the powerlines. Due to the geometry of the 345 kV powerline, the electric field increases at 5 m with a maximum at 7.5 m, followed by a sharp drop.

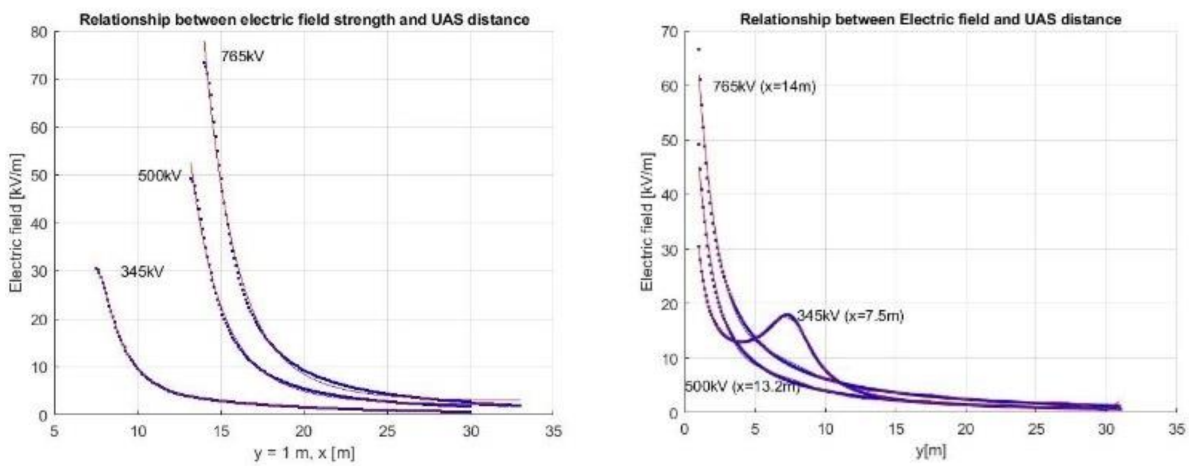

a) b)

Figure 3. Electric field as a function of *x* (a; horizontal movement) and *y* (b; vertical movement).

Figure 4 depicts the distribution of electric fields for different heights for horizontal movement above and below the centerline of the three phases or at the centerline of phase B for the double-circuit configuration. As expected, the electric field reaches its maximum at the horizontal coordinates of the phases and drops as the UAS moves vertically from the powerlines. For instance, for y = ±1 m, the peak electric field strength is at its maximum at 30, 51, and 78 kV m^{-1} for the 345, 500, and 765 kV transmission lines, respectively. At y = ±10 m, the peak electric field strength decreases to 0.6 kV, 3.6 kV, and 5.6 kV m^{-1}, respectively.

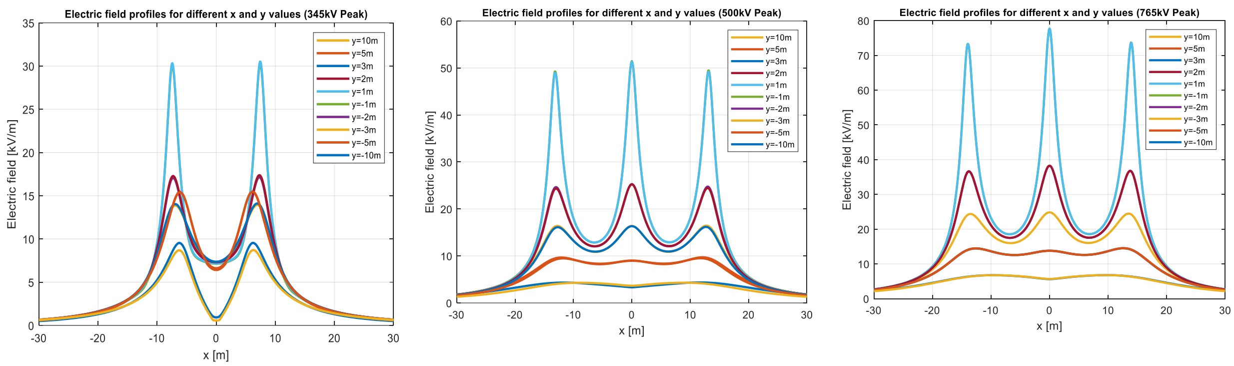

a) b) c)

Figure 4. Lateral profiles of electric fields for heights between -10 and 10 m and for the 345 kV (a), 500 kV (b), and 765 kV (c) powerlines.

Figure 5 presents the 3D mapping of the electric field strength for the three powerline types. A concentrated electric field is clearly produced around the phase of the conductor surface. This electric field gradually decreases as the UAS moves away from the phase conductors. An extra degree of cancellation can be observed for the 345 kV transmission line between the fields.

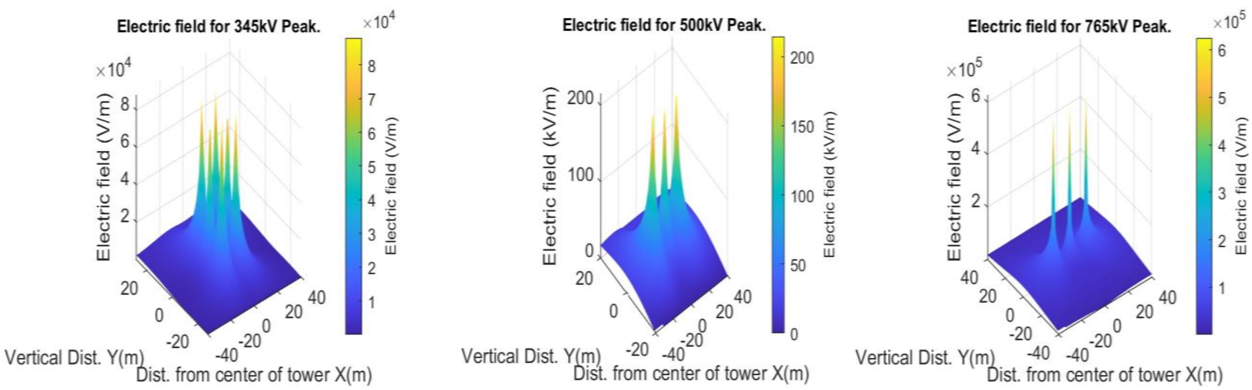

Figure 5. Three-dimensional plot of the electric field for the three (345 kV—left; 500 kV—middle; 765 kV—right) powerline levels.

Figure 6 shows the electric field intensity for four different radius values for each of the powerline types. The UAS path began on the right side of the transmission line and ended on the left. For each figure, the left side of plots corresponds to an angle, θ, of 0°, and the right side corresponds to 180°. For these two angles, the electric field values are higher for the 500 kV and 765 kV powerlines. For the 345 kV powerline, the electric filed presents two maxima at 40° and 140°, and a minimum at about 90°. In general, the electric field decreases as the radius increases. For circular flights, the highest field values correspond to an approximate radius of 15 m due to the shape of towers.

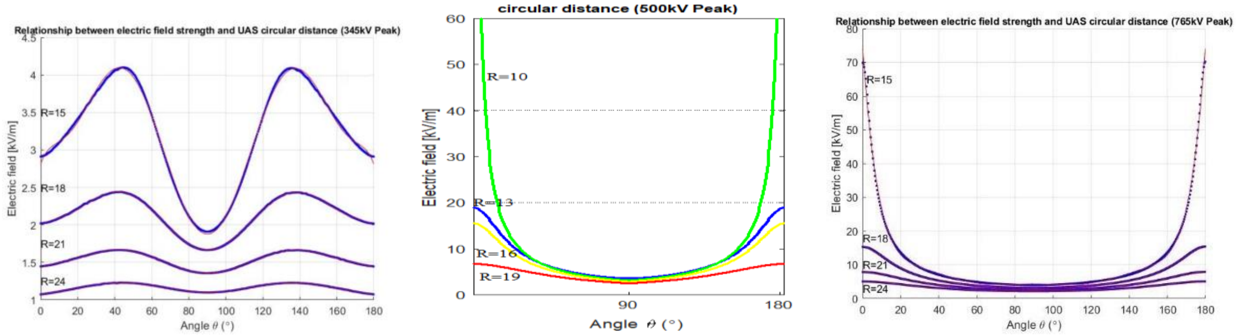

Figure 6. Electric field for different angles and at four different radius values. The left side of plots corresponds to an angle, θ, of 0°, and the right side corresponds to 180°.

4.1.1.2.2 Magnetic Field

Simulation results are illustrated in Figures 7-10. Figure 7 depicts the resultant magnetic field as a function of *x* and *y*, respectively, for each of the three powerline types. These figures exhibit similar profiles as with the electric fields of Figure 3; however, the magnetic field values are much higher.

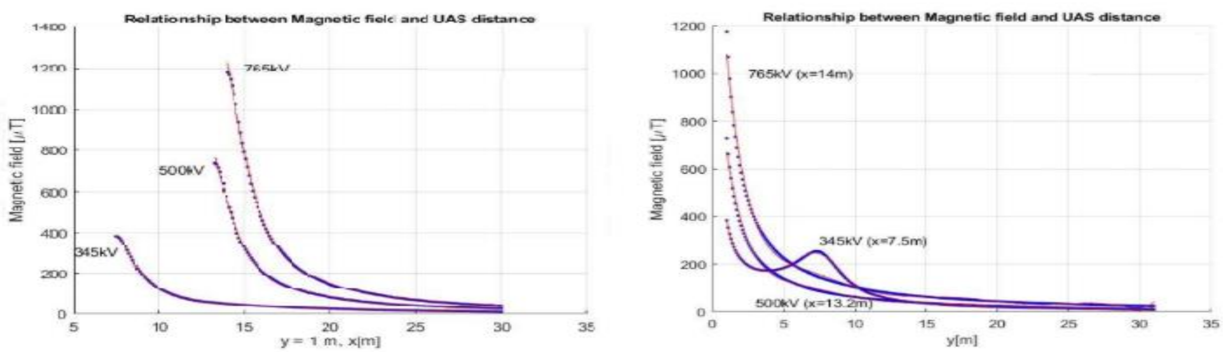

Figure 7. Magnetic field as the UAS moves horizontally (left) and vertically (right).

Figure 8 shows the magnetic field distribution for horizontal movement above and below the centerline of the three phases or at the centerline of phase B for the double-circuit configuration. The magnetic field presents maxima at the horizontal coordinates of the phases and drops as the UAS moves horizontally and vertically from the powerlines. For instance, for y = ±1 m, the magnetic field is at its maximum at 384 µT, 728 µT, and 1173 µT for the 345 kV, 500 kV, and 765 kV transmission lines, respectively. For *y* = ±10 m, the magnetic field decreases to 8.9 µT, 59 µT, and 99 µT, respectively.

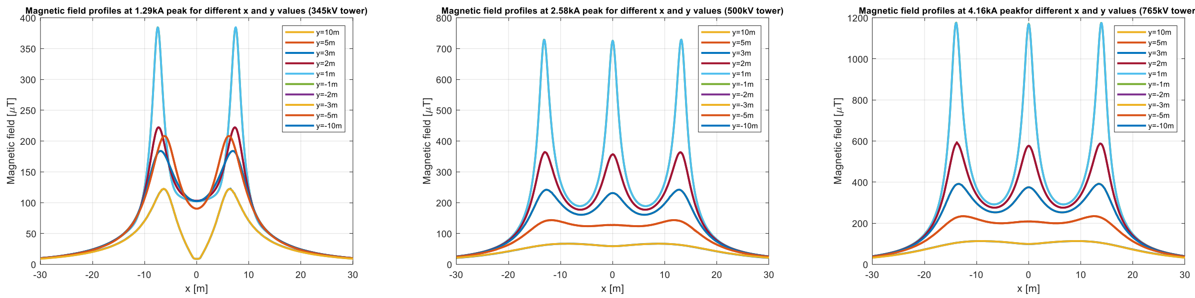

a) b) c)

Figure 8. Lateral profiles of the magnetic field for heights between -10 and 10 m for 345 kV (a), 500 kV (b), and 765 kV (c) powerlines.

Figure 9 depicts the magnetic field for circular flights around powerlines at four different radius values. Similar to the electric field case, the UAS movement began on the right side of the transmission line (0°) and ended on the left side (180°). For these two angles, the magnetic field values are higher for the 500 kV and 765 kV powerlines. For the 345 kV powerline, the magnetic field presents two maxima at 40° and 140° and a minimum at approximately 90°. In general, the magnetic field decreases as radius increases. The highest field values correspond to an approximate radius of 15 m due to the shape of the towers.

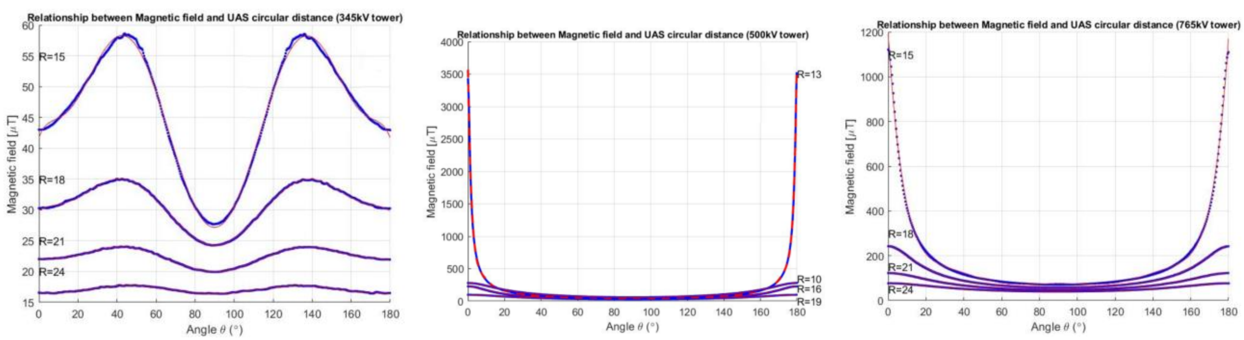

Figure 9. Magnetic field as a function of angle and at four different radius values for the 345 kV powerline (left), 500 kV powerline (middle), and 765 kV powerline (right).

Figure 10 provides 3D mapping of the magnetic field intensity. Similar to the electric field case, the magnetic field's concentration is clearly produced around the conductors of the phases. As the UAS moves away from these phase conductors, the magnetic field gradually decreases.

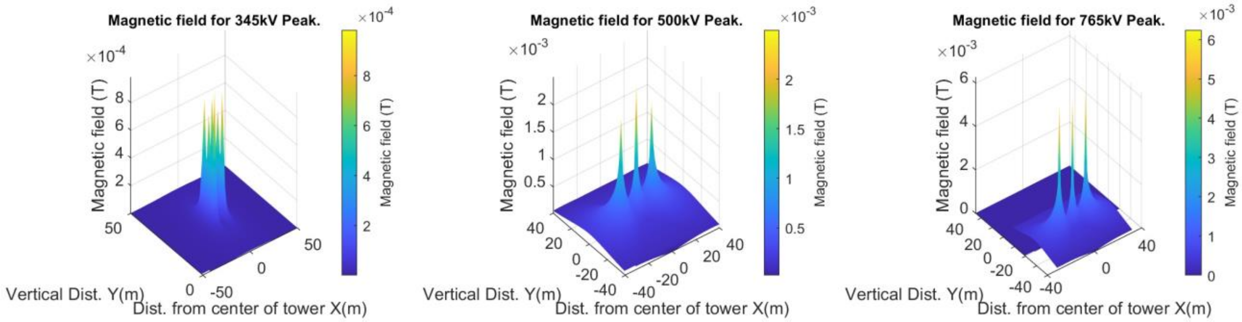

Figure 10. Three-dimensional plot of magnetic field intensity for the three (345 kV—left; 500 kV—middle; 765 kV—right) voltage levels.

4.1.1.2.3 Minimum Distance Constraints Analysis for UAS Inspection

The minimum safe distance during a powerline inspection depends on the UAS' ability to withstand electromagnetic interference. This ability depends greatly on UAS design and its magnetic and electric field strengths. The maximum electric field strength that can resist electromagnetic interference under normal operation is about 50 kV m^{-1} (Qiu et al. 2018; National Coordinating Center for Communications 2019; Zhang et al. 2019; Autodesk 2021), and the maximum magnetic field strength is 180 uT (Zhang et al. 2019) for a small UAS.

Figure 11 depicts the safe distance as a function of the UAS electric (a) and magnetic field (b) strengths for the three powerline types during horizontal and vertical inspections. Knowing the electric or magnetic field strengths of a UAS, one can derive the minimum safe distance for that UAS from Figure 11. A UAS's overall susceptibility depends on the susceptibility of the individual UAS components to outside interference, such as the magnetometer, GPS, compass, and autopilot. This susceptibility can be further affected by mitigations, such as shielding or individual components within a UAS. A UAS's overall susceptibility will most likely be based on the most vulnerable components.

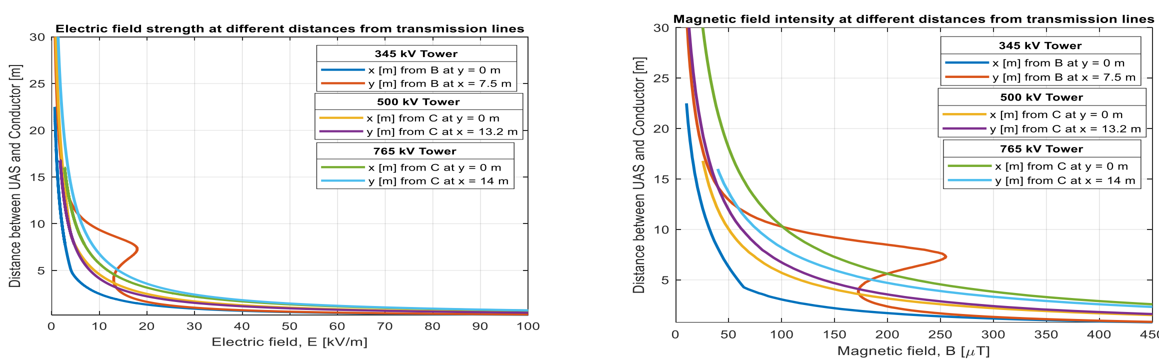

a) b)

Figure 11. Safe distance from conductor vs. electric field (a) and magnetic field (b) strengths for the three powerline types.

Tables 2 and 3 provide safe distances computed for various electric (Table 2) and magnetic (Table 3) field strength values. For instance, if the electric field strength of the UAS is 50 kV m^{-1} (Baker et al. 2019; Qiu et al. 2021), then the minimum safe horizontal and vertical distances (x_s, y_s) are (0.54 m, 0.6 m), (0.94 m, 1.03 m), and (1.37 m, 1.5 m) for the 345 kV, 500 kV, and 765 kV powerlines, respectively. However, if the magnetic field is the one that defines the minimum safe distance as was stated by Zhang et al. (2019), then a 180 μT threshold leads to (1.90 m, 8.76 m), (3.9 m, 3.92 m), and (5.1 m, 6.2 m) as the minimum safe distances from 354 kV, 500 kV, and 765kV powerlines, respectively.

Table 2. Minimum safe distances for various electric field strength intensities.

Electric Field Strength (kV m^{-1})	(x_s, y_s) (m)		
	345 kV	500 kV	765 kV
10	≥ (2.5, 9.35)	≥ (4.14, 4.58)	≥ (5.74, 6.77)
20	≥ (1.35, 1.64)	≥ (2.23, 2.49)	≥ (3.16, 3.58)
30	≥ (0.91, 1.01)	≥ (1.53, 1.69)	≥ (2.2, 2.42)
40	≥ (0.68, 0.75)	≥ (1.17, 1.28)	≥ (1.69, 1.82)
50	≥ (0.54, 0.6)	≥ (0.94, 1.03)	≥ (1.37, 1.5)
60	≥ (0.45, 0.49)	≥ (0.79, 0.86)	≥ (1.16, 1.22)
70	≥ (0.38, 0.42)	≥ (0.68, 0.74)	≥ (1, 1.04)
80	≥ (0.33, 0.36)	≥ (0.60, 0.64)	≥ (0.88, 0.92)
90	≥ (0.29, 0.32)	≥ (0.53, 0.57)	≥ (0.76, 0.81)
100	≥ (0.26, 0.29)	≥ (0.48, 0.56)	≥ (0.71, 0.74)

Table 3. Minimum safe distances for various magnetic field strength intensities.

Magnetic Field Intensity (μT)	(x_s, y_s) (m)		
	345 kV	500 kV	765 kV
100	`≥ (3.06, 10.28)	≥ (6.1, 6.73)	≥ (8.2, 10.35)
120	≥ (2.65, 9.77)	≥ (5.3, 5.73)	≥ (7.12, 8.85)
140	≥ (2.34, 9.37)	≥ (4.71, 4.97)	≥ (6.31, 7.74)
160	≥ (2.07, 9.05)	≥ (4.24, 4.39)	≥ (5.65, 6.88)
180	≥ (1.90, 8.76)	≥ (3.9, 3.92)	≥ (5.1, 6.2)
200	≥ (1.71, 8.48)	≥ (3.56, 3.56)	≥ (4.7, 5.6)
220	≥ (1.56, 8.19)	≥ (3.3, 3.24)	≥ (4.34, 5.13)
240	≥ (1.44, 7.87)	≥ (3, 2.99)	≥ (4.03, 4.73)
260	≥ (1.34, 1.59)	≥ (2.9, 2.77)	≥ (3.77, 4.39)
280	≥ (1.25, 1.45)	≥ (2.74, 2.57)	≥ (3.53, 4.09)

4.1.1.2.4 Validations of the Results

The results of the Quickfield simulations were validated using EMFACDC, an interactive software tool based on analytical methods (Fikry et al. 2022) that generates accurate electric field and magnetic (lateral) profiles at any user-defined height above ground level. The simulations revealed that the results of the two methods, EMFACDC and Quickfield, yield the same results for the electric and magnetic fields for all powerline types. Figure 12 provides an example of comparison of results. This figure compares the lateral profile of the electric field for the two methods at 1 m above the conductors for the three types of powerlines. As is apparent, the two methods produced the same results. In addition, the results obtained from this work were consistent with those of other published results, including the measurements and calculations for distances above ground (Ayad et al. 2019; Tourab and Babouri 2016; Houicher and Djekidel 2021).

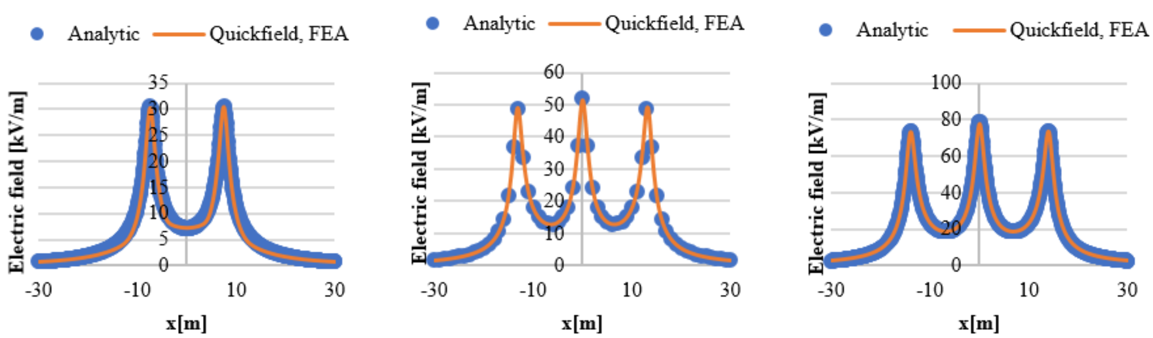

Figure 12. Analytical vs. FEA-obtained lateral profiles of the electric field for the 345 kV, 500 kV, and 765 kV powerlines.

4.1.1.3 Conclusion and Recommendations

This work computed and analyzed the distribution of electric fields generated by EHV transmission lines using the QuickField software. For this purpose, the electric and magnetic field profiles around 345, 500, and 765 kV transmission lines were analyzed from the perspective of UAS exposure. The results were compared with those from another package based on analytical methods. The two types of simulations exhibited excellent agreement.

Overall, the best guidance for operations around transmission lines is provided by Tables 2 and 3 for horizontal and vertical distances given the field profiles of the three power transmission lines. Two approaches can be applied to integrate these distances into safe operating practices. One assumes a level of local awareness and expertise that a UAS flight crew might be expected to have if working directly with a power authority around the transmission lines in question. These distances would be integrated into pre-flight planning for an operation given the normal information required to conduct a safe flight, including ambient weather and forecasts.

On the other hand, it may be best to abstract these results into conservative assumptions and minimum safe distances suitable for an operator, such as a contractor less familiar with the EM fields and field effects in question. Overall, minimum safe distances should likely be calculated as a single, conservative value based on multiple factors, including operator capability, UAS susceptibility to interference, UAS performance, and transmission line characteristics.

4.1.2 Inspection of Parallel Transmission Lines

4.1.2.1 Introduction

Powerlines are often aligned in parallel for long power transmission, affecting the strength of the resultant electromagnetic field. Indeed, multiple transmission lines within a corridor can strengthen or weaken magnetic fields (Henke at al. 2009), which can affect UAS operations. In this section, the magnetic fields in the vicinity of parallel EHV transmission lines are described from the perspective of UAS exposure using the electrostatic and magnetostatic modules of the Quickfield software, based on the 2D finite element method, primarily in the form of peak magnetic field profiles. Figure 13 provides an example for 345kV parallel powerlines. In this work, it is assumed that the UAS is inspecting the left powerline.

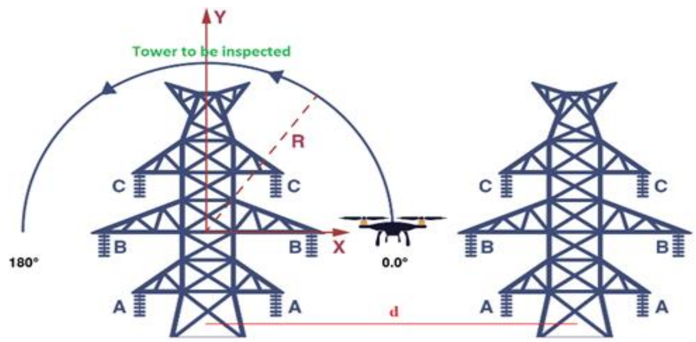

Figure 13. Direction of UAS motion during horizontal, vertical, and circular inspection scenarios for parallel transmission lines.

4.1.2.2 Results

For this investigation, only the magnetic field is reported as it requires higher safe distances than the electric fields as previously discussed in Section 4.1.1.2.3 (relevant simulation results are shown in Figures 5–6). Figure 14 depicts magnetic field as a function of horizontal distance, x (y = 0), for the three powerline types and two cases—single and double lines. As is apparent, the presence of the second line actually reduces the field under the first line. The profiles are almost identical close to the line; however, the difference between the fields is markedly different between the two towers.

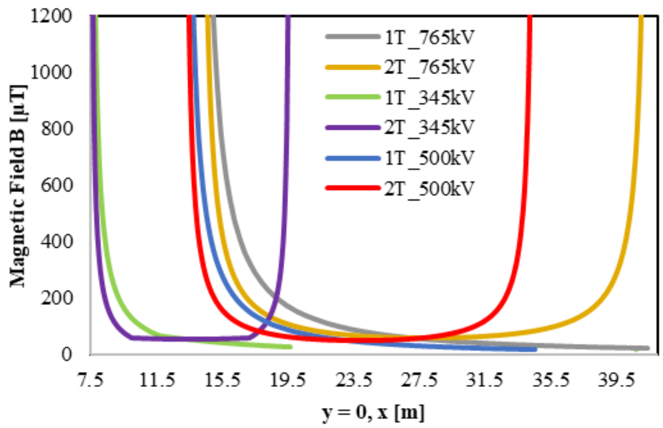

Figure 14. Comparison between the magnetic field generated by a single powerline and that generated in the presence of a second powerline during a horizontal inspection for the three types of powerlines. The gray, green, and blue curves indicate the magnetic field intensity from a single line, whereas the orange, purple, and red curves indicate the magnetic field intensity when a second identical line is placed at 29 m, 47 m, and 56 m away from the first line for the 345, 500, and 765 kV powerlines, respectively.

Figure 15 presents the magnetic field as a function of vertical distance, y (x = 0), for the three powerline types with and without the presence of a second powerline. As for the horizontal inspection, the presence of the second line clearly reduces the field under the first line. The profiles are almost identical further away from the line; however, the difference between the fields is markedly different between the two powerlines.

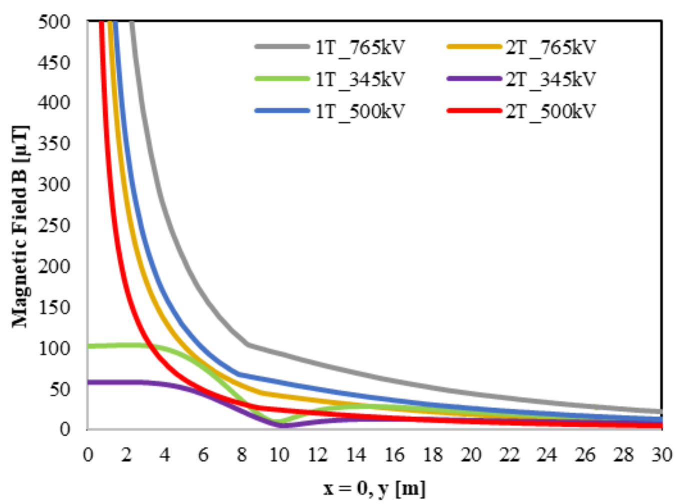

Figure 15. As in Figure 14, but as a function of vertical distance from powerlines.

Figures 16-19 illustrate the magnetic field intensity for four different radius values for each powerline type with and without a second powerline. The UAS movement began on the right side of the inspected transmission line and ended on the left. The right side of each figure corresponds to an angle, θ, of 0°, and the left side corresponds to 180°.

For the 345 kV powerline, at $\theta = 0°$ the presence of the second line increased the magnetic field compared to one line by more than 5, 65, 120, and 45 µT for R = 15, 18, 21, and 24 m, respectively. For $\theta \geq 90°$, the presence of the second line decreased the magnetic field compared to one line by more than 35, 9, 18, and 10 µT for R = 15, 18, 21, and 24 m, respectively.

For the 500 kV powerline, at $\theta = 0°$ the presence of the second line decreased the magnetic field compared to one line by more than 165, 295, 15, and 0.5 µT for R = 15, 18, 21, and 24 m, respectively. For $\theta \geq 90°$, the presence of the second line decreased the magnetic field compared to one line by more than 35, 25, 20, and 17 µT for R = 15, 18, 21, and 24 m, respectively.

For the 765 kV powerline, at $\theta = 0°$ the presence of the second line decreased the magnetic field compared to one line by more than 150, 120, 45, and 20 µT for R = 15, 18, 21, and 24 m, respectively. For $\theta \geq 90°$, the presence of the second line decreased the magnetic field compared to one line by more than 50, 32, 35, and 30 µT for R = 15, 18, 21, and 24 m, respectively.

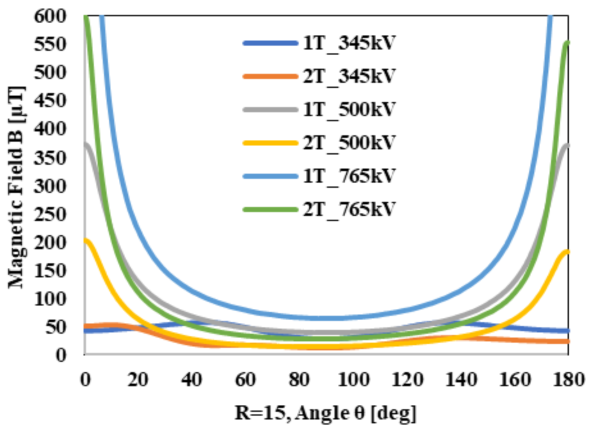

Figure 16. Comparison between the magnetic field generated by a single powerline and that generated in the presence of a second powerline during a circular inspection at a 15 m radius around each of the three types of powerlines.

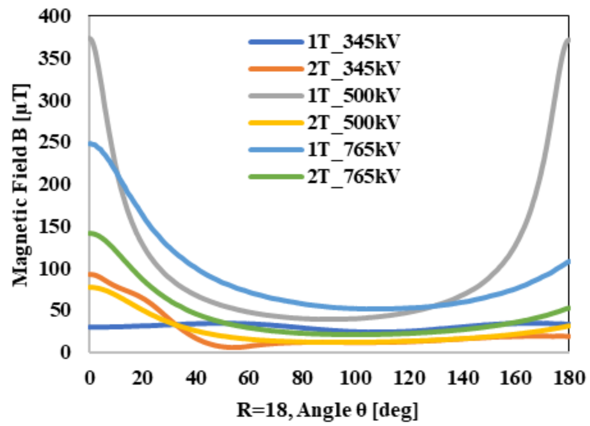

Figure 17. As in Figure 16 but for a radius of 18 m.

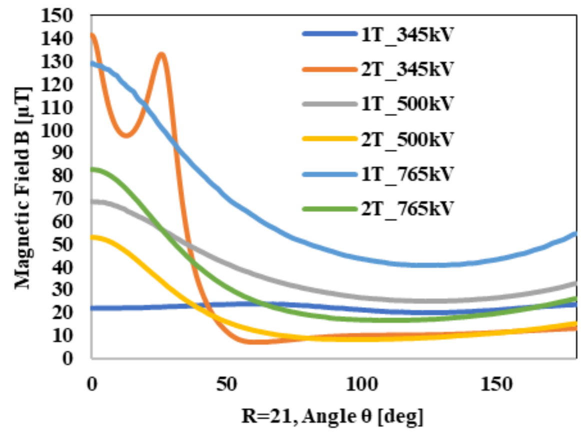

Figure 18. As in Figure 16 but for a radius of 21 m.

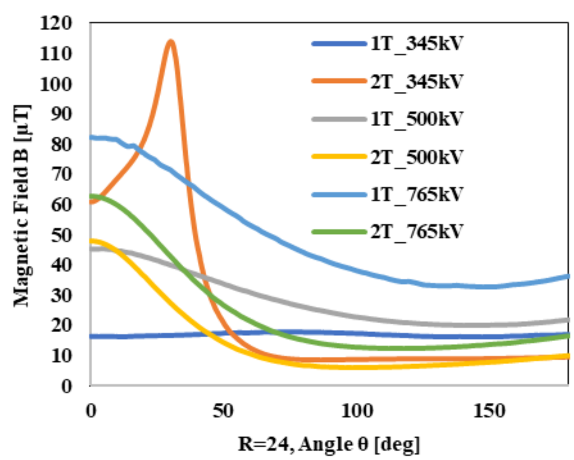

Figure 19. As in Figure 16 but for a radius of 24 m.

4.1.2.3 Conclusion and Recommendations

Numerical simulations were performed using the FEM with the QuickField software to compute and analyze the distribution of magnetic fields generated by parallel EHV transmission lines without considering the effect of the ground or shield wires. The magnetic field profiles of the 345, 500, and 765 kV transmission lines were analyzed from the perspective of UAS exposure. The details of where the two fields cancel out or reinforce each other were investigated; however, the results of the examined magnetic field profiles for parallel transmission depend upon knowing the relative phase of each of the conductors and loads in the line. The next step in this research will be to apply the proposed model to multi-parallel transmission lines and to compute electric fields, as well as apply it to other high-voltage transmission lines while considering the effects of shields, ground wires, catenaries, and when the ground surface under the transmission lines is irregular.

4.1.3 Inspection of Powerlines During Short Circuits

Electromagnetic fields increase exponentially during transmission line faults. A few studies have been conducted on these transmission line faults (Lisewski et al. 2014; DhanaLakshmi et al. 2011; Kumar et al. 2014; Ayad et al. 2019; Gu et al. 2008). For instance, Lisewski et al. (2014) studied the magnetic field surrounding a 110 kV power system with a short circuit fault and how that exposure could impact humans. Their results indicated that the magnetic flux density from the unbalanced load reached a peak of 576 µT. Ayad et al. (2019) simulated the electromagnetic field around a 400 kV transmission line and used the electrostatic and magnetostatic modules of the COMSOL software (COMSOL 2023). They simulated a line-to-line short circuit event and established that the peak magnetic field density was eighteen times greater than the nominal peak magnetic field density. All of these studies used different techniques to study faults in transmission lines; however, none have simulated a phase-to-phase fault in a transmission line and determined the minimum safe distance for a UAS from that information. Therefore, the objective of this simulation is to calculate the electric and magnetic fields during a phase-to-phase fault in a transmission line and estimate the minimum safe distance for UAS during horizontal and vertical inspections of these faults.

4.1.3.1 Methodology

The Quickfield software was used for the simulations, similar to previous investigations. A circuit was built to define the load on the transmission line, including a short circuit bridge to define the transient event. The magnetic field was calculated given the phase-to-phase short circuit using the physical parameters and the external load. The transient magnetic field analysis was then performed by calculating the magnetic field produced by a time-varying current. One million mesh nodes were used to achieve high confidence levels for the results.

Figure 20a depicts the circuit corresponding to 345 kV. The short circuit was placed between phases A and B. A similar circuit was used for the 500 kV scenario in Figure 20b. Figure 20c depicts the circuit corresponding to765 kV.

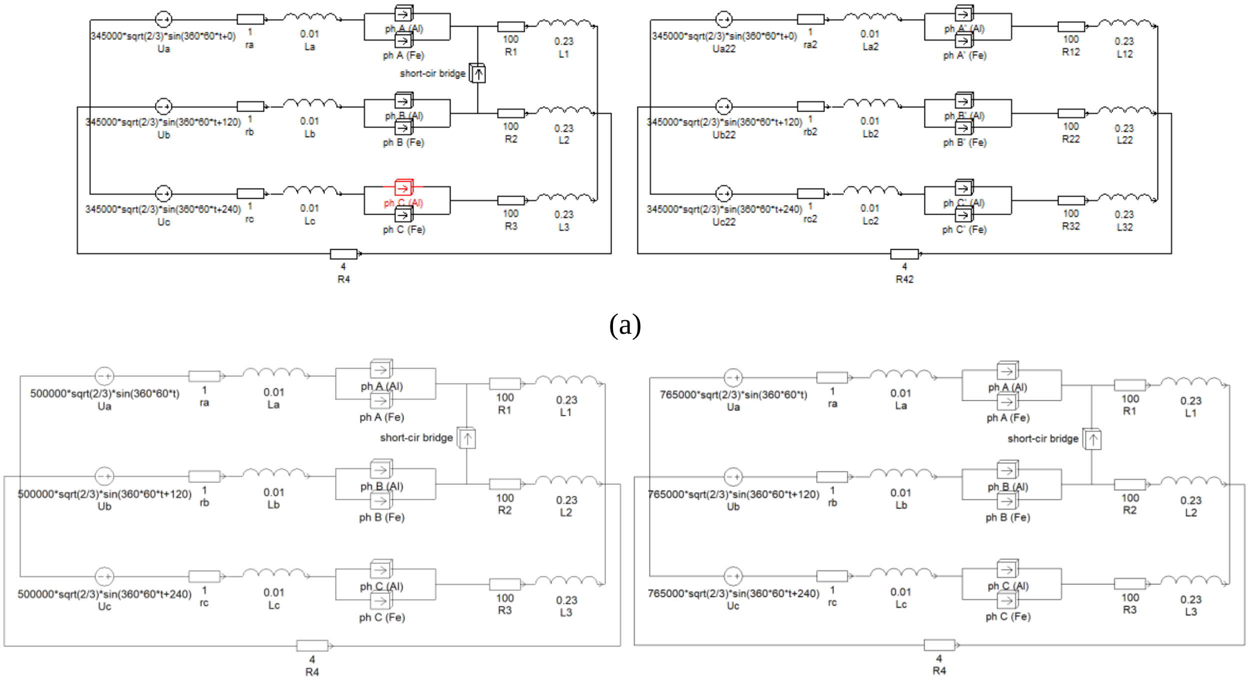

(a)

(b) (c)

Figure 20. Circuit diagram for modeling transient magnetic fields for a (a) 345 kV transmission line, (b) 500 kV transmission line, and (c) 765 kV transmission line.

4.1.3.2 Results

Faults can occur between any of the phases and the ground or even between phases. Faults are transient events that can last from 0.08 to 1.0 seconds, depending on the location and type of fault (Finneran at al. 2015). The simulations used short circuits that lasted 0.1 and 1.0 seconds. The 0.1-second simulation fault began at 0.96 seconds and ended at 1.06 seconds. The 1.0 second simulation fault began at 0.96 seconds and ended at 1.96 seconds.

Figure 21 depicts the short circuit bridge voltages and currents for the 500 kV powerline in the 0.1 second and 1.0 second scenarios. The voltage peaked above 0.5 MV, and the current peaked at 42 MA. The change in fault duration did not change the peak voltage and current values. The current or voltage spike occurred much faster than the full 1.0 or 0.1 seconds. The graphs indicate that the current transient lasted approximately 0.015 seconds, and the voltage transient lasted approximately 0.02 seconds.

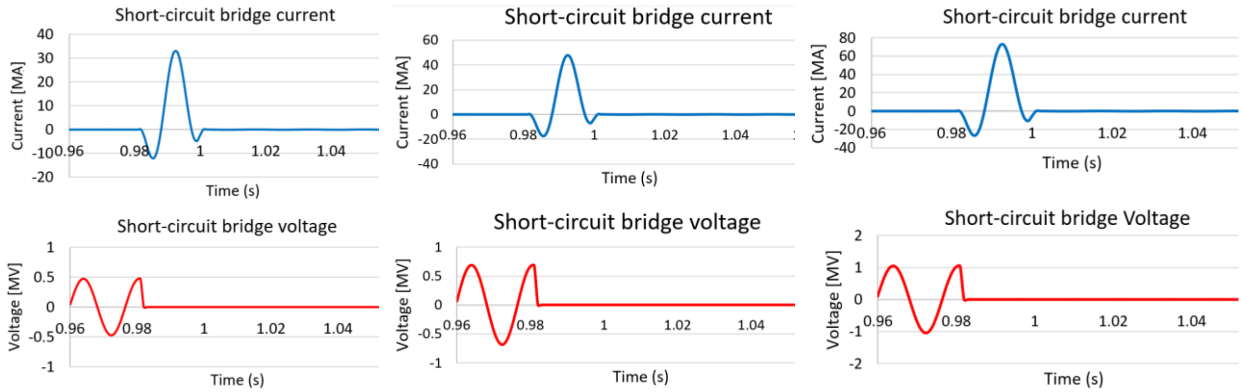

(a) (b) (c)

Figure 21. Short-circuit bridge currents and voltages for a (a) 345 kV transmission line, (b) 500 kV transmission line, and (c) 765 kV transmission line.

Figure 22 shows the current and voltage during the simulated phase-to-phase fault in the electrical transmission system. As the fault occurs at the specific time point, the Phase A current sharply increases, reaching its peak at 0.99 s. Similarly, the Phase B rises rapidly, peaking at 1.05 s.

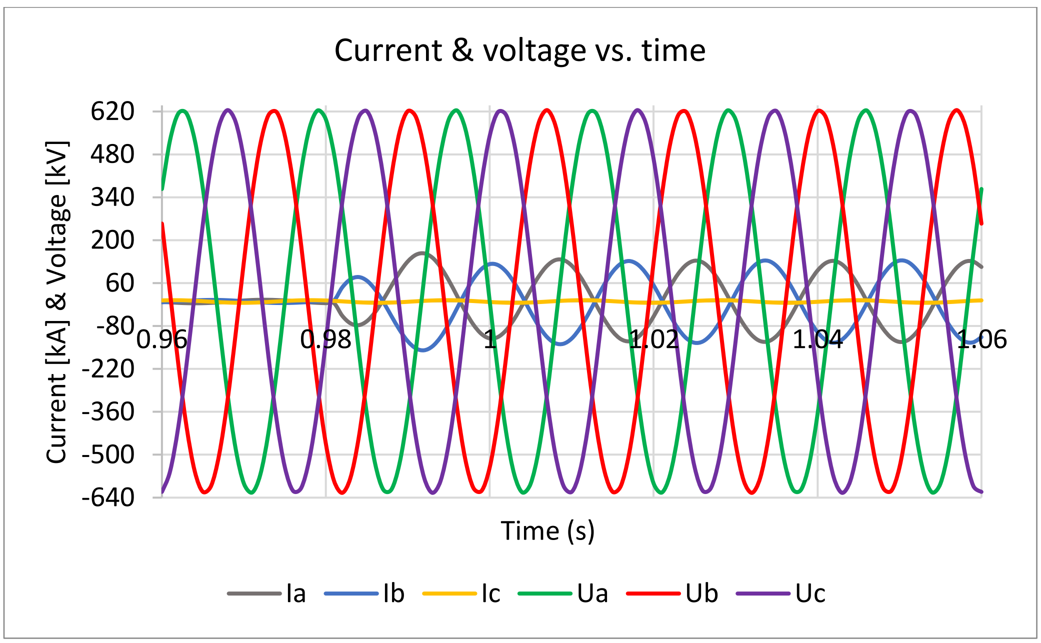

Figure 22. Three-phase voltages and currents during the phase-to-phase fault between phases A and B.

Figure 23 depicts the magnetic field at different horizontal locations for different heights across the three transmission lines. The center of phase B was located at $x = 0$ m. The plots illustrate the magnetic flux density for varying heights above and below the transmission lines. The peaks of the magnetic field appear 1 m above and below the transmission line at 23 mT for the 765 kV line, 15 mT for the 500 kV line, and 12 mT for the 345 kV line. These peaks decrease to 1.8 mT for the 765 kV line, 1 mT for the 500 kV line, and 0.7 mT for the 345 kV line at 10 m above and below the transmission lines at the center of phase B. These peak values are eighteen times greater than the magnetic field density of the transmission lines operating nominally.

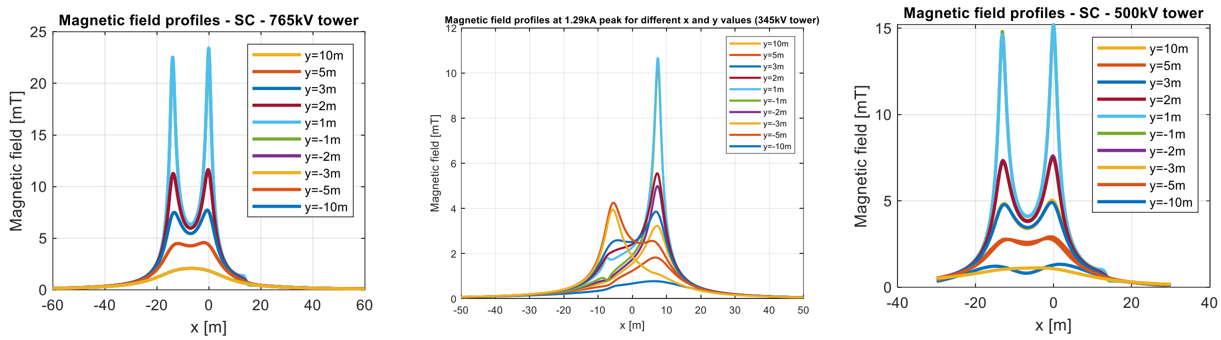

Figure 23. Peak values of the magnetic field at different horizontal and vertical locations during a phase-to-phase short circuit.

Figure 24 depicts the magnetic field intensity at different radii and angle values around the transmission line. These results indicate that the magnetic field decreases as the radius increases; however, the highest magnetic field is at R = 15 m for the 765 kV and R = 13 m for the 500 kV transmission line.

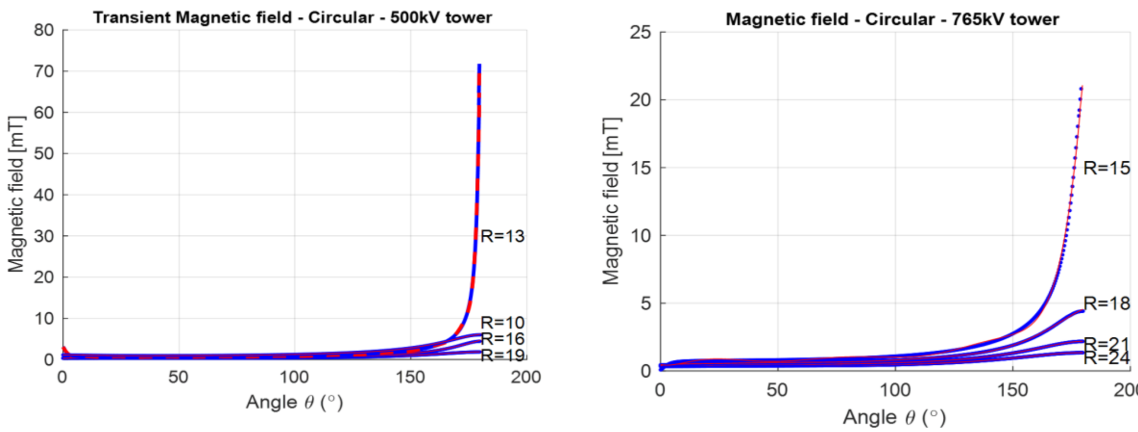

Figure 24. Magnetic field for different angle and radii values during a phase-to-phase fault scenario in the 500 kV and 765 kV transmission lines.

As expected, the results indicate a high magnetic field near the transmission line and that field decreases as the distance from the transmission line increases. The circulation of the short circuit current bridge yielded a high magnetic field of mT order. The maximum amplitude of the magnetic field with a phase A to phase B fault was approximately eighteen times greater than the nominal value.

The minimum safe distance during a phase-to-phase fault inspection depends on the UAS' ability to withstand electromagnetic interference. As previously stated, this ability depends greatly on the UAS design and its magnetic and electric field strengths. Figure 25 depicts the safe distances as a function of magnetic field strength for the three powerline types during horizontal and vertical inspections. Table 4 lists minimum horizontal and vertical safe distances for different UAS magnetic field strengths. Assuming a UAS magnetic field threshold of 180 µT (Zhang et al. 2019), the minimum safe distances (x_s, y_s) are (22.74 m, 33.11 m), (29.2 m, 27.11 m), and (39.4 m, 35.62 m) for the 345 kV, 500kV, and 765kV lines, respectively.

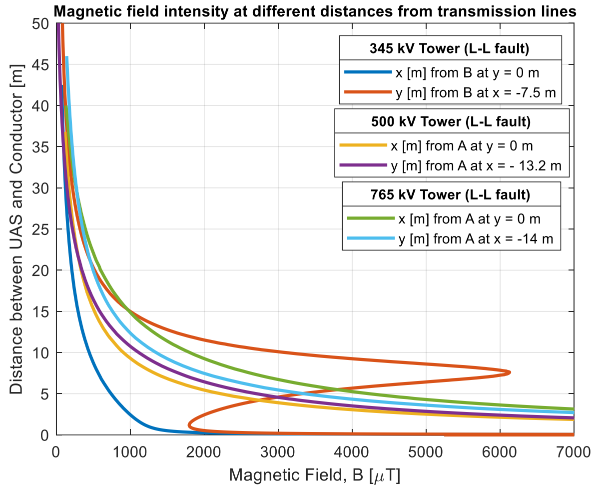

Figure 25. Minimum safe distance vs magnetic field strength.

Table 4. Safe distances for various magnetic field strength intensities in the case a phase-to-phase fault.

Magnetic Field Intensity [μT]	(x_s, y_s) [m]		
	345 kV L-L Fault	500 kV L-L Fault	765 kV L-L Fault
100	≥ (34.86, 45)	≥ (19.53, 36.01)	≥ (25.8, 45.2)
120	≥ (30.77, 40.63)	≥ (22.11, 32.36)	≥ (29.33, 42.15)
140	≥ (27.42, 37.57)	≥ (24.91, 30.42)	≥ (33.01, 39.29)
160	≥ (24.87, 35.03)	≥ (27.21, 28.76)	≥ (36.33, 37.29)
180	≥ (22.74, 33.11)	≥ (29.2, 27.11)	≥ (39.4, 35.62)
200	≥ (20.91, 36.01)	≥ (30.93, 31.47)	≥ (42.08, 34.09)
220	≥ (19.3, 30)	≥ (32.42, 24.95)	≥ (44.28, 32.8)
240	≥ (17.91, 28.76)	≥ (33.76, 23.97)	≥ (46.22, 31.54)
260	≥ (16.78, 27.68)	≥ (34.91, 23.06)	≥ (47.9, 30.45)
280	≥ (15.7, 26.71)	≥ (35.95, 22.26)	≥ (49.34, 29.43)

Table 4 serves as a precautionary framework, empowering UAS operators with the requisite knowledge to maintain safe distances in the face of unforeseen line faults. This is particularly pertinent in areas that have recently experienced severe weather, for example, which can increase the likelihood of faults. In addition, regions of transmission lines located further from the circuit breaker are especially vulnerable, as a phase-to-phase fault could inflict significant damage on nearby UAS. Operators should also have access to data from the electricity provider and be mindful of surrounding vegetation, which can come into contact with lines and induce phase-to-phase faults.

4.1.3.3 Conclusion and Recommendations

This study shows that a phase-to-phase short circuit can cause a significant increase in the strength of the magnetic field surrounding a transmission line. This increase can be as much as or more than eighteen times the normal magnetic field strength. As a result, the safe distance for a UAS from a transmission line during a short circuit is much greater than the safe distance under normal operating conditions.

This application to UAS operations is a sub-case of the guidance suggested above to keep the aircraft clear of EM field effects. The safe distance is much larger; therefore, special care should be taken in the case of short circuit during inspections or inspections that have a higher risk for this type of issue. Normal guidance suggestions indicate that safe distance values might be abstracted into a single conservative value for UAS operators not familiar with the exact specifics of the EM effects; however, the short-circuit situation should be treated and calculated more carefully to provide a balance between the needs of the inspection and the larger safe distances. Some of the recommended safe distance values could still be combined into fewer conservative assumptions; however, these adjustments should be made through further careful analysis.

4.1.4 Inspection of Transformers and Minimum Safe Distances

UAS are also used to inspect transformers. These transformers emit considerably higher electric and magnetic fields than other grid components, which can cause errors in the UAS' GPS, magnetometers, and transmitted data, among other considerations. GPS and magnetometer errors could cause the UAS to crash into transformers and possibly cause explosions since these transformers are mostly oil immersed. Most studies on transformers' EMF distributions have focused on the internal magnetic fields. These studies do not provide any data regarding the field densities in the surrounding areas of the transformers and do not correlate to the operational safety of a UAS. Here, the electromagnetic fields radiated outward by two commercially available three-phase and single-phase pole-mounted power transformers at different operating modes are analyzed using the 3D FEM.

4.1.4.1 Methodology

Two popular commercial transformers, a three-phase transformer and a single-phase three-transformer bank, were implemented using the 3D modeling software Autodesk Inventor (Autodesk 2021) and the FEM analysis plug-in (EMWorks 2022). The three-phase transformer, depicted in Figure 26a, was designed using parameters acquired from the commercially available transformer produced by Hitachi Energy (2022). The manufacturer's specifications, listed in Table 5, were used to design the 3D model of this 3-phase transformer bank, and the EMworks plug-in was used to evaluate the model structure and apply the 3D mesh for the FEM. The design consists of three components needed for the analysis: the core (a), primary windings (b), and secondary windings (c).

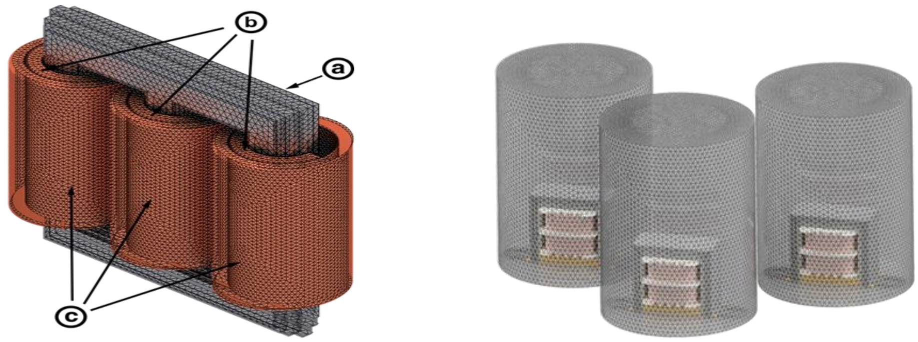

(a) (b)

Figure 26. 3D model of the 3-Phase (a) and 1-Phase (b) Transformer with mesh.

Table 5. Three-phase transformer specifications.

Manufacturer	Voltage [kV]	Current [kVA]	Frequency [Hz]	Load Loss [kW]	No-Load Loss [kW]	Short-Circuit Impedance [%]	Height [m]	Width [m]	Weight [kg]	Core Material	Coil Material	Winding Style	Cooling
ABB	13.4	2500	60	19.6	3.5	0.06	2.37	2.94	7630	Electrical steel	Copper	Shell type	Mineral oil

The second transformer model was based on three commercial 20 kVA cylindrical pole-mounted transformers produced by ABB Ltd (ABB 2022). The manufacturer's specifications for the 20 kVA transformer are listed in Table 6 and were used to design the 3D model of the 1-phase transformer bank. Each transformer is immersed in mineral oil for cooling. Here, the material shaped as the cylinder was considered to be the oil material, and the metal housing and its effects on the transformer's EMFs were ignored since they are negligible. The 3D design is depicted in Figure 26b.

Table 6. Single-phase transformer specifications.

Manufacturer	Primary Voltage [kV]	Current [kVA]	Frequency [Hz]	Weight [kg]	Core Material	Coil Material	Winding Style	Cooling
ABB	2.4	20	60	100	Electrical steel	Copper	Shell type	Mineral oil (22 Liters)

The EMworks plug-in was used to evaluate the model and apply the 3D mesh to perform the FEM, similar to the three-phase transformer design. The three transformers were surrounded by a 3D cube simulated as air in the environment.

4.1.4.2 Results

Field values were calculated assuming horizontal and vertical UA flights (Figure 27). The effects of the powerlines on the drone were assumed to be negligible.

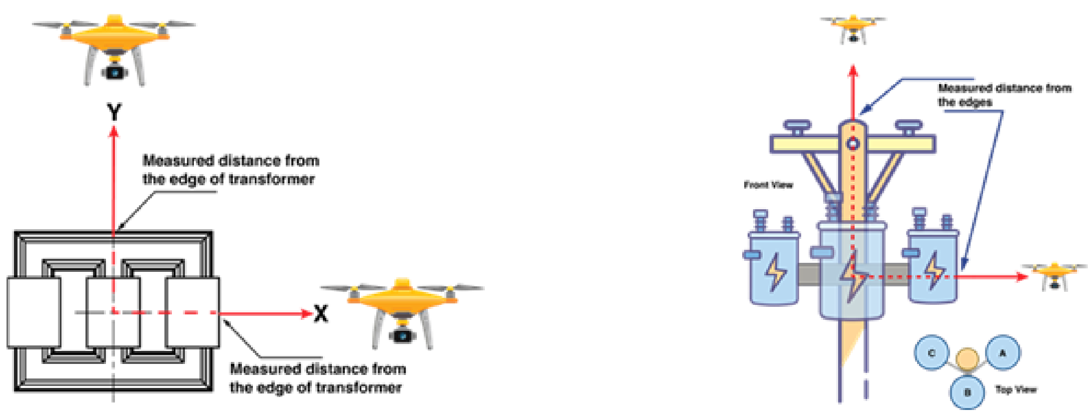

(a) **(b)**

Figure 27. Measurement locations of the three-phase (a) and single-phase (b) transformers.

4.1.4.2.1 Three-Phase Transformer

Figure 28 illustrates a cross-section across the XY plane of the three-phase transformer after the FEM analysis was complete. The legend's darkest blue section at and below 180 µT was assumed the UAS' safe flight zone with minimal interference. The red region, closer to the core and in the immediate vicinity of this core, has the highest amount of EMFs. The red to blue gradations also depict areas dense in EMFs.

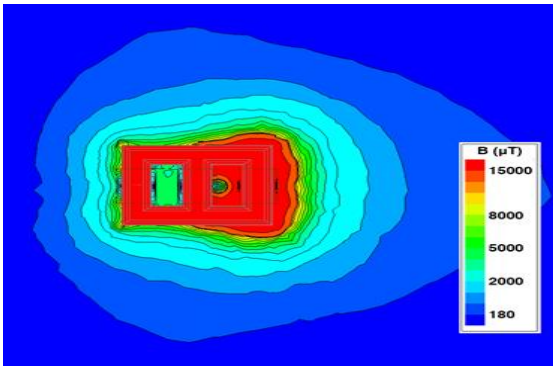

Figure 28. Magnetic field for the 3-Phase Transformer.

Figure 29a depicts the magnetic field as a function of the horizontal distance, *x*, from the edge of the three-phase transformer (Figure 27b). The magnetic field, as a function of vertical distance, *y*, is depicted in Figure 29b, and the values were taken from the top edge of the transformer, as depicted in Figure 26b. Assuming a maximum magnetic field strength of 180 μT as safe for a UAS, the minimum safe distances are 4.08 m horizontally and 3.69 m vertically.

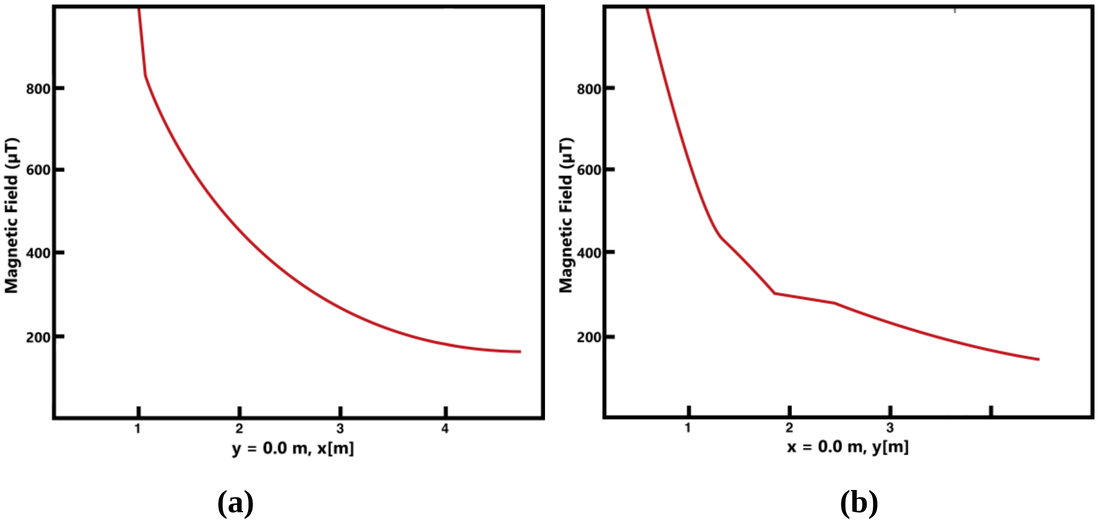

Figure 29. Magnetic field as a function of distance from the 3-Phase Transformer in the *x* (a) and *y* directions (b).

4.1.4.2.2 Single-Phase Transformer Analysis

Figure 30 illustrates an XZ cross-section for the simulation model. Similar to the three-transformer plot, the darkest blue section was considered safe since it was at or below 180 μT, where the UAS can operate with minimal EMF interference. The magnetic field seems to be intense from the plot's red area to the light green space.

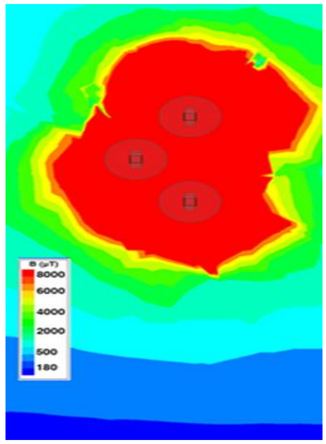

Figure 30. Magnetic field of the 1-Phase Transformer Bank.

Figure 31a shows the EM field as a function of horizontal distance from the transformer bank with a safe distance of 2.104 m on the *x*-axis. Similarly, Figure 31b depicts the magnetic field as a function of vertical distance where the safe distance is measured at 1.474 m on the *y*-axis. These values are estimated assuming the threshold safe UAS magnetic field strength of 180 µT.

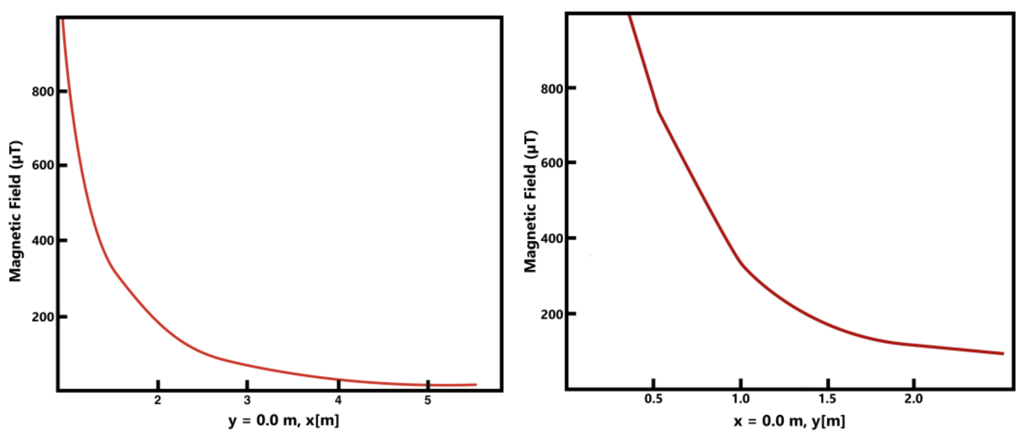

(a) (b)

Figure 31. Magnetic field as a function of distance from the 1-Phase transformer in the *x* direction (left) and *y* direction (right).

4.1.4.3 Conclusion and Recommendations

This study investigated the effects of magnetic fields generated by distribution transformers on a UAS. Two standard distribution transformer configurations were modeled in 3D software using commercially available data. These 3D models were simulated using a 3D FEM plug-in, and the results were analyzed using 3D color plots and *x* and *y* axis plots. The data were then analyzed to define the minimum safe distance boundaries for a UAS to operate around the two transformer configurations, which are provided in Table 7.

Table 7. Safe distances for single and three-phase transformers.

Transformer Configuration	Horizontal Distance (m)	Vertical Distance (m)
Single-Phase	2.104	1.474
Three-Phase	4.081	3.69

In these cases, the transformer effects provide clear guidance for maintaining a safe distance from transformers of this size and performance level. Safe distances may exceed these depending upon the circumstances; however, this should be carefully considered during pre-flight planning or when creating standard operating procedures. Transformers operating at higher performance levels should be evaluated to develop more comprehensive distance values. Likewise, groups of transformers may have to be evaluated for overlapping EM fields, such as at a power substation.

4.2 Wind Effect on UAS During Powerlines Inspections

4.2.1 Methodology

AirSim (Shah et al. 2018) was selected as a platform to investigate the effect of wind near powerlines. It is an open-source simulation platform that employs high-quality graphics rendering engines. This platform performs real-time simulations in a simulated world using either direct pilot control or scripted control of the aircraft via Python scripting. The platform also supports interfacing with small fixed-wing and multirotor aircraft through MavLink and ArduCopter. Simulations of shielded and confined operations can be performed in this platform by integrating real world-environmental conditions. AirSim can also be used to simulate terrain and object collisions, which makes it suitable for simulating shielded or low-altitude encounters where trees, structures, and the ground are potential issues.

A real-world environment, at Tiger Mountain in Washington (including 765 powerlines) was integrated into Airsim for this project (Figure 32). This location was chosen because of its dense powerline network, dense trees, non-uniform terrain, and high- and low-traffic roads. In addition, two UAS—a fixed wing and a quadcopter based on the DJI E310—were modeled using a JSBSim flight dynamics controller. Many programs were developed to perform the simulations, including the wind model and data collection and visualization algorithms.

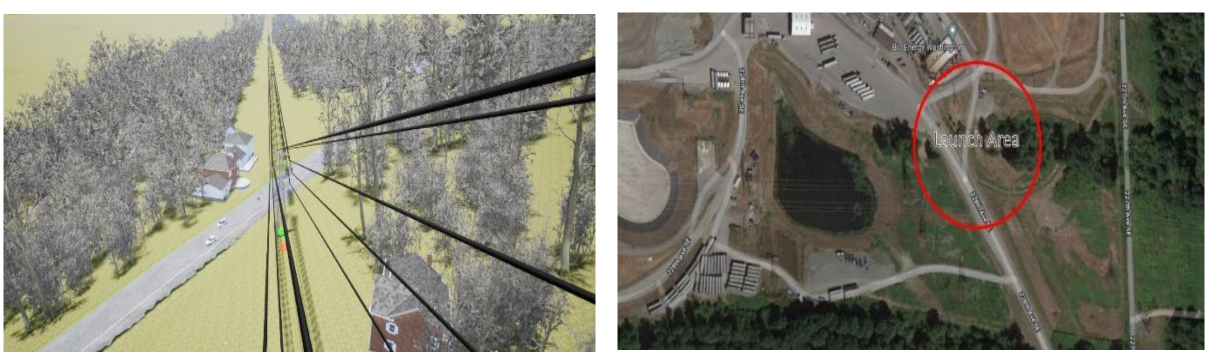

Figure 32. Tiger Mountain (Washington) simulation environment.

The AirSim API was modified to include additional control and data, such as from the Pulse-Width Modulation technique, for direct control and metric/data logging purposes. This modified API was then used by custom python scripts and code to automate the process of performing wind and wake vortex simulations, generation of the flight path, timing of the intruder, logging of data, generation of metric data, and visualization of the results.

The default implementation of the AirSim plugin implements a quadcopter based on the DJI E310 that provides a high-performance aircraft that is capable of performing high speed maneuvers. To further expand simulation capabilities, an AirSim plugin that adds support for fixed-wing aircraft using JSBSim, an open-source flight dynamics model, was also integrated into the code base to allow for simulation of fixed wing aircraft.

To simplify intruder aircraft implementation and make it more repeatable, pre-simulated intruder aircraft telemetry was used. These telemetry files were generated by flying the aircraft at the real-world location inside of aircraft simulators, specifically Microsoft Flight Simulator 2020 and X-Plane 11.

The simulation setup used to determine the impact of wind on a UAS near powerlines was for a UAS flying a survey mission starting at a constant altitude and distance from the wires. A constant wind was applied horizontally with a direction toward the powerlines, and the distance of the UAS from the powerlines was monitored, as shown in Figure 33.

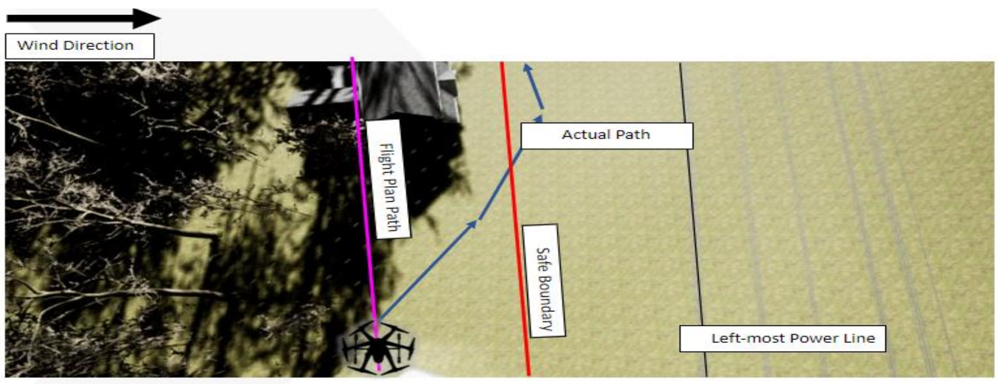

Figure 33. Set up for crosswind simulations.

4.2.2 Results

Several simulations at different wind velocity values were performed to determine the impact of wind on UAS near powerlines. The tested wind values can be divided into two categories: moderate winds for values lower than 22 m s^{-1} and high winds for values greater than 22 m s^{-1}. The Proportional-Integrative-Derivative controller of the multirotor was further tuned, which allowed the path deviation of the UAS to be smaller.

Several performance metrics were collected to estimate the impact of wind on UAS given a safe boundary for the powerlines. This safety distance was estimated at 5.1 m for 765 kV transmission towers. In addition, attitude angle change rates were analyzed to describe the controller response.

Figure 34 shows the results of horizontal path deviation of the UAS from the powerlines for a starting distance of 9.1 m. As is apparent, the UAS deviated from the planned path when the wind started blowing and stabilized after some distance, making it approach the unsafe boundary of the powerline. For wind speeds higher that 22 m s^{-1}, the UAS path was not as uniform as in the moderate wind scenarios. The UAS did not cross the unsafe boundary for this starting distance of 9.1 m, but it could not return to the original path.

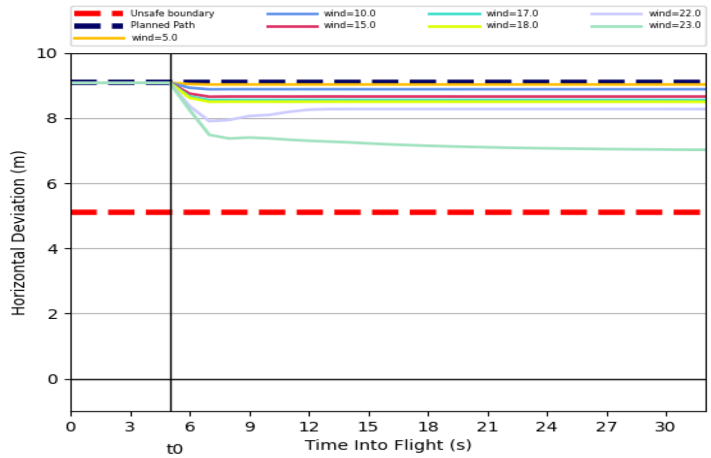

Figure 34. Horizontal path deviation of the UAS from the powerlines for a starting distance of 9.1 m.

Figure 35 depicts the UAS vertical path deviation from the powerlines with the starting distance of 9.1 m. The value of the deviation from the planned path was small, less than 0.1 m, for moderate winds lesser than 18 m s^{-1}. Higher wind speed values resulted in a significant vertical path deviation of more than 0.8 m that led the UAS to not maintain its path and to descend below the powerlines, as was observed for the wind of 23 m s^{-1}. This descent can present several risks to traffic, residences, and other infrastructure.

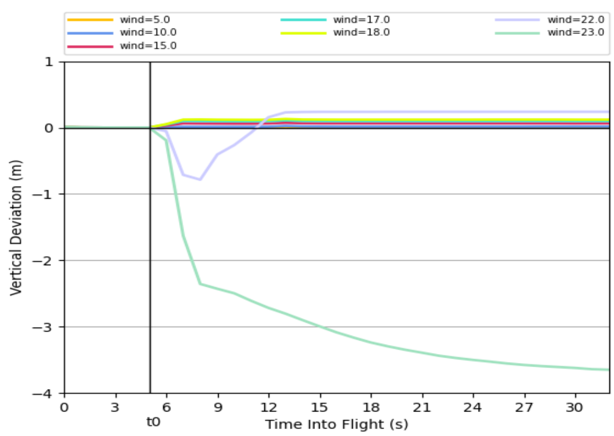

Figure 35. Vertical distance from the powerlines for a starting distance of 9.1 m.

Figure 36 shows the UAS controller attitude response (pitch, roll, and yaw) as a function of the wind speed. To maintain its path and withstand the wind, the UAS increased its attitude change rates in response to the wind. The higher the wind speed, the higher the angle changes.

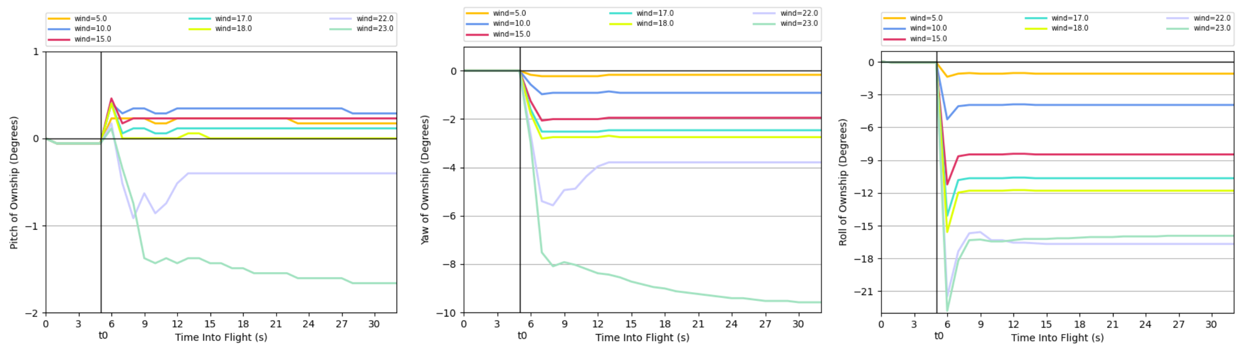

(a) (b) (c)

Figure 36. Attitude change rates (Pitch—Left, Yaw—Middle, and Roll—Left) with winds for simulated UAS flights near powerlines and for a starting distance of 9.1 m.

Table 8 summarizes the above results. It shows where the multirotor could not maintain a course after being displaced by a crosswind and demonstrates that winds higher than 22 m s^{-1} overwhelmed the aircraft's ability to stabilize. The mission parameters should be considered along with the UAS performance envelope to determine the maximum wind speed during flights near powerlines because any given inspection mission may require a maximum distance to resolve images with the necessary stability and resolution.

Table 8. Nearest horizontal distance and roll, pitch, and yaw impacts for the UAS flying next to powerlines when impacted with constant wind.

Wind (m s^{-1})	Maximum Horizontal Deviation of the UAS (m)	Maximum Vertical Deviation of the UAS (m)	Maximum Roll Deviation (°)	Maximum Pitch Deviation (°)	Maximum Yaw Deviation (°)
5	0.07	0.01	0 (Right) 1.55 (Left)	0.57 (Up) 0.63 (Down)	0. (Right) 0.29 (Left)
10	0.23	0.03	0 (Right) 5.27 (Left)	0.8 (Up) 0.46 (Down)	0 (Right) 1.03 (Left)
15	0.46	0.07	0 (Right) 11.23 (Left)	0.69 (Up) 0.34 (Down)	0 (Right) 2.12 (Left)
17	0.57	0.11	0 (Right) 14.09 (Left)	0.69 (Up) 0.57 (Down)	0 (Right) 2.64 (Left)
18	0.62	0.13	0 (Right) 15.58 (Left)	0.57 (Up) 0.74 (Down)	0 (Right) 2.92 (Left)
22	1.53	0.79	0 (Right) 21.49 (Left)	0.69 (Up) 2.12 (Down)	0 (Right) 7.23 (Left)
23	2.84	3.68	0 (Right) 22.8 (Left)	0.11 (Up) 3.04 (Down)	0 (Right) 12.96 (Left)

4.2.3 Conclusion and Recommendations

These results do not indicate unusual crosswind effects on the UAS. A multicopter's ability to maintain course or at least resist further displacement after the initial onset of wind effects is predictable and enables provision of guidelines on minimum distances from hazardous areas where EM effects may further disrupt safe navigation. The result in these cases is that there is a minimum distance that must be maintained from the unsafe zone surrounding high voltage powerlines for a given crosswind component. There is also a maximum wind component that will exceed the aircraft's performance envelope, resulting in a no-fly decision by the air crew as the ambient conditions exceed the UAS's ability to navigate the area.

The multicopter's aircraft type, like other copters, is subject to a reduction in performance envelope given strong headwinds; therefore, a strong quartering headwind or tailwind, or even a strong descending wind, will make it harder for the aircraft to maintain course and distance from the unsafe EM distances. This information should be used as part of the pre-flight decision process before launching an inspection mission.

The specific capacity to navigate a mission route will depend upon the aircraft's performance rather than a universal distance. Higher performance will result in the aircraft being able to maintain a closer distance to the unsafe EM area.

4.3 Wake Vortex Impact on UAS During Powerline Inspections

The wake vortex scenarios attempt to determine the impact of a wake vortex produced by crewed aircraft operating near small UAS performing powerline inspection. These scenarios differ from the static wind scenario in the sense that the wake vortex produces a varying, turbulent wind that changes in strength over time based on the distance of the UAS from the center of the wake vortex.

4.3.1 Methodology

Additional custom algorithms were developed in AirSim to implement the wake vortex calculations based on the relative position of the UAS from the wake vortexes center. These calculations use the equations and method described below while also considering the downward drift and decay of the generated wake vortex.

Multiple aircraft with varying sizes and characteristics were selected for this analysis. For the high-performance aircraft, the Boeing 747 and 737 were chosen. These aircraft are less likely to be encountered at low altitudes unless the UAS is performing operations near an airport or for firefighting operations. For the small, crewed aircraft, a selection of common general aviation aircraft, like the C172, were chosen with additional types of small aircraft that could be commonly encountered near powerlines, like the AT-502B used for crop dusting, and helicopters that can be used for powerline inspection purposes. The aircraft used and their physical parameters are provided in Table 9 where Vref/U is the reference landing speed calculated for the final approach and represents the minimum steady flight speed at which the aircraft is controllable in the landing configuration.

Table 9. Physical parameters of fixed wing aircraft and helicopter models used for the wake simulations.

Model	Approach Speed (Vref/U) (m s^{-1})	Wingspan/ Rotor Diameter(b) (m)	Landing Weight (W) (Kg m s^{-2})
Boeing 737-700, -700C (FAA 2022)	66.9	34.3	537284.0
Boeing 747-100, -100B (FAA 2022)	74.1	59.6	2512163.7
Cessna 172 Skyhawk Turbo JT-A (aka a Turbo Skyhawk) (FAA 2022)	31.9	11.0	11346.8
Thrush 510G (Thrush 2022)	55.0	14.5	46722.3
Air Tractor AT-502B (Air Tractor 2022)	39.6	15.8	35597.9
Bell Helicopter 206L4 (Bell Flight 2022)	56.6	11.3	20246.3
Bell Helicopter 412 (Bell Flight 2022)	72.0	14.0	52951.9
MD Helicopters 500E (MD Helicopters 2022)	69.5	8.1	15796.6

In these simulations, inspections were conducted with the multirotor at a speed of 12 m s^{-1}, following a path parallel to the powerlines at a distance of 15 m from the middle wires. This is illustrated in Figure 37.

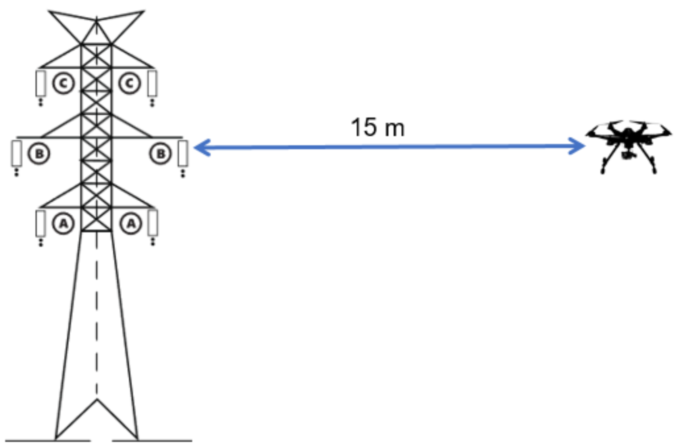

Figure 37. Planned location and path of the UAS near the powerlines.

These simulations did not incorporate the potential influence of electromagnetic fields generated by the powerlines. Thus, they solely focused on the effects of the wake vortex (Figure 38).

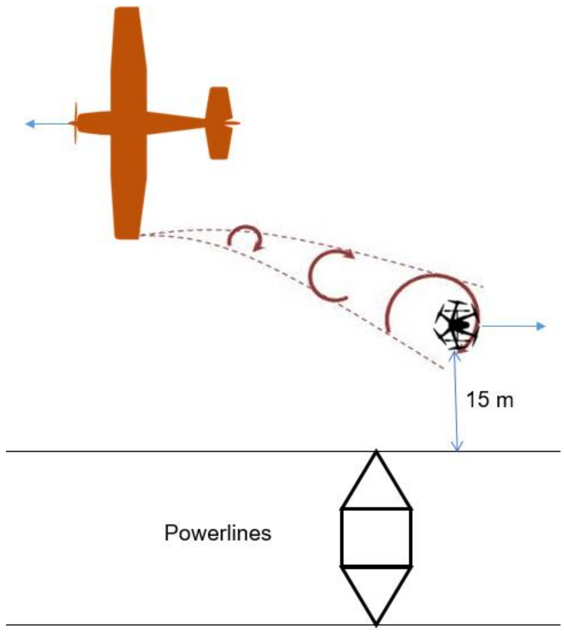

Figure 38. Effects of a wake vortex on a UAS near powerlines in the parallel scenario encounter (plan view).

Three scenarios were implemented and tested for the wake vortex. The first scenario involves the interaction of the UAS with a fixed-wing aircraft in a head-on scenario (Figure 39a), with the second scenario being the same encounter but with a helicopter intruder instead, as shown in Figure 39b. The third scenario involves the interaction of the UAS with a fixed-wing aircraft approaching from 90° to the right, as shown in Figure 39c. For each scenario, aircraft from Table 9 were simulated.

Figure 39. Head on encounter with fixed-wing crewed aircraft (a) and crewed helicopter (b), and 90° encounter with fixed-wing crewed aircraft (c).

4.3.1.1 Wake Vortex Model

Several models can be used to generate aircraft vortices, including Burnham-Hallock, Lamb-Oseen, and Navier-Stokes. These models were compared by Wang et al. (2019), who concluded that Burnham-Hallock and Lamb-Oseen are the best choices for UAS wake modeling. For these reasons, the Lamb-Oseen model was implemented for this project. This model requires significantly less simulation time when importing flow data and eliminates the need for the time-averaging and a transcribing sub-routine necessary for fluid dynamics simulation results. This efficiency is useful since the simulation via AirSim requires the results to be calculated at the moment of the encounter between the aircraft and the UAS. The model's wake velocity $V_\theta(r)$ is defined as (Wang et al. 2019)

$$V_\theta(r) = (\Gamma_0/2\pi)[1 - \exp(-1.26(r/r_c)^2)] \quad (8)$$

Where r denotes the distance of the point to the vortex center and is expressed by:

$$r = \sqrt{(y - y_0)^2 + (z - z_0)^2}. \quad (9)$$

The definition of each parameter in these equations is provided in Table 10.

The initial circulation Γ_0 of the wake vortex for each aircraft model used in this simulation was calculated using

$$\Gamma_0 = W/s\rho U b. \quad (10)$$

The parameters in this equation are defined in Table 10.

The Lamb-Oseen equation models a wake-induced downwash distribution at the outset and may not properly describe the evolution of the post-roll-up wake vortex field over distance or time. Viscous dissipation in the atmosphere causes the wake vortex to grow and weaken. As a result, decay Γ over time was implemented using the decay model described by Hallock et al. (2015)

$$\Gamma = \Gamma_0(1 - T_i/N), \quad (11)$$

where T_i represents the number of time units since the vortex effects started and is expressed by

$$T_i = t/TN. \quad (12)$$

TN is the non-dimensional time unit describing the nearly linear decay of the strength of the wake vortices over much of their lifetime. One unit of time represents the time required for vortices to descend a distance equal to the initial spacing between two vortices (Hallock et al. 2015), as given by

$$TN = \pi^3 b^2/8\Gamma_0. \quad (13)$$

The model decays are based on how many time units have passed since it was generated. The wake vortex ends after *N*, usually between 6- and 8-time units.

The Lamb-Oseen model can also be used to simulate the wake generated by helicopters by replacing the wingspan parameter with the rotor diameter in (10) and (13) (Zioutis et al. 2010; Perrotta 2015; Zioutis et al. 2006). The wake is generated because a significant amount of higher pressure leaks up and around the lift device, which is one of the primary differences between a helicopter and a fixed-wing aircraft. The fixed-wing aircraft gets its lift from the fixed-wing surface, whereas the helicopter gets its lift from the rotor, which is a rotating airfoil (Hurt 1965).

Table 10. Parameters of the wake model, Lamb-Oseen, and decay.

Parameter	Description
V_θ	vortex velocity
(y_0, z_0)	vortex center
Γ/Γ_0	vortex circulation /vortex initial circulation
r	distance from the vortex center
r_c	vortex core radius
b	wingspan
S	vortex span ratio = $\pi/4$
ρ	air density
W	landing weight of aircraft
U	final approach speed (Vref)
T_i	number of time units since current vortex's start
TN	non-dimensional time units
N	time units required for the vortices to go to zero (6 to 8)

4.3.2 Results

The impact of wake vortices on the operation of a UAS in close proximity to powerlines was evaluated using scenarios similar to those described in the previous section. These impacts were evaluated using the following metrics:

- Horizontal deviation.
- Vertical deviation.
- Altitude change rates of the UAS controller by measuring the yaw, roll, and pitch.

The different scenarios did not incorporate the potential influence of electromagnetic fields generated by the powerlines. They solely focused on the effects of wake vortices on the UAS's position, orientation, and velocity.

4.3.2.1 Head-on Scenario

Figures 40-42 illustrate simulation results for the head-on scenario and eight aircraft. The results are compared to scenario 0, in which the UAS was flown along the path without encountering an aircraft and with no wind or wake vortex affecting the UAS.

Figures 40 and 42a illustrate y path deviations for the eight aircraft. These results indicate that larger aircraft cause larger horizontal path deviations, while the others produce very small deviations of less than 1 m.

Figures 41 and 42b illustrate the vertical deviation of the quadcopter due to the eight aircraft wake vortices. Similarly, only the larger aircraft caused significant vertical deviations. For these, the UAS could not maintain its position and was pushed upwards by the generated wake vortex.

Smaller aircraft produced small wake vortices and small deviations; therefore, the UAS was able to compensate easily.

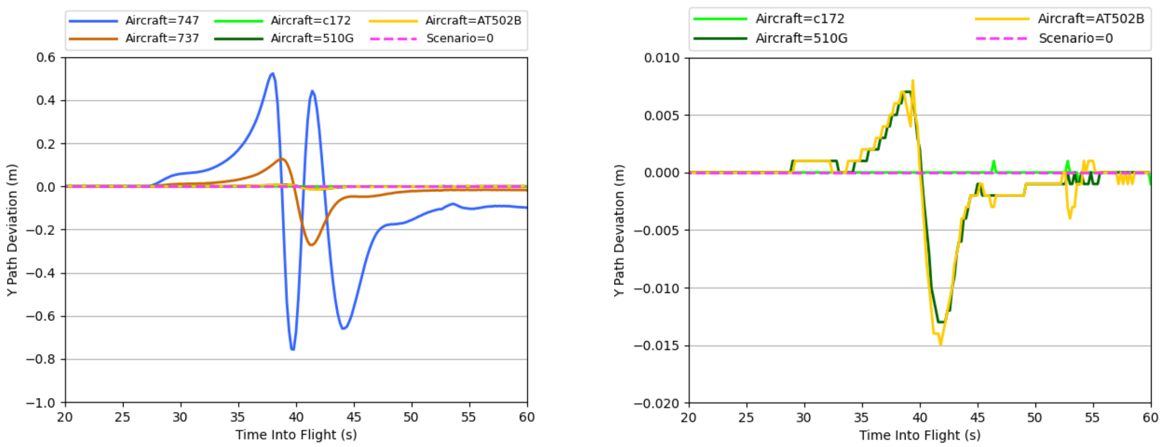

Figure 40. Horizontal, *y* component, path deviations of the UAS for head on encounters with fixed wing aircraft.

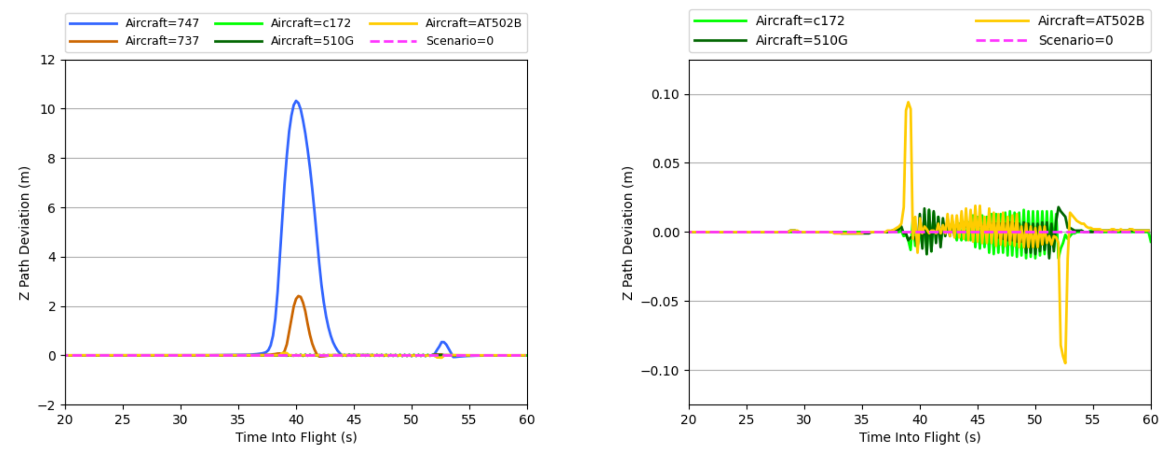

Figure 41. Vertical, *z* component, path deviations of the UAS for head on encounters with fixed wing aircraft.

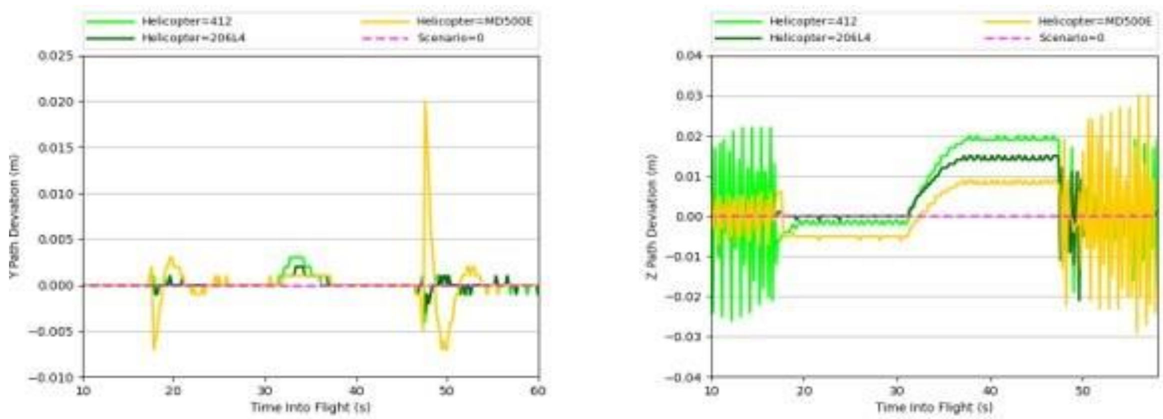

Figure 42. Horizontal (left) and vertical (right) path deviations of the UAS for head on encounters with helicopters.

Table 11 summarizes wake vortex effects on the UAS's path for both fixed-wing and helicopter aircraft. The initial distance must account for the maximum deviation of the UAS impacted by the wake vortex to keep the aircraft clear of the powerlines. The multi-rotor was pushed upwards by the generated wind current; therefore, its primary deviation was in the vertical direction. The larger aircraft required at least an additional 10.32 m buffer in the vertical direction, while the smaller aircraft and helicopters required at least a 0.09 m buffer. This buffer would need to be added to the unsafe boundary of the powerlines.

Table 11. Maximum path deviations of the UAS in the *Y* and *Z* directions for head on encounters with fixed-wing aircraft and helicopters.

Model	Maximum Deviation *Y* Toward the Powerlines (m)	Maximum Deviation *Z* (m)
B747	0.76	10.32
B737	0.27	2.40
C172	0.001	0.02
510G	0.01	0.02
AT502B	0.01	0.09
412	0.02	0.29
MD500B	0.004	0.03
206L4	0.003	0.26

The impact of the wake vortex on the UAS controller was evaluated by the altitude angle change rates, with results shown in Figures 43-46. Figure 43 illustrates the UAS's yaw, Figure 44 the roll, and Figure 45 the pitch changes induced by the fixed-wing aircraft. Figure 46 illustrates the yaw, roll, and pitch changes induced by helicopters.

None of the aircraft could produce a large effect on yaw, with the larger aircraft producing only a few degrees. The smaller aircraft essentially produced no effect on the yaw.

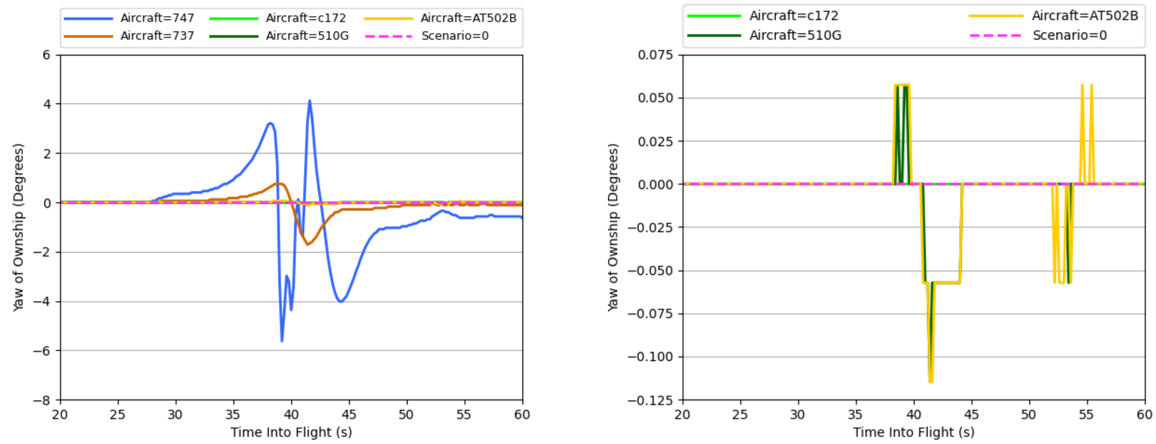

Figure 43. UAS yaw change rates for head on encounters with fixed-wing aircraft.

The larger aircraft did induce a large deviation in roll angle of more than 30°. The smaller aircraft essentially produced no effect on the multi-rotors' attitude, to the point that they could be considered controller noise. This effect is most likely from the multi-rotor trying to stabilize itself after it was pushed upwards by the generated wind current.

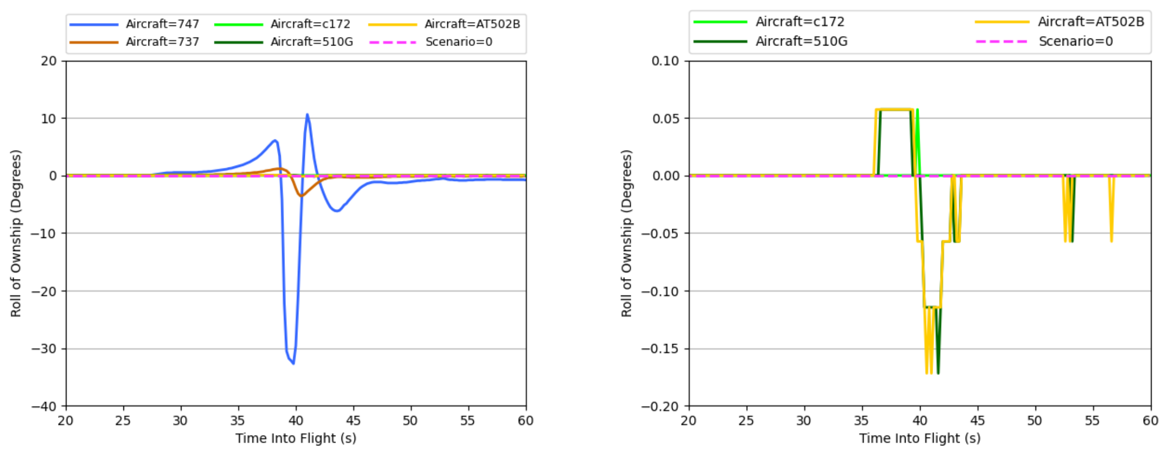

Figure 44. UAS roll change rates for head on encounters with fixed-wing aircraft.

The larger aircraft did induce a large deviation in pitch of ~40°. Similarly, the smaller aircraft essentially produced no effect on the multirotor attitude to the point that they could be considered controller noise.

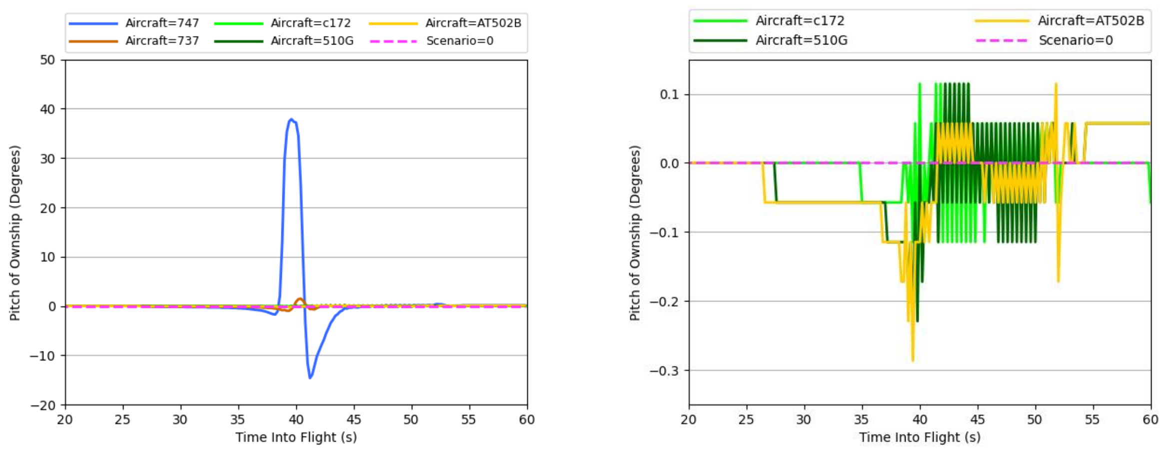

Figure 45. UAS pitch change rates for head on encounters with a fixed-wing aircraft.

The helicopter's wake vortex had little effect on the altitude angle change of the UAS, with a change rate on the order of a few degrees.

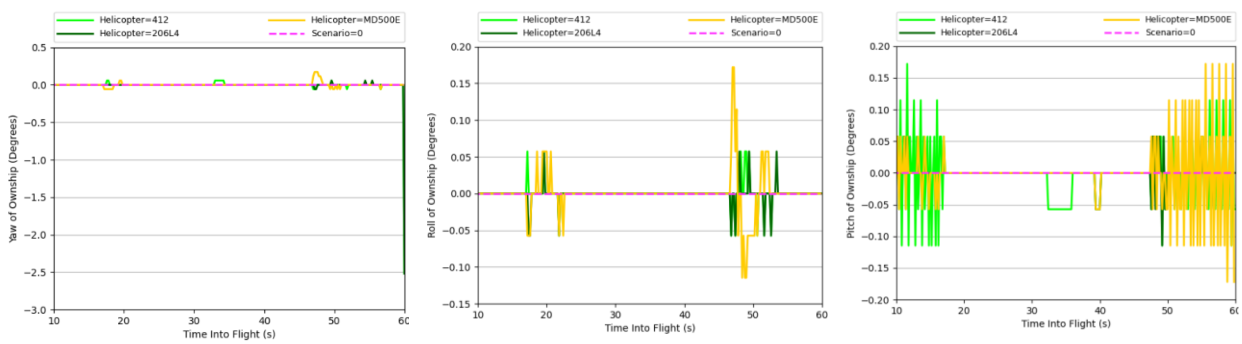

Figure 46. UAS yaw (left), roll (middle), and pitch (right) change rates for head on encounters with helicopters.

Table 12 summarizes the wake vortex effects of the tested aircraft on the attitude angles and the controller response of the UAS. The larger aircraft induced a large deviation in roll and pitch, and none of the aircraft produced large changes in yaw, with the 747 producing the largest (5.63 °), while the small aircraft induced minimal deviation in roll, pitch, and yaw, which could be considered controller noise. Larger or more unfavorable attitude displacements may occur at specific crossing locations of the wake vortex. The wake vortex produced by the helicopter was small enough that the multi-rotor could easily compensate.

Table 12. Maximum path attitude angle changes of the UAS for head on encounters with fixed-wing aircraft and helicopters.

Model	Maximum Roll Deviation (°)	Maximum Pitch Deviation (°)	Maximum Yaw Deviation (°)
B747	10.6 (Right), 32.72 (Left)	37.87 (Up), 14.61 (Down)	4.13 (Right), 5.63 (Left)
B737	1.15 (Right), 3.55 (Left)	1.49 (Up), 0.97 (Down)	0.75 (Right), 1.72 (Left)
C172	0.06 (Right), 0 (Left)	0.12 (Up), 0.17 (Down)	0 (Right), 0 (Left)
510G	0.06 (Right), 0.17 (Left)	0.12 (Up), 0.23 (Down)	0.06 (Right), 0.12 (Left)
AT502B	0.06 (Right), 0.17 (Left)	0.12 (Up), 0.28 (Down)	0.06 (Right), 0.12 (Left)
412	0.06 (Right), 0.06 (Left)	0.17 (Up), 0.17 (Down)	0.06 (Right), 2.52 (Left)
MD500B	0.17 (Right), 0.12 (Left)	0.17 (Up), 0.17 (Down)	0.17 (Right), 0.06 (Left)
206L4	0.06 (Right), 0.06 (Left)	0.06 (Up), 0.12 (Down)	0.06 (Right), 2.52 (Left)

To further investigate the impact of wake vortices on UAS, the velocity components [horizontal (X and Y axes) and vertical (Z axis)] were tested for head on encounters with a fixed-wing and a helicopter, as shown in Figures 47 and 48, respectively. As Figure 47 shows, larger crewed aircraft (B747 and B737) affected the velocity of the UAS as it tries to resist the wake effects. The magnitudes of the changes in speed were higher in the X and Z axes than for the Y axis. Figure 48 shows that the wake vortices generated by the helicopters did not significantly affect the speed of the UAS.

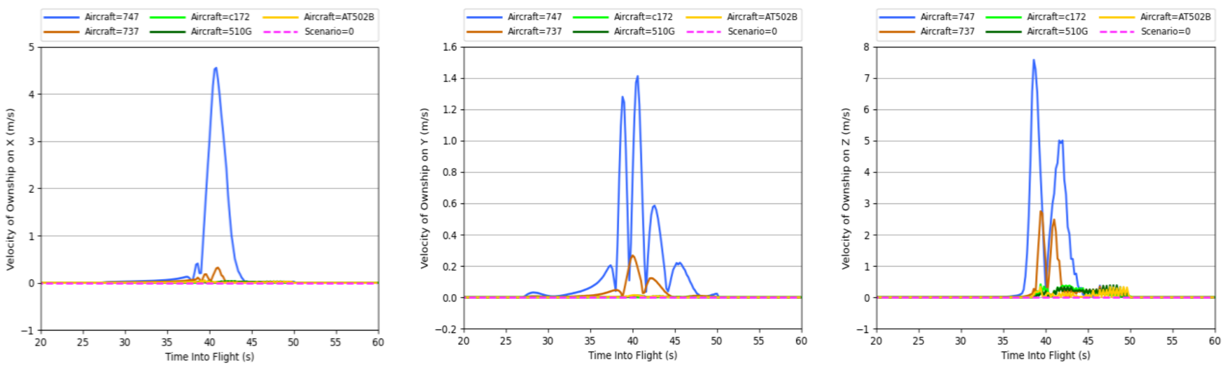

Figure 47. UAS velocity component changes on the X axis (left), Y axis (middle), and Z axis (right) for head-on encounters with fixed-wing intruders.

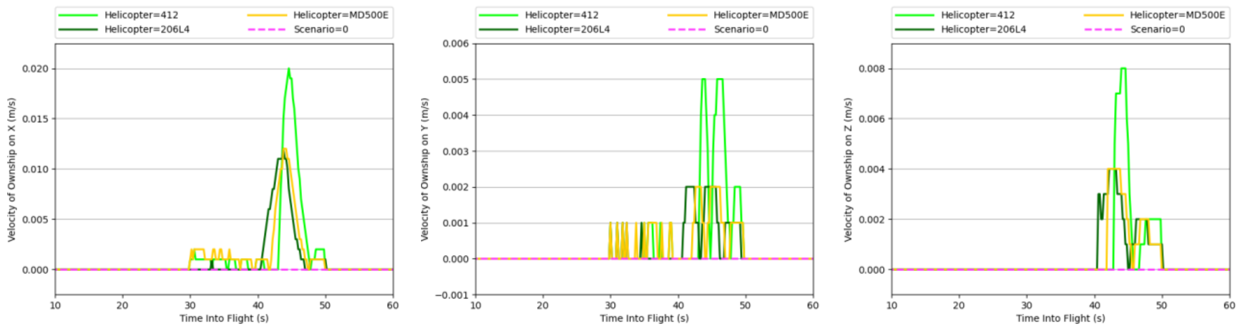

Figure 48. UAS velocity component changes on the X axis (left), Y axis (middle), and Z axis (right) for head-on encounters with helicopters.

Table 13 summarizes crewed aircraft wake vortex impacts on the three velocity components of the UAS. The speed change magnitudes were higher for the X and Z axes than for the Y axis. The larger crewed aircraft induced large velocity changes, with the 747 producing the largest increase in the Z axis of 7.57 m s^{-1}. The smaller fixed-wing aircraft and helicopters induced minimal changes in velocity.

Table 13. Maximum UAS velocity changes for head-on encounters with fixed-wing aircraft and helicopters.

Model	Maximum Velocity Change on X axis (m s^{-1})	Maximum Velocity Change on Y axis (m s^{-1})	Maximum Velocity Change on Z axis (m s^{-1})
B747	4.55	1.41	7.57
B737	0.32	0.27	2.74
C172	0.04	0	0.41
510G	0.03	0.01	0.38
AT502B	0.05	0.01	0.31
412	0.02	0.005	0.008
MD500B	0.01	0.002	0.004
206L4	0.01	0.005	0.004

The location of the UAS compared to the center of the wake vortices when hit by the aircraft's wake can impact the deviation from the planned path. For this purpose, the UAS position at the first impact with the wake was adjusted with a horizontal offset to capture the vortex's cross-section from its center in 1 m increments. Figure 49 depicts the impact of the UAS's position compared to the vortex center on the planned path's *Y* and *Z* positions for head-on encounters with an AT502B aircraft.

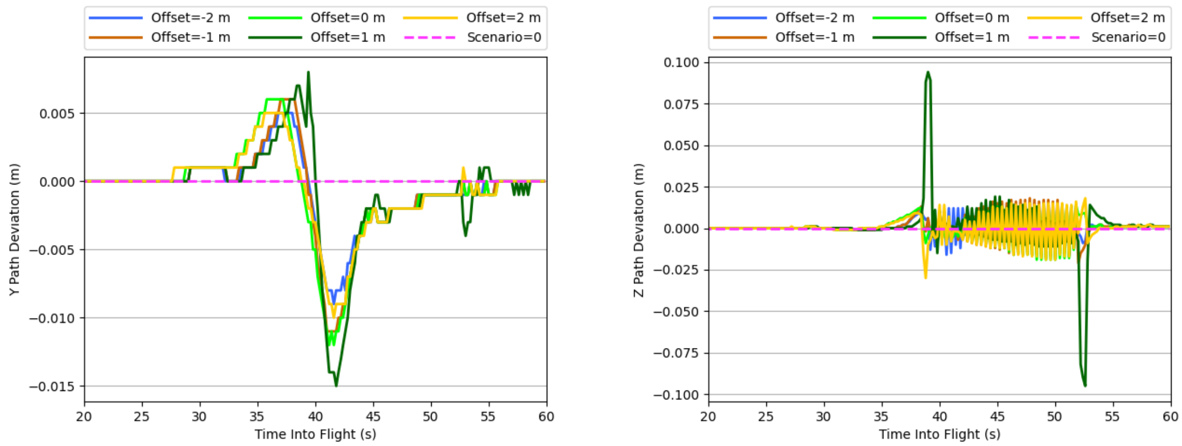

Figure 49. UAS horizontal (left) and vertical (right) path deviations for head-on encounters with an AT502B.

The aircraft chosen for these simulations was small. Therefore, the deviations are small. The larger deviations were recorded when the aircraft were closer to the vortex center, within 0 to 1 m (Table 14).

Table 14. Maximum UAS path deviations in the Y and Z directions for head-on encounters with an AT502B aircraft.

Location of UAS Compared to Vortex Center	Maximum Deviation Toward the Powerlines (m)	Maximum Deviation *Z* (m)
-2	0.01	0.02
-1	0.01	0.02
0	0.01	0.02
1	0.02	0.09
2	0.01	0.03

4.3.2.2 90° Encounter

In the 90° encounter scenario, the time and deviation extent impacts on the UAS were different relative to head-on encounters. The impact time was shorter, and the deviation from the planned path was smaller (Figures 50 and 51).

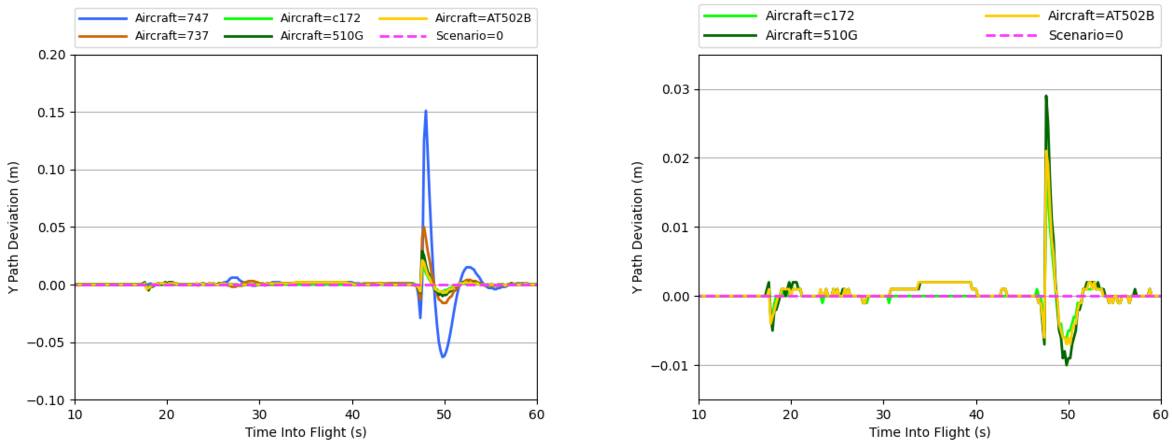

Figure 50. UAS horizontal path deviations for 90° encounters with fixed-wing aircraft.

Figure 50 depicts the Y component of the path deviation, while Figure 51 represents the vertical component. Similar to the head-on scenario, larger aircraft caused larger deviations from the path even after stabilization. The UAS could not maintain its position and was pushed upwards by the generated wind current.

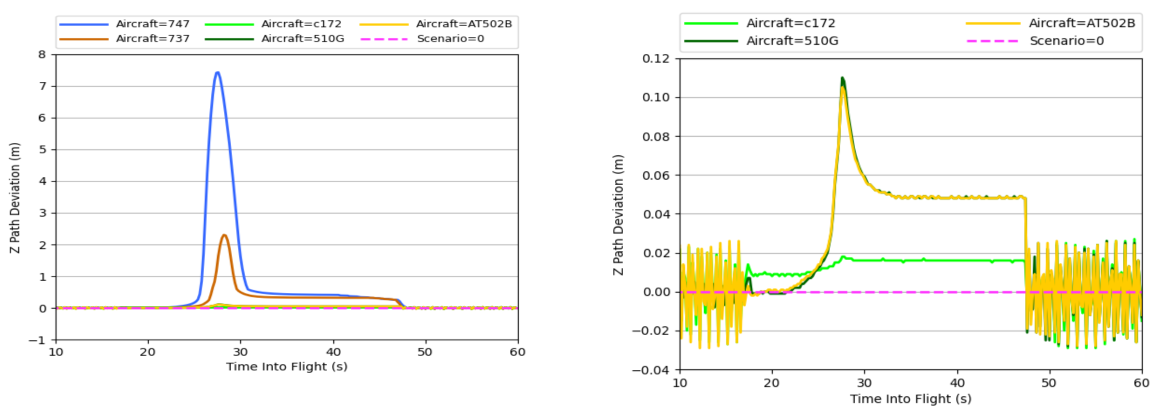

Figure 51. UAS vertical path deviations for 90° encounters with fixed-wing aircraft.

Like for the head-on scenario, larger aircraft cause larger deviations from the path and even after Similar to the head-on scenario, larger aircraft caused larger deviations from the path even after stabilization. The UAS could not maintain its position and was pushed upwards by the generated wind current. Table 15 summarizes the wake vortex effect of the tested aircraft on the UAS' path deviation. To get the UAS to remain clear of the powerlines, the initial distance must account for the maximum deviation of the UAS impacted by the wake vortex. Since this scenario involves a multi-rotor being thrown up into the air, its primary deviation is in the vertical direction. The larger aircraft required at least an additional 7.42 m buffer in the vertical direction. The smaller aircraft required at least a 0.11 m buffer in the vertical direction. This buffer would need to be added to the unsafe boundary of the powerline.

Table 15. UAS maximum path deviations in the Y and Z directions for 90° encounters with fixed-wing aircraft.

Model	Maximum Deviation Y Toward the Powerlines (m)	Maximum Deviation Z (m)
B747	0.15	7.42
B737	0.05	2.30
C172	0.02	0.03
510G	0.03	0.11
AT502B	0.02	0.10

Figures 52-54 illustrate the impact of wake vortices on the UAS controller for the yaw, roll, and pitch angles, respectively. Similar to head-on encounters, none of the aircraft could produce a large effect on yaw for 90° encounters.

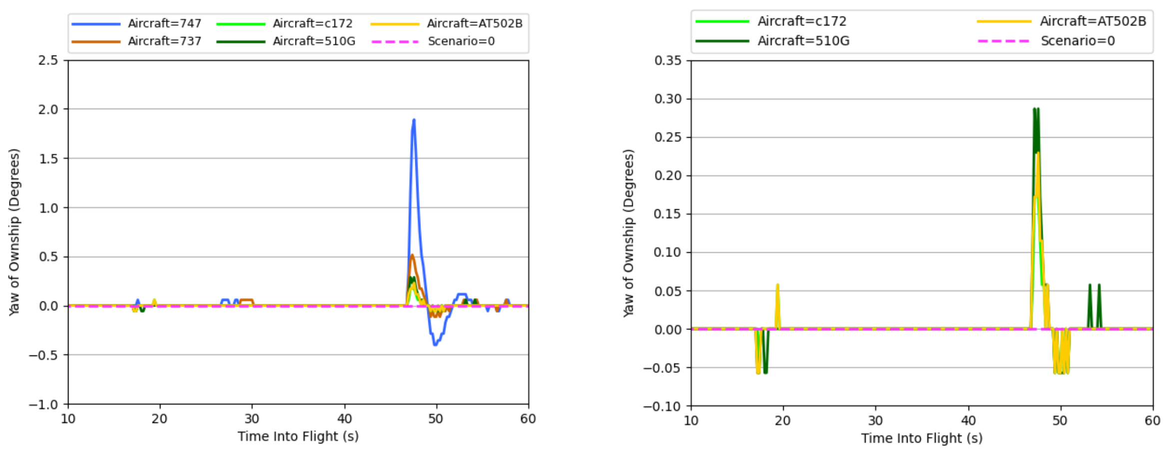

Figure 52. UAS yaw changes for 90° encounters with fixed-wing aircraft.

Unlike the head on scenario, the wake effect induced from the aircraft in the 90° scenario was small even for larger aircraft.

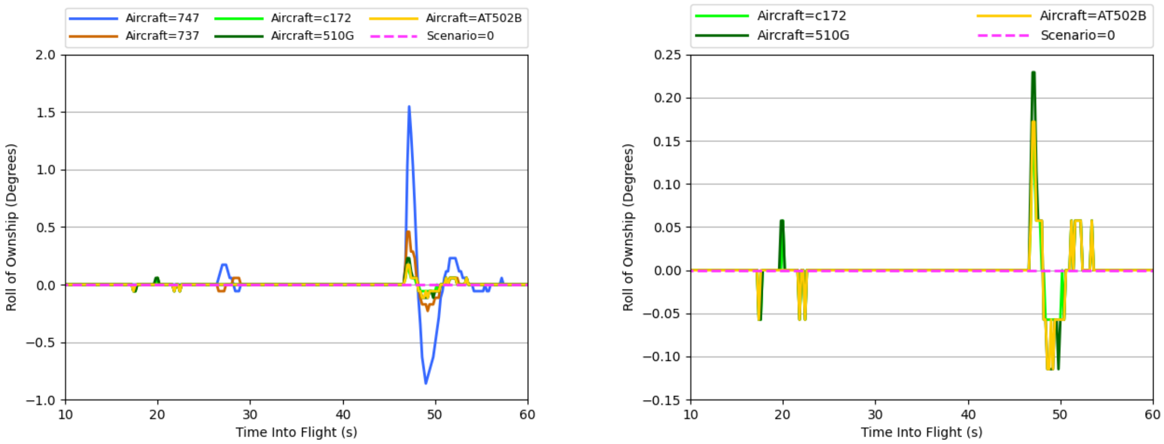

Figure 53. UAS roll changes for 90° encounters with fixed-wing aircraft.

The larger aircraft did induce a large deviation in pitch of ~40°, similar to the head-on scenario. Similarly, the smaller aircraft essentially produced no effect on the multirotor's attitude, to the point that they could be considered controller noise. This effect was most likely from the multi-rotor trying to stabilize itself after being pushed upwards by the generated wind current.

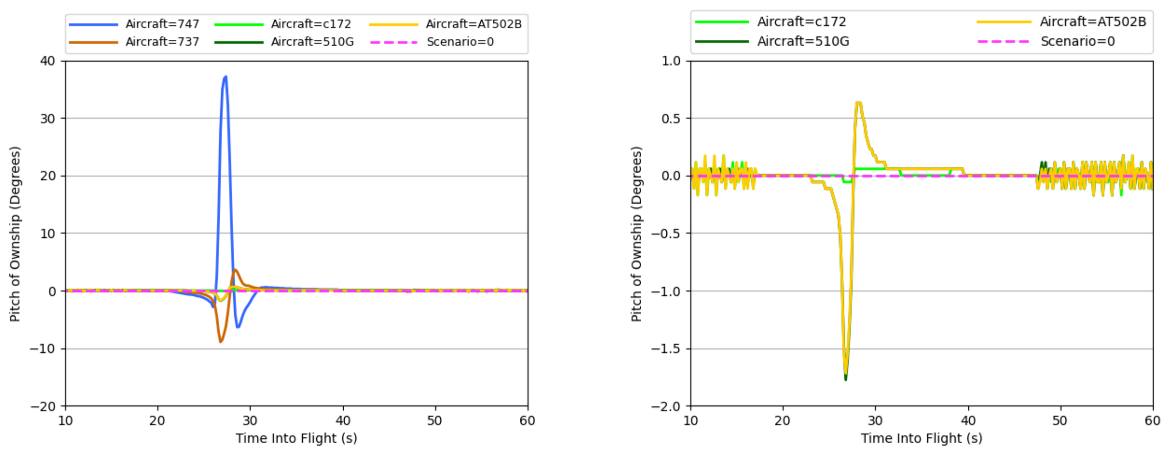

Figure 54. UAS pitch changes for 90° encounters with fixed-wing aircraft.

Table 16 summarizes the wake vortex effects of the tested aircraft on the attitude angles and the controller response of the UAS. The larger aircraft induced a large pitch deviation, and no aircraft produced large changes in yaw and roll. The small aircraft induced minimal roll, pitch, and yaw deviations, which could be considered controller noise.

Table 16. UAS maximum path attitude angle changes for 90° encounters with a fixed-wing aircraft.

Model	Maximum Roll Deviation (°)	Maximum Pitch Deviation (°)	Maximum Yaw Deviation (°)
B747	1.55 (Right), 0.86 (Left)	37.18 (Up), 6.36 (Down)	1.9 (Right), 0.4 (Left)
B737	0.46 (Right), 0.23 (Left)	3.61 (Up), 8.94 (Down)	0.52 (Right), 0.12 (Left)
C172	0.17 (Right), 0.06 (Left)	0.17 (Up), 0.17 (Down)	0.17 (Right), 0.06 (Left)
510G	0.23 (Right), 0.12 (Left)	0.63 (Up), 1.78 (Down)	0.29 (Right), 0.06 (Left)
AT502B	0.17 (Right), 0.12 (Left)	0.63 (Up), 1.72 (Down)	0.23 (Right), 0.06 (Left)

Figure 55 provides velocity component (X, Y, and Z axes) changes of the UAS for 90° encounters with fixed-wing aircraft. Wake turbulence effects were similar to the head-on encounters as the UAS's velocity changes along the X axis and Z axes were noticeable when the wake hit the UAS. Y axis changes were minimal and smaller aircraft essentially produced no effect.

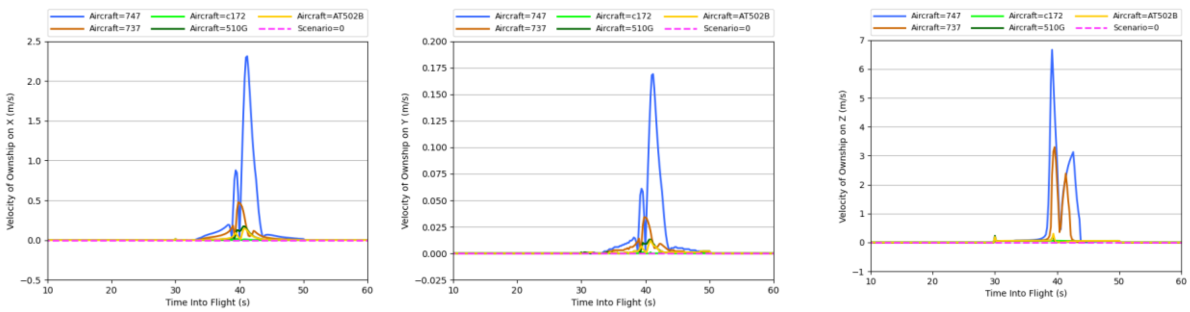

Figure 55. UAS velocity component changes on the X axis (left), Y axis (middle), and Z axis (right) for 90° encounters with a fixed-wing aircraft.

Table 17 summarizes wake vortex effects of the tested aircraft on UAS velocity components for 90° encounters. Velocity changes were notable only for the Boing 747 and 737. The other aircraft had minimal effects on the UAS.

Table 17. Maximum velocity changes of the UAS for 90° encounters with fixed-wing aircraft.

Model	Maximum Velocity Change on X axis ($m\ s^{-1}$)	Maximum Velocity Change on Y axis ($m\ s^{-1}$)	Maximum Velocity Change on Z axis ($m\ s^{-1}$)
B747	2.31	0.17	6.61
B737	0.48	0.05	3.24
C172	0.04	0.01	0.52
510G	0.15	0.02	0.52
AT502B	0.15	0.03	0.57

The UAS path should account for deviations caused by the aircraft wakes in the event of an encounter to avoid the EM effects of the powerlines. The results of the various simulations indicate that the wake vortices generated by small aircraft were weak enough to be considered controller noise, whereas the wake vortices generated by the larger aircraft were stronger and could cause significant deviations in position and attitude. A high-performance quadrotor UAS could easily compensate for the wake vortices created by smaller aircraft, which are more likely to be encountered near powerlines. Head-on encounters produce larger deviations than 90° encounters. In addition, the impact of the wake was more prominent when the UAS was flying near the vortex center than when it was flying through its side. The helicopters used in the simulation were small models used for inspection, firefighting, or agricultural operations and are likely to be near the ground or powerlines. The helicopters produced some controller noise in forward flight but did not affect the UAS. The hovering case was not considered; however, it is expected that a hovering helicopter will have a greater effect on the UAS due to downwash.

4.3.3 Conclusions and Recommendations

To better understand the effects of a broad cross-section of wake turbulence effects on UAS, wake models were applied in AirSim to UAS in close proximity to power transmission lines when interacting with crewed aircraft—specifically 747, 737, Cessna 172, Thrush 510G, Air Tractor AT502B, and mid-sized helicopter models in forward motion. Wake encounters were constructed to ensure that the UAS flew through aircraft wakes near the center of the rotation shortly after that aircraft's passage. The simulations were executed twice, one with the wake-generating aircraft opposed and roughly head-on to the UAS and then 90° to the UAS.

The results were plausible when compared to previous research and accounting for the difference in fixed-wing performance vs. multirotor performance: As the wake-generating aircraft became smaller, the wake effects on altitude and attitude displacement ranged from major for the 747 to nearly negligible for the 172. The rest of the aircraft wake effects from crewed aircraft sizes of the type expected to be encountered a) at common UAS altitudes and b) in shielded spaces remained easily recoverable to negligible.

The implication for safety-of-flight issues is that there remains a small residual risk of displacement or upset that pushes the aircraft into proximity of transmission lines. Otherwise, the simulations do not currently show elevated risk compared to the risks already inherent in UAS/crewed traffic encounters. The remaining exception would be the effects of helicopter rotor wash pushing down on a UA. This, too, presents a scenario where failures of separation have already occurred. UAS aircraft could certainly be pushed down by sustained rotor wash into a transmission line. The safety failure, however, is that of separation; the UAS aircraft should never have come to be beneath the CA. This prospect, coupled with the other wake turbulence results, points toward planning and effective traffic separation.

The overall need, in this case, is for traffic location and intention awareness. When in a potentially hazardous environment such as power lines, the flight planning and timing of a given mission should be made available to other traffic that may be in the area. For powerline related activities, it can be assumed that the power authority in charge of the transmission lines would be responsible for planning missions to account for this, even in a theoretical case where two different entities, such as contractors, may be at work on the lines. Otherwise, normal guidance on sensor and DAA system equipage should be followed.

Other unusual scenarios exist. One example is the possibility of large aircraft passage like a transport category airplane crossing well above the UAS's path posing a risk, but it is assumed that this is restricted to locations below approach/departure paths near airports. In those scenarios, prudent planning and alternate means of inspection likely remain the best mitigation.

One final future case might be a scenario where many UAS have been granted passage through a power corridor for transport purposes. In this case, a comprehensive rules structure for reserving and blocking off airspace on a timed basis may be the best approach.

4.4 Wind Turbulence Effects on UAS During Powerline Inspections

The constant crosswind analysis yielded important insights into the wind speed limits that the UAS can withstand near powerlines without crossing the electromagnetic unsafe boundary; however, the wind is inherently turbulent and characterized by its transient and stochastic nature. This phenomenon necessitates further investigation to understand how these inherent traits affect a UAS when operating in proximity to powerlines. Several studies have investigated the impact of wind gusts on UAS in various contexts. For instance, Schiano et al. (2014) used an experimental setup with a wind tunnel and found that high wind gust values induced UAS destabilization, affecting aircraft attitude. Fernández et al. (2017) highlighted the pronounced effects of high-intensity wind gusts on UAS operations, particularly during tasks such as wind turbine inspections. They showed how the UAS struggled with stabilization, often resulting in actuator failures. Wang et al. (2020) and Yuan et al. (2020) described the disturbance of flight dynamics caused by random wind gusts transferring their kinetic energy to UAS, resulting in jittering effects. Consequently, critical UAS attributes, including attitude, speed, and position consistently deviated from their intended control directives, hindering their ability to keep maintain their desired trajectories.

A reliable estimation model for wind gusts is essential for simulating their impacts on UAS. Given the turbulent and stochastic nature of wind gusts, a numerical statistical model is the best approach for estimating and implementing their values. Numerous models exist for this purpose, including the Log Normal (Baran and Lerch 2015), Exponential (Yan et al. 2022), and Rayleigh (Pishgar-Komleh et al. 2015) distributions; however, one of the most widely utilized models for wind and wind gust estimation is the Weibull distribution (Seregina et al. 2014; Azad et al. 2015; Gryning et al. 2016; Katinas et al. 2017; Shu and Jesson 2021; Sukkiramathi and Seshaiah 2021). Its flexibility allows it to effectively capture the characteristics of wind speed data, particularly in natural phenomena such as turbulence and gusts. This adaptability aligns with the reality that strong wind speeds are infrequent, with moderate and light winds being much more commonplace. The Weibull distribution is positively skewed (Rinne 2008), which perfectly suits such scenarios. Moreover, observations of wind speed data from diverse locations consistently demonstrate that wind speed distributions approximate a Weibull distribution (Seregina et al. 2014; Azad et al. 2015; Gryning et al. 2016; Katinas et al. 2017; Shu and Jesson 2021; Sukkiramathi and Seshaiah 2021).

4.4.1 Methodology

The Weibull distribution was adopted to model wind gusts due to its countless benefits, as highlighted above (Almalki and Nadarajah 2014). This distribution is characterized by the Cumulative Distribution Function (CDF) $F(x)$, represented as

$$F(x) = 1 - \exp\left(-ax^{b}\right), \tag{14}$$

and the Probability Density Function (PDF) $f(x)$

$$f(x) = abx^{b-1}\exp\left(-ax^{b}\right), \tag{15}$$

where a >0 and b >0 are the scale and shape parameters of the distribution, respectively, and x represents the speed of the wind for the type of wind being analyzed, static or gust. The CDF quantifies the likelihood of the wind or wind gust speed being below a certain threshold x, while the PDF characterizes the probability density across the entire range of possible values for wind gust speed.

Given that the wind and wind gust models conform to the Weibull distribution, the scale and shape parameters need extrapolation from actual wind data collected from weather stations. Seregina et al. (2014) and Shu and Jesson (2021) developed the Weibull distribution for wind using data from the UK and Germany. Seregina et al. (2014) performed a linear regression to calculate the scale and shape values from more than 10 years of data collected from several stations across Germany. After developing the model, the authors derived the formula for the mean wind gust speed value u_g from the value of the mean wind speed u_w

$$u_g = \left(\frac{a_w\left(u_w{}^{b_w}\right)}{a_g}\right)^{\frac{1}{b_g}}. \tag{16}$$

where a_w, b_w are the scale and shape parameters of the wind, respectively, and a_g, b_g are the scale and shape parameters of the wind gust, respectively.

Wind data from Tiger Mountain, WA, were extracted to find the Weibull parameters for the simulation site used herein. The development of a distribution model proved unfeasible due to the insufficiency of precise data for that specific site. An accurate assessment of wind gusts necessitates a high temporal resolution of measurements (Suomi and Vihma 2018). As an alternative, a German location (BRAUNLAGE), mirroring the natural attributes of Tiger Mountain with a natural corridor (Figure 56) was selected, and its parameters were utilized.

Figure 56. Natural corridor of the selected BRAUNLAGE (Germany) station for wind model development.

From the BRAUNLAGE location, the scale parameter was estimated to be 26.688 and the shape value was estimated to be 2.05. The Weibull distribution of the gust speed using these values is shown in Figure 57.

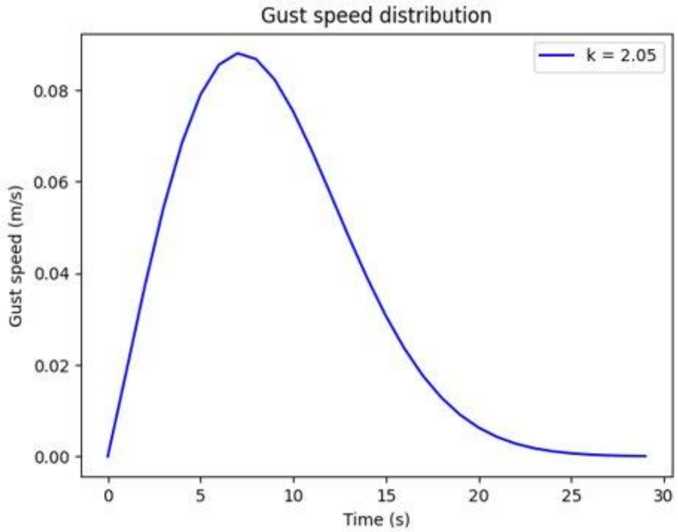

Figure 57. Weibull distribution for wind gusts.

4.4.2 Results

A series of simulations were executed to study the impact of wind gusts on a UAS operating in proximity to powerlines, considering both multirotor and fixed-wing configurations. These simulations were based on generating randomized wind gust magnitudes using the Weibull distribution model. This model's implementation led to the derivation of gust speeds ranging from 2 m s^{-1} to 35 m s^{-1} (Figure 58). For this scenario, the UAS was flown along a path parallel to the powerlines at a distance of 9.1 m.

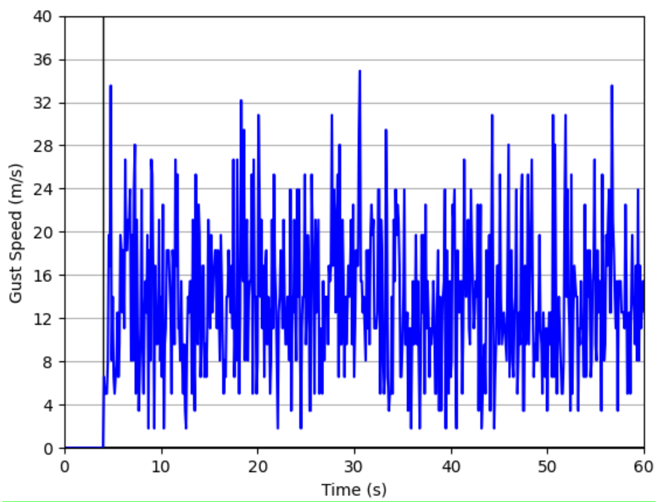

Figure 58. Wind gust simulation distribution.

The influence of wind gusts on the UAS were measured using various performance metrics, the primary being the ability to maintain a safe distance from EMI: 5.1 m for the 765 kV transmission tower used in these tests. Results were primarily derived from analyzing the UAS's horizontal and vertical distances from the powerlines. Additionally, the rate of change in attitude angles, a crucial parameter for comprehending the controller's response, were analyzed.

The UAS exhibited a deviation from its intended trajectory in both fixed-wing and multirotor scenarios when challenged with wind gusts. In both cases, the UAS did not manage to return to its original flight path. Instead, it persistently tried to regain stability amidst the challenging gusts.

In the multirotor case (depicted in Figure 59a), a slight deviation from the original path was observed, accompanied by attempts to stabilize against the gusts. Notably, the multirotor adeptly never crossed the EMI safety boundary (5.1m). In contrast, Figure 59b shows the fixed-wing scenario where stabilization attempts proved ineffective, leading the UAS to cross the unsafe boundary, and even fly over to the other side of the powerlines.

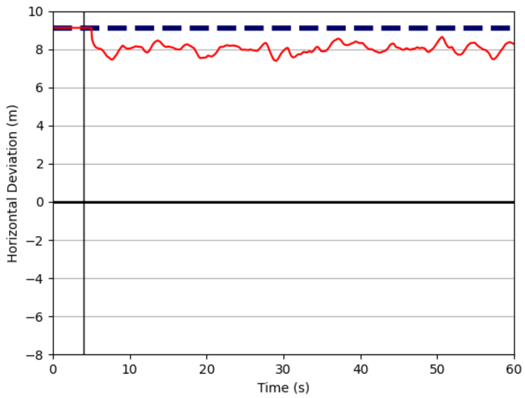

(a)

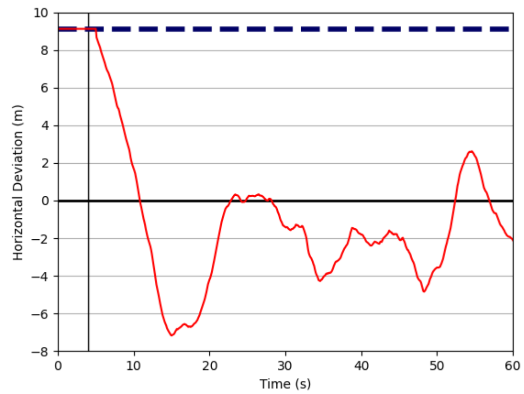

(b)

Figure 59. Horizontal distances from the powerlines for a starting distance of 9.1 m for (a) multirotor UA and (b) fixed wing UA.

Figure 60 illustrates the UAS vertical distances from the powerlines. Deviations were less than 0.44 m for the multirotor. However, gusts did have a strong impact on the fixed-wing aircraft. Struggling to maintain its planned path, the fixed-wing began ascending above the powerlines, ultimately reaching a distance of approximately 32 m. This outcome stresses the pronounced effect that wind gusts have on the maneuverability and stability of fixed-wing UAS, underscoring the challenges they face in maintaining their designated flight trajectory.

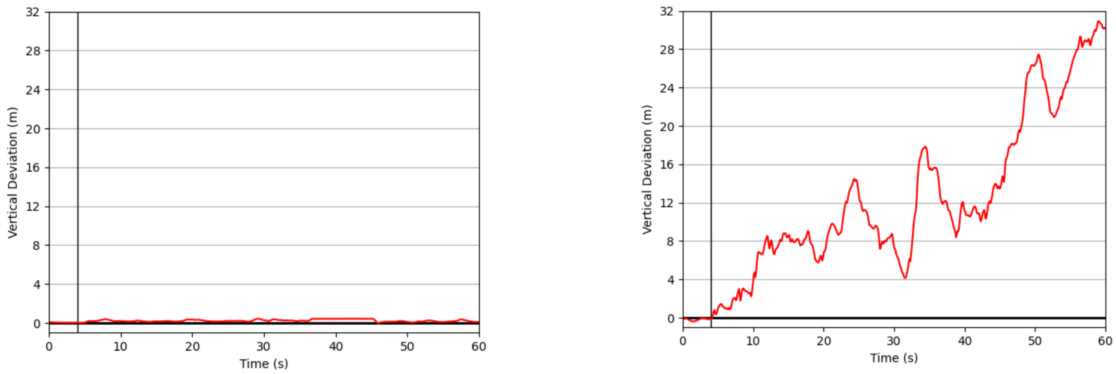

(a) (b)

Figure 60. Vertical distances from the powerlines for a starting distance of 9.1 m for (a) multirotor UA and (b) fixed wing UA.

Figure 61 shows the UAS controller responses displayed as pitch (c, f), roll (b, e), and yaw (a, d). The UAS attitude change increased to remain on course and withstand the wind gusts; however, the fixed-wing struggled with achieving stabilization, leading to a more pronounced impact on the angle changes compared to its multirotor counterpart (Figure 61). Particularly, the yaw angle reached a value of approximately 64° for the fixed-wing configuration. This significant deviation emphasizes the notable challenges encountered with the fixed-wing UAS in maintaining its intended orientation and stability under the influence of wind gusts.

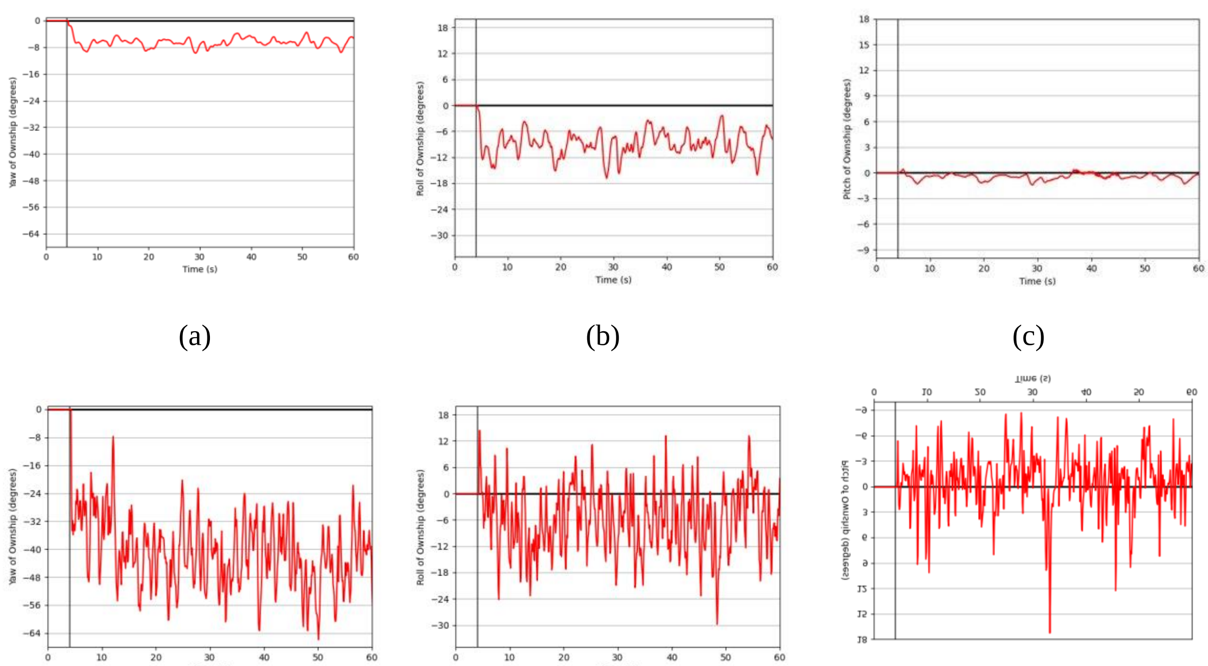

(a) (b) (c)

(d) (e) (f)

Figure 61. Attitudes for UA operating near powerlines with wind gusts for a starting distance of 9.1 m for (a,b,c) multirotor and (d,e,f) fixed-wing UA.

Table 18 summarizes the outcomes discussed earlier. The multirotor managed to maintain a safe separation from the powerlines even when wind gusts reached a velocity of 35 m s^{-1}, highlighting its adeptness in the face of gusts. On the contrary, the fixed-wing UAS encountered difficulties, resulting in a significant divergence from its intended trajectory. The implications of these findings are noteworthy, highlighting the necessity to align mission parameters with the UAS performance envelope. The performance of any given inspection mission should be evaluated in conjunction with the UAS's operational capabilities, particularly since diverse inspection tasks may necessitate a distinct maximum distance to ensure the acquisition of stable and high-resolution images. Optimal outcomes can be achieved by taking into consideration mission objectives with UAS capabilities and unsafe powerline boundaries, effectively addressing the dynamic interplay between wind-induced disturbances and operational requirements.

Table 18. Summary of wind gust impacts on UAS near powerlines.

UAS	Maximum Horizontal Deviation of the UAS (m)	Maximum Vertical Deviation of the UAS (m)	Maximum Roll Deviation (°); X (Right), Y (Left)	Maximum Pitch Deviation (°); X (Up), Y (Down)	Maximum Yaw Deviation (°); X (Right), Y (Left)
Multirotor	1.69	0.45	0, 16.9	0.4, 1.43	0, 9.75
Fixed Wing	16.3	33.13	14.38, 30.71	17.19, 12.95	0, 65.9

4.4.3 Conclusions and Recommendations

The outcomes of the investigation of the impact of wind gusts on UASs reveal a common pattern for both multirotor and fixed-wing configurations. In each scenario, the UAS could not return to the original path and tried to resist the effects of turbulence to fulfill its mission objectives. Despite wind gust speeds surging beyond 30 m s^{-1}, the UAS demonstrated a noteworthy resilience, evading catastrophic outcomes such as collisions or crashes, which can be attributed to the transient nature of these high-speed wind bursts (brief duration). The multirotor exhibited remarkable performance since it never crossed the safety boundary. These results provide invaluable insights for establishing guidelines concerning minimum safe distances from dangers related to electromagnetic disruptions. In contrast, the fixed-wing UA experienced more challenges owing to turbulence. It crossed the safety boundary and experienced significant vertical deviations as it struggled with the gusts. This divergence underscores the relative stability of the multirotor, which has a robust performance envelope and superior control over attitude angles. The multirotor's ability to withstand turbulent gusts more effectively is attributed to its inherent design, while the characteristics of the fixed wing UA results in it struggling to maintain both its course and safe distances from sources of strong EM fields.

5 IMPACTS ON GPS SYSTEMS/DATA

5.1 Introduction

Previous research has shown that GPS signal availability in urban environments range from 30% to 50% (Rufa and Atkins 2016) and is affected by factors such as multi path, significant signal attenuation, masking or even intentional acts such as denial or deception. As mentioned in Strümpfel et al. (2020), potential causes for GPS unavailability or sparse availability include shadowing effects caused by the presence of objects and buildings or deteriorated positioning performance due to multipath and bad available satellite geometry. Other causes for degraded navigation signals include erroneous, spoofed, jammed, or dropouts of GPS data that may result in UA position and navigation being incorrect. Additionally, operations in urban environments take place in concentrated radiofrequency environments with high levels of noise and degraded signals resulting in signal reflections and disruptions to wireless communication, air-ground communication, and satellite-based communication. If satellite signals are blocked by obstacles, then GPS measurements cannot be collected as illustrated in Figure 62.

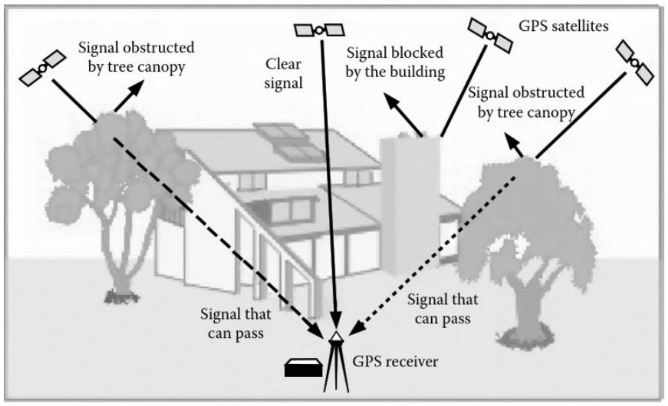

Figure 62. Obstructions and interference to GPS signals.

All mentioned causes for degraded navigation signals may result in a fly away beyond radio control, a flight into critical infrastructure, pedestrians, or obstacles, and possibly fatalities. Therefore, a quantitative risk-based assessment model that accounts for these threats is needed to address the growing demand for sUAS operations and their safe integration into the National Airspace System.

To support the risk analysis associated with sUAS operations and to improve the validation and verification process of guidance, navigation, and control algorithms, this report addresses the design, integration, and implementation of a high-fidelity simulation environment to facilitate the development of potential mitigation solutions and to increase the safety of sUAS operations. To demonstrate the capabilities of the developed tool, different navigation signal cases are implemented while executing a point-to-point mission trajectory within an urban scenario. These include nominal GPS conditions, dropouts, jamming, and reduced number of connected satellites. Additionally, for a quantitative risk assessment (e.g., severity and expected occurrence rate of a hazard), the tool uses a set of metrics included as part of the sUAS Airworthiness Assessment Tool (sAAT) developed by the MITRE Corporation (Breunig et al. 2019).

This report briefly describes the main aspects of the simulation environment, its components, and interactions followed by a description of metrics used in a preliminary risk assessment. A description of the test cases used to demonstrate the simulation tool capabilities and a performance analysis for the selected simulated scenarios are also presented.

5.2 Methodology

5.2.1 Simulation Environment

The architecture of the simulation environment presented in this report is modular. It is flexible enough to allow investigation of various sUAS operational scenarios along with design aspects such as processing of flight data; evaluation and testing of different guidance, navigation, and control schemes; analysis of several sUAS operations in normal and abnormal conditions; and risk assessment associated with such missions.

The main functional blocks of the tool and their interconnections are presented in Figure 63. The tool uses Matlab and Simulink interfaced with Gazebo to ensure maximum portability and flexibility. The simulation environment is modular and consists of the following main components:

- Graphical-interface Gazebo
- Communication module Robot Operating System (ROS)
- Aircraft model module
- Control system module
- Guidance and navigation module
- GPS model module
- Failures module

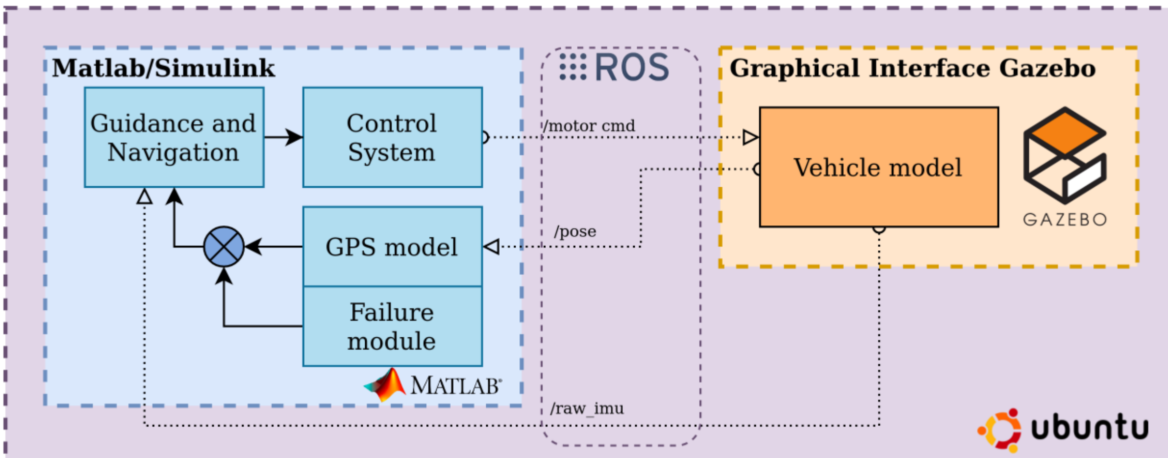

Figure 63. Simulation architecture.

5.2.1.1 Graphical-Interface Gazebo

The simulation environment includes the physical characteristics of the world and its interaction with the aircraft. The default physics engine used by the Gazebo platform is Open Dynamic Engine and uses the rendering library Object-Oriented Graphics Rendering Engine for a 3D visualization of objects and scenes. One of the advantages of Gazebo for world description is the collision feature, which provides a layer of realism in simulation scenarios especially for UAS operating near cooperative and non-cooperative obstacles. An example of a map created in Gazebo is presented in Figure 64. The map recreates a 70 m x 70 m area that includes different types of obstacles such as buildings, roads, people, and cars. Additionally, the world model includes a constant gravity field of 9.8 m s^{-2}, a geophysical location assignation for optional inclusion of magnetic field and GPS models, and constant customizable wind vectors.

a) Top View (b) Side View 3D

Figure 64. Simulation environment world.

5.2.1.2 Communication Module Robot Operating System (ROS)

Each software involved in the Simulation Architecture as presented in Figure 63 contains an ROS node to allow the exchange of information through an ROS network. The Gazebo simulator (gazebo node) publishes the pose information (pose topic) of the aircraft and the sensor data (raw_Imu topic) from an accelerometer and gyroscope. Matlab/Simulink (gazebo_ros_sim_92034 node) publishes the motor commands (motor_speed_cmd topic) for the UA control in Gazebo. Figure 65 shows the ROS network with the described topics and nodes.

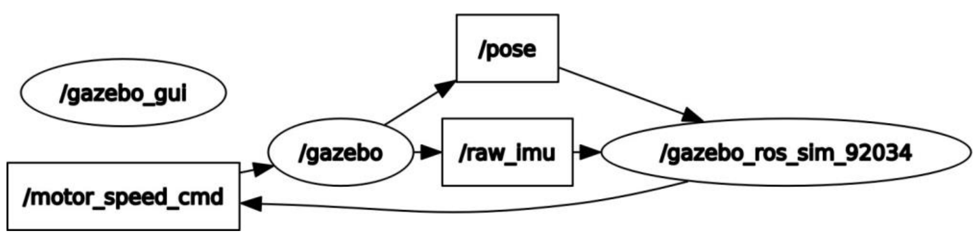

Figure 65. Simulation environment ROS network.

5.2.1.3 Aircraft Model Module

The aircraft represents the main object in the simulation environment, and is composed of several elements including physical properties given by a Computer-Aided Design (CAD) model. The aircraft selected for the Simulation Environment (SE) is a commercial 3DR RTF X8 drone, a multi-rotor composed of aluminum bars and a carbon-fiber body. It is powered by a 4S 10000 mAh battery and four T-Motor MT2216-9 1100 KV Brushless motors combined with four 10x3.3 carbon fiber propellers. This setup represents a mass of 2.087 kg, area of 787828.851 mm^2, and volume of 841576.252 mm^3. The average mission velocity for this drone is 6.5 m s^{-1}.

The information presented in Table 19 summarizes the aircraft power characteristics, payload allowance for different throttle setups, and the geometric characteristics of the aircraft. This information enables design of a 3D CAD model of the chosen aircaft as presented in Figure 66. Dimensions, inertia, and mass properties are included with the CAD description in a Universal Robot Description Format (URDF). The aircraft model is divided into five links for its Gazebo description, corresponding to the body, four propellers, and four joints defining a revolution relation of each propeller against the arms, allowing independent control of each propeller for aircraft control.

Table 19. Payload allowance for different throttle percentages (Aerofly Hobbies 2023).

Motor	Volts (V)	Propeller	Throttle	Amps (A)	Watts (W)	Thrust (gf)	Payload allowed (g)
MT2216 KV1100	14.8 (4S)	T-MOTOR 10x3.3CF	50%	6.2	92	590	273
			65%	8.8	130	760	953
			75%	11.3	167	900	1513
			85%	14.9	221	1100	2313
			100%	17.5	259	1190	2673

Figure 66. Gazebo 3DR physical model.

The mathematical model of the aircraft is simulated using a custom plugin in Gazebo attached to the physical properties of the object. The plugin receives the commanded velocity of each motor and generates the associated torque T_i and force F_i defined by

$$F_i = kw_i^2 \tag{17}$$

and

$$T_i = bw_i^2, \tag{18}$$

where w_i is the velocity of the i^th propeller, k is the lift coefficient, and b the drag coefficient.

5.2.1.4 Control System Module

The aircraft operation uses a linear controller for trajectory tracking. The control module is divided into two loops, an inner controller that minimizes attitude tracking errors and an outer controller that regulates position and velocity errors, as shown in Figure 67.

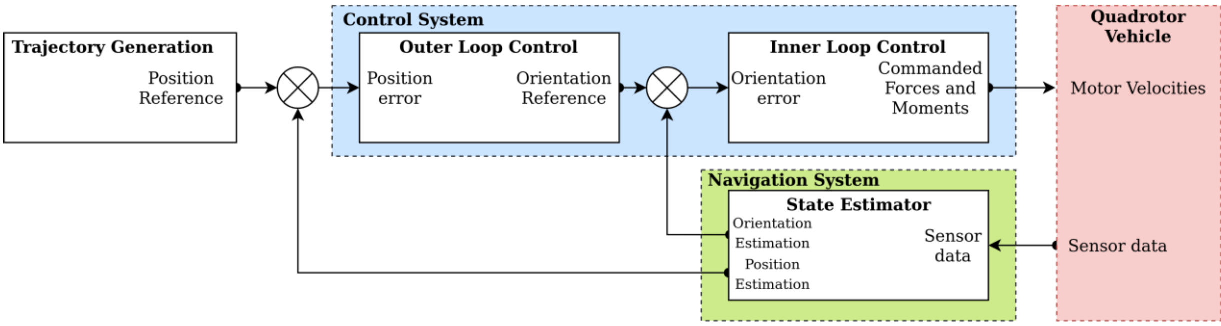

Figure 67. Block diagram of the control integration.

The controller uses the reference trajectory from the guidance block and the estimated states of the aircraft from the navigation system and calculates the required motor velocity inputs to achieve the reference states. The outer control generates orientation references to the inner controller based on the commanded accelerations derived from the position error and time constraints. Solving for the desired accelerations and using Newton's second law, a relation between the desired heading and the roll Φ_{ref} and pitch θ_{ref} angles is obtained as (Mellinger 2012)

$$\Phi_{ref} = \frac{1}{g}((\ddot{X}_{ref}\, sin(\Psi_{ref}) - \ddot{Y}_{ref}\, cos(\Psi_{ref})), \tag{19}$$

$$\Phi_{ref} = \frac{1}{g}((\ddot{X}_{ref}\, cos(\Psi_{ref}) + \ddot{Y}_{ref}\, sin(\Psi_{ref})) \tag{20}$$

and

$$\Psi_{ref} = \text{atan}\left(\frac{V_{y\_ref}}{V_{x\_ref}}\right), \tag{21}$$

where Ψ_{ref} is the reference heading and $\ddot{X}_{ref}$ and $\ddot{Y}_{ref}$ are the accelerations in the *X* and *Y* directions, respectively. V_{x_ref} and V_{y_ref} are the desired velocities in the *X* and *Y* directions, while *g* is the gravity acceleration.

Given the reference attitude angles provided by the outer controller, the inner controller calculates the attitude error and outputs the desired forces F_z and moments τ_Φ, τ_θ, τ_Ψ to control the aircraft of mass *m*. The control law uses an internal linear structure defined as

$$\tau_\Phi = k_d\left(\dot{\Phi}_{ref} - \dot{\Phi}\right) + k_p\left(\Phi_{ref} - \Phi\right) + k_i \int\left(\Phi_{ref} - \Phi\right), \tag{22}$$

$$\tau_\theta = k_d\left(\dot{\theta}_{ref} - \dot{\theta}\right) + k_p\left(\theta_{ref} - \theta\right) + k_i \int\left(\theta_{ref} - \theta\right), \tag{23}$$

$$\tau_\Psi = k_d\left(\dot{\Psi}_{ref} - \dot{\Psi}\right) + k_p\left(\Psi_{ref} - \Psi\right) + k_i \int\left(\Psi_{ref} - \Psi\right), \tag{24}$$

and

$$F_z = k_d\left(\dot{Z}_{ref} - \dot{Z}\right) + k_p\left(Z_{ref} - Z\right) + k_i \int\left(Z_{ref} - Z\right)\frac{m}{\cos\theta\cos\Phi}. \tag{25}$$

The control coefficients k_d, k_p, k_i are the derivative, proportional, and integral actions, respectively. Finally, the input velocity commands given by the controller are sent to the aicraft dynamics in Gazebo using ROS, while the sensor data are constantly published and processed by the navigation module.

5.2.1.5 Guidance and Navigation Module

Different algorithms for guidance navigation are implemented in Matlab/Simulink, and use ROS topics to exchange control commands to the aircraft model in Gazebo. These techniques were selected based on low-cost solutions currently being used by commercial sUAS (Skog and Händel 2005).

First, the trajectory reference is generated by performing a cubic spline fit of the desired way-points along with the desired timestamps. This provided a continuous/differential trajectory to the control system with implicit velocity and acceleration requirements.

The navigation algorithm integrates the accelerometer, gyroscope, and GPS data which corresponds to a loosely coupled Inertial Navigation System (INS) with GPS architecture based on aircraft error dynamics as shown in Figure 68. The architecture utilizes an Extended Kalman Filter (EKF) to estimate and compensate errors from the INS based on GPS/Global Navigation Satellite System (GNSS) observations and knowledge of the noise characteristics from all the sensors.

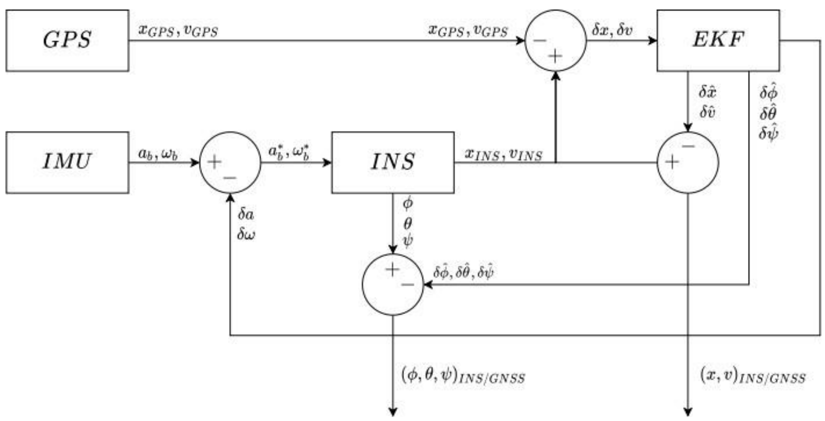

Figure 68. Loosely coupled INS/GNSS architecture.

Within the navigation module, it is desirable to compensate for errors introduced by the sensor, such as bias and noise, before they are provided to the INS mechanization. The following fifteen states-vector is defined using nonlinear dynamic equations and are used within the EKF for error estimation

$$x = [\delta x, \delta y, \delta z, \delta v_x, \delta v_y, \delta v_z, \delta \Phi, \delta \theta, \delta \Psi, \delta p, \delta q, \delta r, \delta b_{a_x}^b, \delta b_{a_y}^b, \delta b_{a_z}^b]^T. \quad (26)$$

The biases estimated with the EKF are used then to correct the upcoming measurements for the consequent iterations. Note from Figure 68 that the position, velocity, and angular states corrections are not used in the feedback, but as a direct output to the navigation system.

5.2.1.6 GPS Model Module

The GPS system is subject to several sources of error associated with communication systems. These sources of error contribute to abnormal or inaccurate measurements of critical sUAS flight information regarding position, velocity, and time solutions. Some of these errors correspond to the hardware and signal acquisition capabilities of the GPS receiver on-board the aircraft or the surrounding environment. In addition to these natural processing errors, GPS signals can also be subject to signal-based attacks; these errors and attacks can degrade or seize GPS systems leading to critical degradations of sUAS flight capabilities.

The simulation environment follows a modular structure within MATLAB and Simulink. This environment provides a portable, flexible, and extensible capability for new sUAS models and autonomous flight algorithms, and is capable of emulating flight hardware with high fidelity modeling. The critical flight hardware chosen for simulation modeling is a GPS receiver. This subsystem is classified as a critical flight system for sUAS systems as it provides position and velocity data for the aircraft in relation to the surrounding environment; additionally, this flight system is prone to signal spoofing attacks, signal hacking, signal dropouts, and environmental effects. The GPS model simulates GPS satellite acquisition, signal dropout, and attenuation, and allows various anomalies to be injected. For this study, the research team developed a GPS-module that would represent typical systems that are commercially available. A high-fidelity GPS module that would include transmission, acquisition-receiver, modulation and other specific electronic and signal components was not included in this project. However, several models including dropouts, jamming, shadowing, and multipath were developed to analyze the effect of these GPS-degraded cases on mission performance. The use of more sophisticated GPS-devices, with higher fidelity models, that usually include countermeasures to GPS-degraded effects could be included in a risk assessment, as discussed in Section 5.2.2, by reducing the probability of aircraft hardware failure or reducing the probability of collision through implementation of mitigation techniques. With this model, the impact of each flight system's performance can be characterized, and mitigation methods can be devised to increase robustness to various in-flight anomalies. The GPS Acquisition model is depicted in Figure 69.

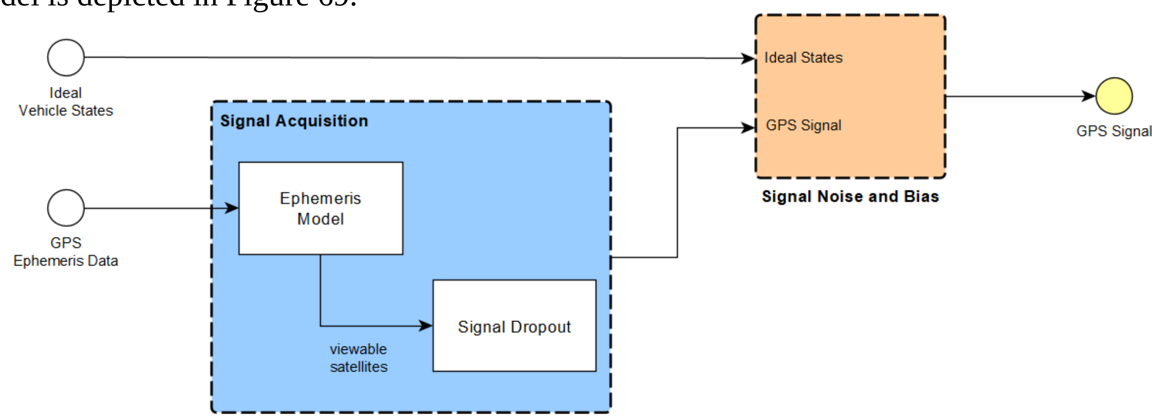

Figure 69. GPS model block diagram with satellite acquisition.

GPS signal acquisition utilizes the GPS constellation ephemeris data to determine the number of satellites that are within line of sight of the sUAS. These ephemeris data are provided by the National Aeronautics and Space Administration (NASA) and the European Space Agency (ESA) Earthdata platform providing weekly GPS ephemerides. The satellite orbit data are defined at a specific epoch and the GPS week number is transformed to Julian date and to the user location. The signal acquisition model simulates the acquisition time and GPS signal dropouts that can occur within urban environments. Once the aircraft location is specified and the GPS ephemerides are converted into a more readily useful format for propagation, the number of GPS satellites connected to the sUAS receiver is determined and updated throughout the simulation time frame.

After the number of GPS satellites that can be acquired by the sUAS receiver is determined, the signal dispersion and User Equivalent Error (UEE) are determined. The UEE is the statistical summation of system errors for the acquired GPS system (Kaplan and Hegarty 2005). For typical civilian use cases, the available GPS systems provide a single frequency receiver capable of achieving a UEE of 5.5 m with a 95% confidence level (GPS SPS PS Standard, 2020). In many cases, terrestrial GPS receivers will lose signal with GPS satellites either due to the environment or the natural orbital dynamics of the GPS constellations. When these signal dropouts occur, position and velocity data received and estimated by the sUAS can become less accurate with higher signal-to-noise ratios. The process error is propagated for each GPS state generating the sUAS aircraft states as estimated by the GPS receiver; this transformation of the ideal aircraft states to GPS measured states is defined by

$$Y(t) = X(t) + K * P(u) * W(t), \quad (27)$$

where $X(t)$ is the ideal aircraft state, K is a user defined noise gain, $P(u)$ is the UEE defined by a second-order polynomial, u is the number of acquired satellites from the GPS constellation ephemerides data, and $W(t)$ is the Gaussian process noise. The GPS model provides a useful and extensible system for characterizing GPS performance and environment threats to an sUAS in flight. This process transforms perfect aircraft states into noisy signals with position and velocity dispersion representative of commercial-based hardware.

5.2.2 Risk Assessment Architecture

In line with previous studies, for a quantitative risk assessment (e.g., severity and expected occurrence rate of a hazard), this study uses a set of metrics included as part of the sAAT developed by the MITRE Corporation (Breunig et al. 2019). These metrics are useful to quantify the risk of fatality to third-party people by accounting for aircraft and mission characteristics.

The rate of fatality due to sUAS failure is given by

$$C = P_{fail} * \rho_{people} * S * A_{lethal} * P_{collide} * P_{fatality}, \quad (28)$$

where C is the number of fatalities per flight hour, P_{fail} is the probability of aircraft failure per flight hour, ρ_{people} is the density of people at risk per square unit area, S is a shelter factor (a dimensionless quantity between zero and one), A_{lethal} is the lethal area of the aircraft on impact, $P_{collide}$ is the probability of collision that could be reduced with a mitigation strategy, and $P_{fatality}$ is the probability of fatality (Wieser and Brunner 2000).

5.2.2.1 Aircraft Failing Parameter

The probability of the aircraft failing P_{fail} is affected by different factors such as loss of control, component failure, damage to aircraft, among others. This probability depends on the failure rate, which can be expressed as Mean Time Between Failure. Usually, this information can be obtained from the developer company or from flight test data. However, due to lack of information for this analysis, data used in the sAAT model are leveraged (shown in Table 20). The category of the aircraft used in the SE is within the Mini weight category with an estimated failure per hour rate of 1×10^{-3}.

Table 20. Nominal aircraft failure rates by weight class from (Breunig et al. 2019).

Weight Category	Failure Rate Per Flight hour
Micro (0.55 lb.)	1E-2
Mini (0.56 – 4.4 lb.)	1E-3
Limited (4.5 – 20.9 lb.)	1E-4
Bantam (21-55 lb.)	1E-5

5.2.2.2 Pedestrians Exposed

For a realistic calculation of the pedestrian strike probability, it is necessary to quantify the population in the operational area. The city of Orlando, Florida, was selected as a reference area. Using Geographic Information System and remote sensing databases, a geoprocessing analysis was performed on population and land use data to estimate population density. For population data, the LandScanTM Global Population database was used with a 1 km resolution distribution that represents an ambient population average over 24 hours.[4] For land-use data, an open-source database for the city of Orlando was used. The results in units of people per square kilometer are shown in Table 21. The population density information was provided to the SE based on the existent infrastructure as illustrated in Figure 70.

Table 21. Estimated population sensity According to landuse type in Orlando, FL.

Land Use Type	Population Density (pp km^{-2})
Multi-Family	1,765.79
Commercial	1,294.09
Office	1,243.46
Hotel	1,065.37
Single Family	1,000.48
Industrial	609.56
Hospital/Medical/RSSF	411.00
Public Benefit Use	349.42
Unknown	340.00

[4] This product was made utilizing the LandScan 2019 High-Resolution Global Population Data Set copyrighted by UT-Battelle, LLC, operatorof Oak Ridge National Laboratory under Contract No. DE-AC05-00OR22725 with the United States Department of Energy. The United States Government has certain rights in this Data Set. Neither UT-BATTELLE, LLC NOR THE UNITED STATES DEPARTMENT OF ENERGY, NOR ANY OF THEIR EMPLOYEES, MAKES ANY WARRANTY, EXPRESS OR IMPLIED, OR ASSUMES ANY LEGAL LIABILITY OR RESPONSIBILITY FOR THE ACCURACY, COMPLETENESS, OR USEFULNESS OF THE DATA SET.

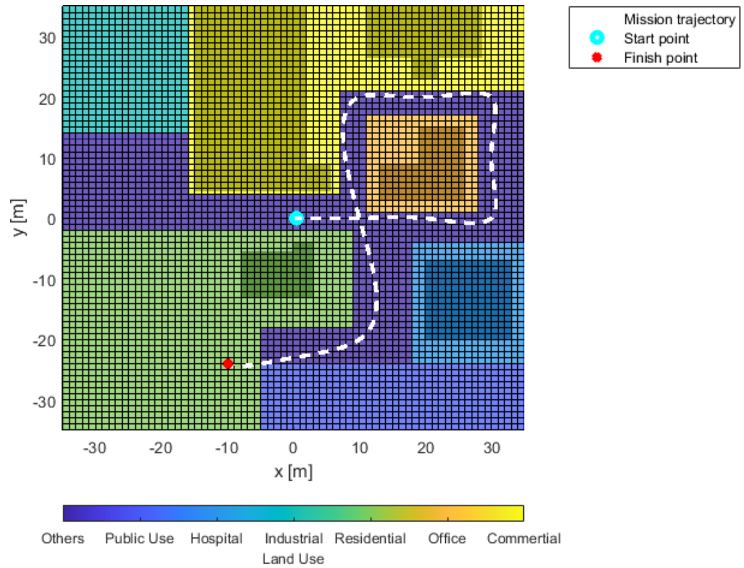

Figure 70. Land use area classification for simulation environment world.

5.2.2.3 Collision Course with Pedestrian

The likelihood that the aircraft is on a collision course with a pedestrian is related to aircraft characteristics and surrounding population density. One approach to estimating an impact area A_{lethal} at any instance in time is to assume that the aircraft is limited to a simple, parabolic trajectory based on an initial altitude and horizontal speed. Notice that many other trajectories could be considered in this analysis. However, for simplicity of the analysis, a parabolic trajectory was chosen to calculate the average and maximum values for velocity and height when the GPS-degradation is introduced (at time 35 – 40 s). This assumption is somewhat conservative since a parabolic trajectory would represent a case when complete loss of control of the vehicle is present. Regardless of this assumption, this test case provides preliminary insight into the worst-case scenario that could be experienced. It is also important to mention that A_{lethal} is only an estimation of the area where there is a higher probability that the vehicle is on a collision course with a pedestrian, which also depends on the population density of such an area. This density of population is captured by ρ_{people} as the density of people at risk. Therefore, other factors such as sidewalks outside this area were not considered implicitly in this study. Solving for horizontal distances travelled, as the radii of two circles, the ‘average’ and ’maximum’ impact areas were then calculated. The difference between these circles yielded the resulting A_{lethal} area. This is illustrated in Figure 71.

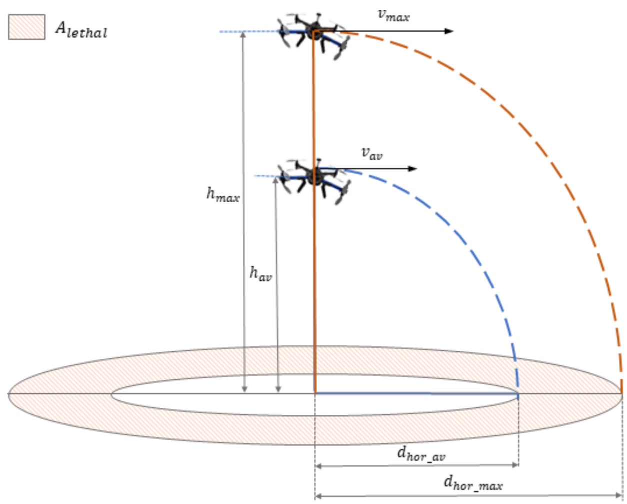

Figure 71. Estimated zone of impact of a falling sUAS.

5.2.2.4 Not Avoided Collision

Collisions may be avoided by implementing different mitigation techniques that reduce the probability of collision. For this SE analysis, the worst-case scenario is assumed with no mitigation techniques onboard. Therefore, $P_{collide}$ is assumed equal to 1.0.

5.2.2.5 Collision Resulted in Fatality

Aircraft configuration and characteristics are important for estimating the energy during a collision. $P_{fatality}$ is calculated based on the Kinetic Energy (KE) that represents the transferred energy from the aircraft to the obstacle. In the sAAT model, $P_{fatality}$ is calculated as

$$P_{fatality} = \frac{1}{1+e^{-k(E-E_0)}}, \tag{29}$$

where k is the shape parameter and is held constant, E_0 represents the KE associated to the average velocity of the mission, and E represents the KE associated to the impact velocity. Using the 3DR RTF X8 quadrotor's mass and average velocity during a mission (6.5 m s^{-1}), the shape of the fatality curve shown in Figure 72 was obtained.

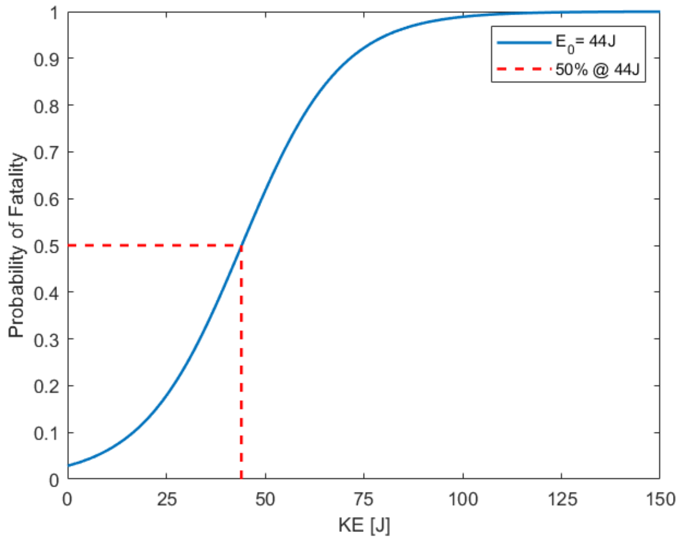

Figure 72. Shape of fatality curve, given a kinetic energy E_0 associated with the average velocity of the mission, usually 44 J.

5.2.2.6 Shelter Factor

Pedestrian behavior is continuously changing; therefore, a shelter factor is appropriate for estimating a percentage of the population that is safely covered by buildings or other objects from the direct impact of a sUAS crash. A shelter factor equal to 1.0 represents a flight operation above people who are directly exposed to impact, whereas a shelter factor of 0.0 represents a population that is entirely sheltered. To estimate this factor, data from the Environmental Protection Agency's (EPA's) Exposure Factors Handbook (Table 22) are used, which provides recommended values for activity patterns for indoor and outdoor activities (EPA 2011). Based on the age group of 18 to < 65 years, the shelter factor was calculated as 0.195.[5]

Table 22. Recommended values for activity patterns.

Age Group	Activity Patterns	Mean (min day^{-1})
18 to < 65 years	Indoors	1,159
	Outdoors	281

5.3 Numerical Simulation for Risk Assessment

Numerical simulations were performed to evaluate four cases associated with GPS signal degradation that compromise sUAS flight capabilities. Each test scenario simulates a point-to-point mission such as a small package delivery in an urban environment. The defined trajectory requires the aircraft to navigate through several obstacles typical of an urban environment mission. The SE characteristics used for the test cases are:

- The mission is performed at a constant altitude of 6.0 m.
- The time of failure is defined to occur between 35 and 40 s.

[5] Ratio of the amount of time outdoors (281 minutes/day) to the number of minutes in a day (1440 minutes).

- Nine satellites are available except during the time of failure period, when a specific form of signal degradation is applied, according to each test case.

5.3.1 Test Cases

For each case, four types of simulations were performed in order to gather data and analyze the parameters required for the preliminary risk assessment:

- Case 1 - Nominal Conditions: At an altitude of approximately 20,200 km, a nominal constellation of 24 GPS satellites is enough to ensure that there will be at least four satellites visible, at any unobstructed site on Earth (Bossler et al. 2010). In Case 1, nine GPS satellites are used at all times, which provides highly accurate position and velocity estimations. Additionally, there is no signal degradation during the time of failure and the aircraft is able to successfully complete the commanded mission.
- Case 2 - GPS Dropouts: Any event that causes GPS data to be degraded or denied (unavailable) can be classified as a factor contributing to a dropped GPS signal (Kubo et al. 2020). GPS dropouts might result in loss of sUAS control, crossing airspace boundaries, flying beyond radio control, or sudden climbing, leading to fatal accidents. Within the SE, GPS dropout was simulated by reducing the available satellites until loss of GPS signal (e.g., between 0 and 3 satellites). With these conditions, the EKF will not correct estimates from INS based on GPS measurements, reducing estimation performance, and leading to errors in the estimated position and velocity of the aircraft.
- Case 3 - GPS Jamming: GPS jamming is a common problem usually associated with cyber-attacks, where significant radio frequency noise is transmitted to cause data inaccuracies, signal locks, or replacement of the GPS measurement by the jamming signal (Yu 2012; Leonardi and Piracci 2018). Within the SE, jamming was simulated as a lock to the current GPS position at the time of failure, causing erroneous position and velocity estimates from the navigation system, as it continues to operate based on non-updated GPS data.
- Case 4 - GPS Satellites Reduced: Although at certain times during the day enough satellites may be available simultaneously, periods of degraded satellite coverage caused by navigational signals being reflected or blocked by obstacles may occur (Bossler et al. 2010). Challenging zones are defined as areas where GPS satellites are not available or may be reduced. Potential causes for GPS unavailability or sparse availability include shadowing effects due to the presence of buildings or deteriorated positioning performance due to multipath and poor available satellite geometry (Strümpfel et al. 2020). To simulate this event within the SE, the number of available satellites was reduced to eight, six, and four during the time of failure.

5.3.2 Results and Analysis

After multiple simulation runs, i.e., five simulations for each case, the following are some findings:

- Case 1: The aircraft was able to complete the commanded mission with small trajectory deviations.
- Case 2: During the time of failure the aircraft performed sudden climbing and flew away from the limits of A_{lethal}.
- Case 3: During the time of failure the aircraft crashed within the A_{lethal} limits.
- Case 4 - GPS Satellites Reduced to 8: For all runs, the aircraft was able to execute the mission with small deviations from the commanded trajectory. No crashes occurred.

- Case 4 - GPS Satellites Reduced to 6: In one of the runs the aircraft flew away and did not complete the mission. For all other runs, the aircraft completed the mission with no crashes.
- Case 4 - GPS Satellites Reduced to 4: For two runs the aircraft was able to execute the mission. However, a significant loss of control during the time of failure was present. In the remaining runs, the aircraft crashed during the time of failure.

For all five runs for each case analyzed, Table 23 summarizes the average velocities ($\bar{v}_{ave}$), standard deviation velocities ($\bar{\sigma}\, v_{ave}$), maximum velocities ($\bar{v}_{max}$), standard deviation maximum velocities ($\bar{\sigma}\, v_{max}$), lethal area ($\bar{A}_{lethal}$), and standard deviation area lethal ($\bar{\sigma}\, A_{lethal}$).

Table 23. Averaged simulation parameters for each test case.

Parameter	Case 1	Case 2	Case 3	Case 4		
	Nominal	Dropout	Jamming	8 Satellites	6 Satellites	4 Satellites
$\bar{v}_{ave}$	2.27	16.76	6.3	2.44	2.00	4.12
$\bar{\sigma}\, v_{ave}$	0.026	2.06	1.91	0.09	0.11	11.85
$\bar{v}_{max}$	5.46	32.39	16.52	6.2	4.94	11.85
$\bar{\sigma}\, v_{max}$	0.24	3.65	3.60	0.69	0.55	4.15
$\bar{A}_{lethal}$	97.07	3009.3	1009.37	110.83	101.28	614.51
$\bar{\sigma}\, A_{lethal}$	10.4	642.80	381.57	32.65	57.06	436.08

To perform a preliminary risk assessment calculation, a run from each case was analyzed. The parameters for the selected runs are shown in Table 24. Using these data, the estimated risk assessment parameters to evaluate (28) were calculated.

Table 24. Simulation parameters for an example of each test case.

Parameter	Case 1	Case 2	Case3	Case 4		
	Nominal	Dropout	Jamming	8 Satellites	6 Satelites	4 Satellites
$\bar{v}_{ave}$ m s^{-1}	2.28	16.65	6.79	2.59	2.35	5.3
$\bar{v}_{max}$ m s^{-1}	5.23	32.43	17.19	6.56	7.13	12.97
$\bar{A}_{lethal}$ m^2	86.67	2996.07	1010.88	142.68	177.25	554.33

Table 25 shows the estimated risk assessment parameters and C, number of fatalities per flight hour, calculations. Figure 73 illustrates the differences in estimated *C* for each case. It is noted that the magnitude of the risk assessment results is conclusive, showing that the cases with higher risks are Case 2 - Dropout, Case 3 – Jamming, and Case 4 - Reduced Satellites 4. This is an important finding in the understanding of the risks when an aircraft is exposed to a specific form of GPS signal degradation.

Table 25. Risk assessment parameters and estimates using (28).

Parameter	Case 1	Case 2	Case3	Case 4		
	Nominal	Dropout	Jamming	8 Satellites	6 Satellites	4 Satellites
P_{fail}	$1x10^{-3}$	$1x10^{-3}$	$1x10^{-3}$	$1x10^{-3}$	$1x10^{-3}$	$1x10^{-3}$
ρ_{people} pp km^{-2}	749.0	776.0	902.0	812.0	953.0	900.0
A_{lethal} m^2	86.7	2996.1	1010.9	142.7	177.3	554.3
S	0.195	0.195	0.195	0.195	0.195	0.195
$P_{collide}$	1.0	1.0	1.0	1.0	1.0	1.0
$P_{fatality}$	0.22	1.0	1.0	0.51	0.67	0.99
C (fatalities (flight hr)$^{-1}$)	$2.84x10^{-6}$	$4.54x10^{-4}$	$1.78x10^{-4}$	$1.17x10^{-5}$	$2.21x10^{-5}$	$9.73x10^{-5}$

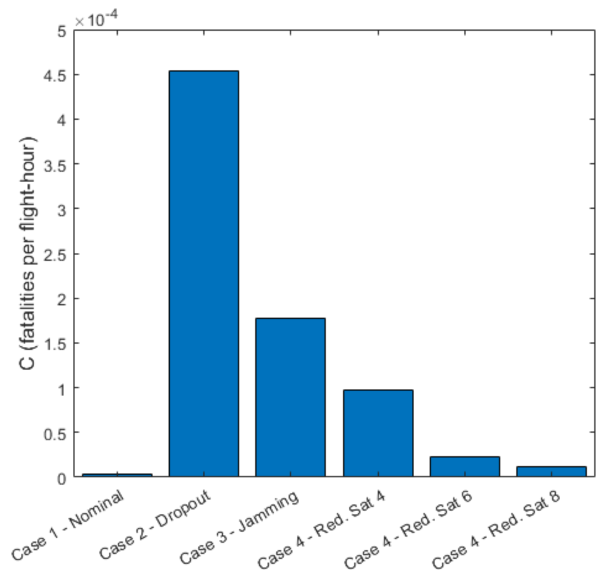

Figure 73. C value from a selected SE run for each test case.

A top view of the SE mission results from each of the examples analyzed for the risk assessment is provided in Figure 74. It is clear that there is a significant variation in the trajectory path and in the size of A_{lethal} for each case. Additionally, it is noted that the aircraft crashes in Cases: 2 - Dropout, 3 – Jamming, and 4 -Reduced Satellites 4. These results are consistent with the C results presented in Figure 73.

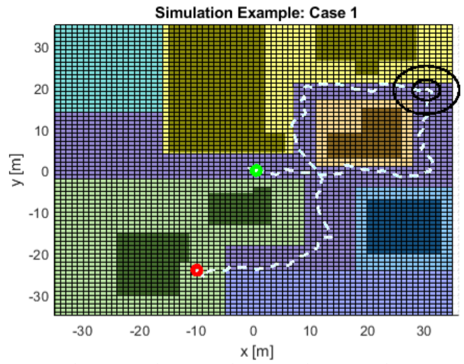

(a) Case 1: Nominal Conditions

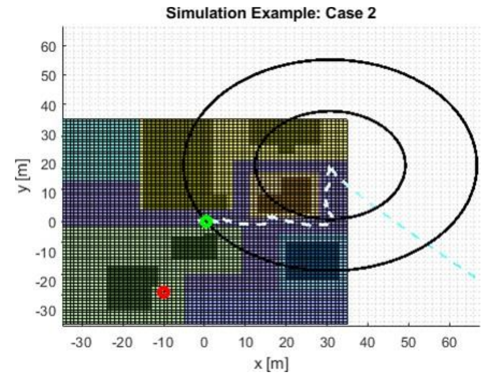

(b) Case 2: GPS Dropouts

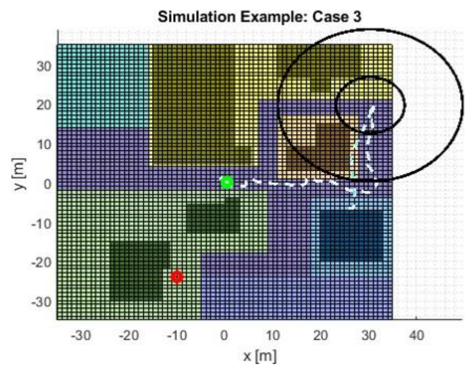

(c) Case 3: GPS Jamming

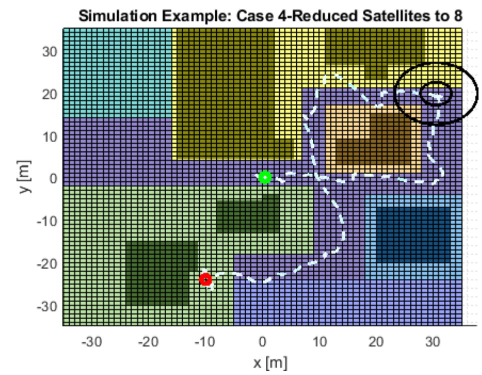

(d) Case 4: GPS Reduced Satellites

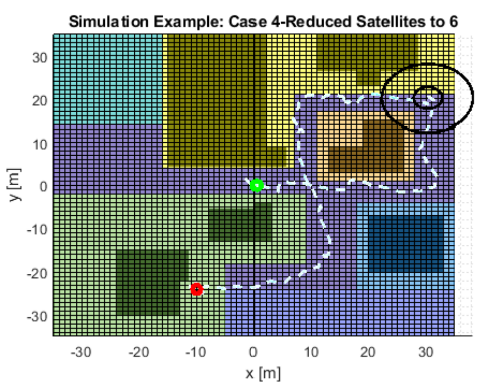

(e) Case 4: GPS Reduced Satellites

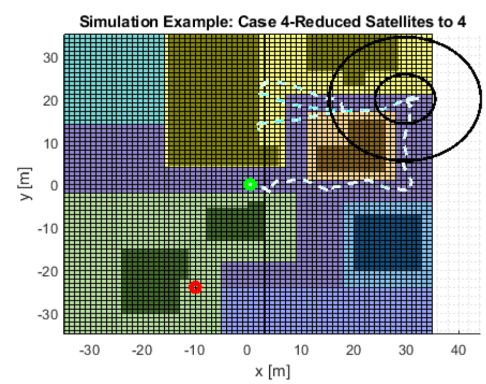

(f) Case 4: GPS Reduced Satellites

Figure 74. Simulation example for each test case.

5.4 Modeling of GPS Degradation for Risk Assessment

UASs are generally equipped with GPS that provide essential support to the navigation and control system by positioning the aircraft over the application area. However, diverse applications cannot use these positioning systems without experiencing degradation due to environmental conditions. An example is UA operations within urban environments, as depicted in Figure 75, where signal deterioration can occur due to building obstruction, signal multipath, shadowing effects, or jamming from strong electromagnetic sources (FAA 2012).

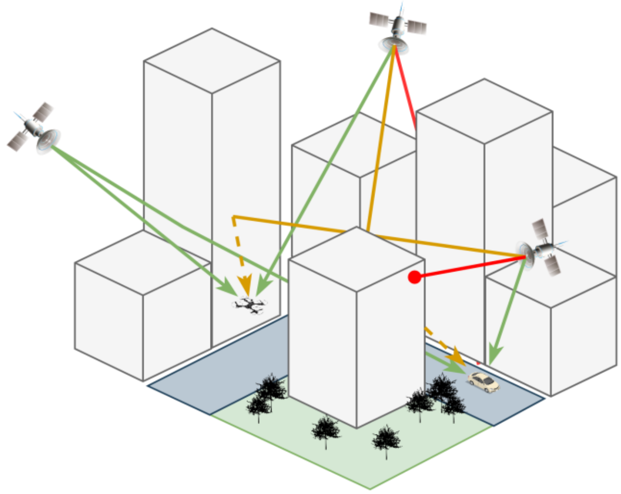

Figure 75. GPS signal (green), signal obstruction (red), and multipath (orange).

A communication link between a satellite and a receiver may be created not only through a direct path or direct Line-of-Sight but can be established with multiple indirect paths generated by signal bounces over reflective surfaces, which leads to multipath. According to Kos et al. (2010), a multipath error results from interference between two radio waves that have traveled paths of different lengths between the transmitter and the receiver. As a result, signal delays and phase problems can be introduced, degrading GPS signal accuracy. This phenomenon is common within urban canyons where streets are densely populated by tall buildings, potentially generating the conditions for the occurrence of signal obstruction and reflections (Smyrnaios et al. 2013). For instance, the flight integrity of UASs that strongly rely on GPS positioning can be severely affected since positioning errors will increase over time (Kan et al. 2018). Particularly, autonomous flight missions with multi-rotors require nominal conditions with high levels of precision in order to conduct the flight plans in a safe manner (Patrik et al. 2019; Strümpfel et al. 2020) and errors introduced due to signal deterioration can potentially compromise flight safety and the integrity of the surroundings. Techniques to provide consistency of service in GNSS-challenged environments include implementing additional sensors and positioning mechanisms along the GPS system to increase the sensitivity and robustness of aircraft control. For this study, is of interest to investigate the effects of different forms of signal degradation induced when operating in urban scenarios.

Although the GPS constellation is composed of thirty-one operational satellites (Wang et al. 2018), a minimum of four satellites is required to establish the location of a receiver with a certain degree of accuracy. Furthermore, inclusion of more visible satellites into the solution of the geometric problem can decrease the error variance; as a result, it has become a requirement not only to have the minimum required satellites to establish a position but to observe a higher number, along with good satellite geometry, to achieve desired levels of accuracy for autonomous missions (Isik et al. 2020). Based on this concept, it is known that the Dilution of Precision (DOP) value provides a measure of GPS accuracy based on satellite geometry and the number of visible satellites; therefore, it can be used as an indicator of GPS accuracy. For example, DJI commercial drones require a minimum of six satellites to rely on GPS outdoor navigation (MAVIC PRO 2017), while some propose 7 to 12 visible satellites to reduce redundancies and improve accuracy (Dutt et al. 2009, Isik et al. 2020).

Based on geometry calculations of visible satellites from a receiver location, this section assesses the impact of GPS signal degradation on the performance of aerial navigation in urban environments. Modeling of signal shadowing and multipath within a simulation environment is tested to monitor DOP coefficients. Further analysis of probabilities of collision is also presented using Monte Carlo simulations for different GPS degradation conditions.

5.4.1 GPS Modeling

The performance of autonomous missions is highly dependent on the integrity and continuity of its positioning system, often carried by GNSS due to its high overall accuracy and worldwide availability. However, several factors can significantly degrade GPS signal accuracy. Thus, integration of geometric models for signal blocking is presented in this report along with probabilistic approaches for testing multipath effects in a modular simulation environment (Gutierrez et al. 2022). A GPS model workflow is presented in Figure 76.

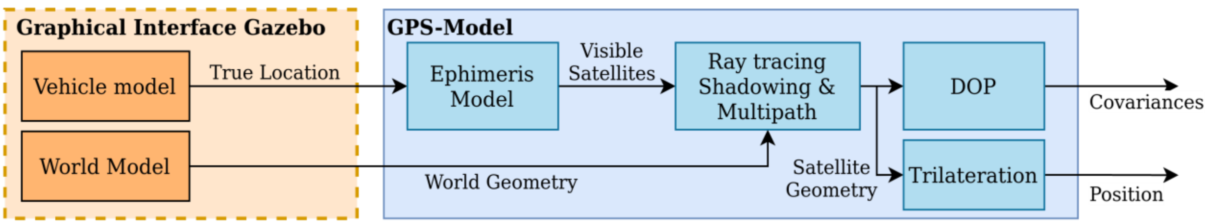

Figure 76. GPS model workflow.

5.4.2 Ephemeris Model

This simulation environment utilizes GPS constellation ephemeris data to determine the number of satellites that are within LOS of the aircraft. These ephemeris data are provided by the NASA and ESA Earth data platform, which provides weekly GPS ephemerides. Furthermore, the signal acquisition model simulates the acquisition time and GPS signal dropouts that can occur within urban environments. Once the aircraft location is specified and the GPS ephemerides are converted into a more readily useful format for propagation, the number of GPS satellites connected to the aircraft's receiver is determined and updated throughout the simulation time frame (Gutierrez et al. 2022). Furthermore, the corresponding geometric range is calculated for further modeling of multipath effects and shadowing checks by means of ray tracing and determination of impacts on the final DOP parameter.

5.4.3 Ray Tracing for Shadowing and Multipath Effects

The ephemeris data along with the ray tracing algorithms in local environments provides the corresponding visible satellites at any location of the UA within the area, allowing computation of DOP for the given geometry of the satellites within LOS. Therefore, an impact assessment of covariance variation in the guidance, navigation, and control architecture provided by the UAS model can be performed. A description is presented in the following subsections.

5.4.3.1 The Pseudo-Range Measurement

The pseudo-range measurement approximates the distance between a given receiver and a satellite and can be obtained by computing the corresponding offset of the three-dimensional coordinates and clock data of every satellite being tracked and of the antenna of the receiver (Langley 1999).

However, GPS pseudo-range measurements often contain errors caused by interference from ionospheric (D_{ion}) and tropospheric (D_{trop}) delays, multipath effects (ϵ), and receiver noise (w). Consequently, the pseudo-range measurement can be defined as (Teunissen and Kleusberg 2012; Kubo et al. 2020)

$$R = \rho + c(dt - dT) + D_{ion} + D_{trop} + \epsilon + w, \tag{30}$$

where R represents the pseudo-range, ρ is the geometric range to the satellite, and c is the speed of light. Furthermore, the geometric range or true range ρ is calculated as (Kaplan and Hegarty 2005)

$$\rho = \sqrt{(x_s - x_r)^2} + \sqrt{(y_s - y_r)^2} + \sqrt{(z_s - z_r)^2}. \tag{31}$$

Similar to the pseudo-range or code measurement, the phase is simultaneously measured as given by the carrier phase and represents the difference between the phase Φ of the receiver-generated signal and the signals at the transmission time. This carrier phase can be defined as

$$\Phi = \rho + c(dt - dT) - D_{ion} + D_{trop} + \Phi_{\epsilon} + \Phi_w + N\lambda \tag{32}$$

with $N\lambda$ defined as the carrier phase range ambiguity.

The magnitude of these effects can severely impact the accuracy of position estimation when compared to true range. Therefore, this research effort focuses on quantifying the error produced by multipath and receiver noise effects in the pseudo-range calculation along with degradation perceived in the trilateration process due to obstruction of signal caused by shadowing effects.

5.4.3.2 Multipath Effects

Multipath effects occur when the receiver obtains superposed signals from the same satellite sources due to the reflection of the original signals off objects present in the environment. The superposition of these reflected signals and the original signals in LOS yields a compound signal at the receiving antenna. Depending upon the relative phase between the signals, constructive or destructive interference affects the pseudo-range measurement (Smyrnaios et al. 2013). Often, multipath effects are a nuisance in GPS positioning and therefore its quantification becomes important.

A common approach reported in the literature to quantify multipath error when dual frequency is available is the multi-frequency Code-Minus-Carrier (CMC) (Teunissen and Montenbruck 2017; Medina et al. 2018). This technique is used to isolate multipath error and relies on observing the difference between code and phase measurements since both have common terms that are equal in both cases, resulting in

$$R - \Phi = 2D_{ion} + (\epsilon - \Phi_{\epsilon}) + N\lambda + (w - \Phi_w). \tag{33}$$

The carrier phase multipath and sensor noise error can be considered negligible compared to the pseudo-range magnitude, normally by about two orders of magnitude. On the other hand, the ionospheric divergence is estimated in diverse references when dual frequency measurements are available. Here the difference of both carrier-phases is taken since the multipath and sensor noise are negligible in both equations. Therefore, an expression denoted as dual frequency (L1 and L2) iono-corrected CMC is defined as

$$CMC = R_{L1} - \Phi_{L1} + \frac{2}{\alpha}(\Phi_{L1} - \Phi_{L2}). \tag{34}$$

By expanding these equations with all of the corresponding components in the code and carrier-phase measurements, the CMC becomes

$$CMC = \epsilon + \Phi_{\epsilon_{L1}} + \frac{2}{\alpha}\left(\Phi_{\epsilon_{L1}} - \Phi_{\epsilon_{L2}}\right) + \left(N\lambda_{L1} + \frac{2}{\alpha}(N\lambda_{L1} - N\lambda_{L2})\right). \quad (35)$$

As previously mentioned, the carrier-phase multipath and sensor noise errors are considered zero, and all the components related to phase ambiguities are condensed in a single term denoted as v, which will be considered as a constant value and works as a bias in the CMC. Thus, this implies (Medina et al. 2018)

$$v = N\lambda_{L1} + \frac{2}{\alpha}(N\lambda_{L1} - N\lambda_{L2}), \quad (36)$$

and

$$\epsilon = CMC - v. \quad (37)$$

Although the CMC is a metric well known for monitoring, characterizing, and measuring code range multipath errors, some literature proposes stochastic models to quantify this component since geometric solutions are challenging to solve, especially for antennas in motion. The multipath problem is a geometry-dependent problem and motion can severely degrade the performance of the monitoring process; hence, probabilistic and data-driven models are proposed for the characterization of the multipath model.

Some of the existing models for multipath effects that are independent of geometric calculations consider the variance of the multipath error as a random variable, as presented in (Medina et al. 2018). Moreover, error sources are correlated with the elevation angle, and simultaneous effects can be observed over the carrier-to-noise measurement C/N_0. Larger paths due to elevation angles and reflections increase the signal path and waves reach the antennas with different patterns, where antennas are not optimal. Thus, it is possible to consider the multipath error variance as a random variable such that

$$\sigma_\epsilon^2 \sim p(\sigma^2;\ \theta; C/N_0). \quad (38)$$

This expression proposes that the variance can be represented as a probability density function dependent on the elevation angle and the signal-to-noise ratio C/N_0 of the satellite. A popular choice for this distribution is an inverse-Gamma distribution. As suggested by the sigma-ϵ model, the signal strength is a good indicator of the quality of the pseudo-range measurement. Thus, characterizations of the C/N_0 parameter in areas of interest as is the case of urban environments can be performed in order to quantify multipath effects with probabilistic models (Kubo et al. 2020).

As a result, a characterization should include the parameters that affect the variance such that a model fitting needs to be performed for each θ and C/N_0. A reasonable modeling can be expressed as

$$\epsilon \sim \mathbb{N}\ (0, \sigma^2(\theta, C/N_0). \quad (39)$$

This modeling method for multipath error has been generally adopted for challenging scenarios. For instance, where high position accuracy is required, satellite elevation models have been implemented successfully (Wang et al. 1998). The model proposes the following expression for multipath error covariance

$$\sigma_\epsilon^2 = a + b\ x\ 10^{\frac{-C/N_0(k)}{10}}, \quad (40)$$

where a and b are model parameters and are set based on the multipath environments and equipment. This model is also often called sigma-ϵ (Hartinger and Brunner 1999; Wieser and Brunner 2000), and assumes that measurements with C/N_0 have higher precision and are more effective in mitigation of stochastic errors due to multipath. Alternative models denoted as additive and multiplicative have been proposed, and are denoted as (Medina et al. 2018)

$$\sigma^2 = a + \frac{b}{\sin\theta} + c\ x\ 10^{\frac{-C/N_0(k)}{10}} \quad (41)$$

and

$$\sigma^2 = a + b^{\frac{10^{-C/N_0\ /\ 10}}{\sin\theta}}. \quad (42)$$

Finding the unknown parameters a, b and c of these models is a nonlinear regression problem. For purposes of estimation of C/N_0 within the simulation environment proposed, the parameters used were $a = 10$ m^2 and $b = 150^2$ m^2 Hz (Kuusniemi et al. 2007). Thereafter, a final solution for the pseudo-range error due to multipath effects, ϵ, is proposed based on a normal Gaussian distribution with mean zero and variance that is dictated by modification of the sigma- ϵ model, which is dependent on the elevation angle and the carrier-to-noise ratio of each satellite.

5.4.3.3 Shadowing Effects

Within urban scenarios, direct access to every satellite is not always guaranteed due to the presence of objects that can obstruct communications. Provided a set of possible visible satellites in each location and the ephemeris data, a LOS check can be performed between each satellite and the aircraft's position considering plane intersection with the world geometry as presented in Figure 77. For this purpose, a ray tracing algorithm determines the number of satellites not obstructed by buildings at any point in space over the map, allowing one to re-select the set of satellites that can be used for the calculation of the DOP parameters, along with the new geometry used for trilateration.

Furthermore, the ray tracing algorithm determines the obstacles in the LOS between satellite-UA links. With this, it establishes the carrier-to-noise ratio model for multipath definition and posterior quantification of the added errors into the pseudo-ranges (and, consequently, its influence over DOP).

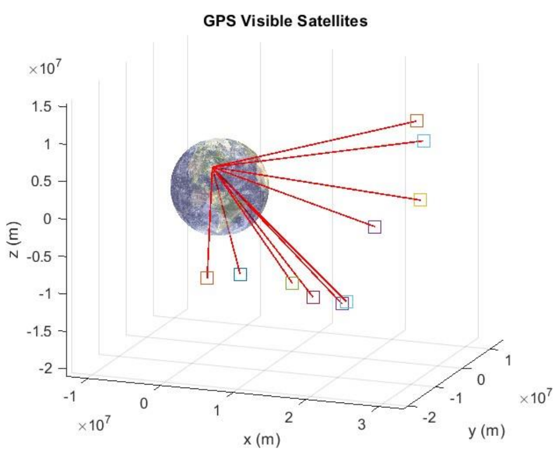

(a) Global Visible Satellites Check Geometry

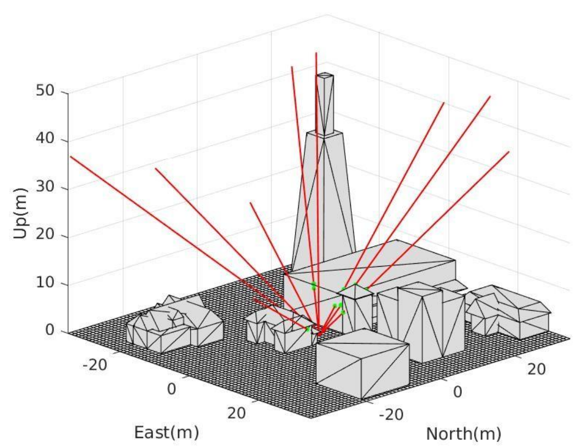

(b) Line-of-sight Plane Intersection Check within the World

Figure 77. Line-of-sight check for shadowed satellites.

5.4.3.4 Dilution of Precision

Degraded satellite coverage is usually defined in terms of the magnitude of the DOP parameter. This parameter is used as a metric of the quality of receiver-satellite geometry (Bossler et al. 2010) or of the magnifying effect on GPS position error induced by mapping pseudo-range accuracy (i.e., "User Range Error") into a position solution within the specified coordinate system, through relative satellite-to-receiver geometry (GPS SPS PS Standard 2020). The DOP varies as a function of satellite positions relative to user positions. Four DOP metrics exist:

- Position Dilution of Precision (PDOP) – spatial, three dimensions (3-D)
- Horizontal Dilution of Precision – spatial, two dimensions (2-D)
- Vertical Dilution of Precision – spatial, one dimension (1-D)
- Time Dilution of Precision – temporal, one dimension (1-D)

This research focuses on the PDOP availability standard which is defined as the percentage of time over any 24-hour interval that the PDOP value is less than or equal to its threshold for any point within the service volume. The PDOP describes the error caused by the relative position of the GPS satellites and each particular satellite-to-user geometry, which has its own set of PDOP values. The higher the DOP value, the poorer the satellite geometry is with respect to the user on the ground. For example, Figure 78(b) shows visible satellites that are close together, hence the geometry is said to be weak and the DOP value is high; while in Figure 78(a) the geometry is strong and the DOP value is low.

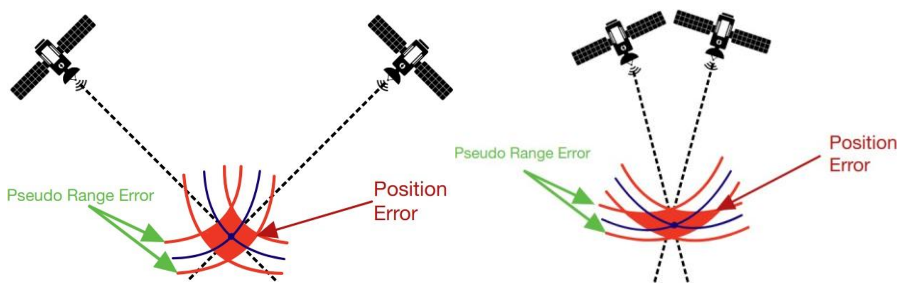

(a) Good Satellite Geometry (b) Bad Satellite Geometry

Figure 78. Area of uncertainty due to satellite geometry configuration.

Other factors that can increase the effective DOP value include obstructions such as nearby mountains or buildings. This occurs because of multipath effects, which occurs when GPS satellite signals bounce. In effect, the GPS receiver detects the same signal twice at different ranges, as shown in Figure 62.

Satellite availability is required for determining adequate accuracy. A nominal constellation of 24 GPS satellites, located in six orbital planes, is sufficient to ensure that there will be at least four satellites visible, at any unobstructed site on the Earth, at any time of the day (Bossler et al. 2010). When multiple satellites are available, different approaches can be used to assess DOP [e.g., fast satellite selection (Jyothirmaye et al. 2019) when all satellites are in view, optimum four satellite configuration (Dutt et al. 2009), among others]. In urban environments, the number of satellites becomes a variable parameter that changes constantly based on the number of satellites obstructed. This results in a variable DOP along the trajectory. The geometric DOP is defined as the square root of variances of receiver position over an orthogonal coordinate frame, for example North-East-Down, and can be expressed as

$$\sigma_G = \sqrt{\sigma_E + \sigma_N + \sigma_U + \sigma_{dt}} = \sigma tr(A^T A)^{-1}. \tag{43}$$

The matrix A is denoted as the design matrix, which contains the variances in the position estimation over each axis and cross terms. This matrix is calculated based on the locations of the satellites and the receiver position over the Cartesian frame as

$$A = \begin{bmatrix} \frac{x_r - x_{s1}}{\rho_1} & \frac{y_r - y_{s1}}{\rho_1} & \frac{z_r - z_{s1}}{\rho_1} & 1 \\ \frac{x_r - x_{s1}}{\rho_1} & \frac{y_r - y_{s1}}{\rho_1} & \frac{z_r - z_{s1}}{\rho_1} & 1 \\ . & . & . & . \\ \frac{x_r - x_{s1}}{\rho_1} & \frac{y_r - y_{s1}}{\rho_1} & \frac{z_r - z_{s1}}{\rho_1} & 1 \end{bmatrix}, \tag{44}$$

where x_r, y_r, z_r and $x_{s1..n}$, $y_{s1..n}$, $z_{s1..n}$ are receiver and satellite positions defined over the selected frame, and ρ are the respective pseudo-ranges from satellite to receiver (Jyothirmaye et al. 2019). Once a design matrix is calculated, the co-factor matrix that provides the variances is defined as

$$Q = (A^T A)^{-1} = \begin{bmatrix} \sigma_x^2 & \sigma_{xy} & \sigma_{xz} & \sigma_{xt} \\ \sigma_{yx} & \sigma_y^2 & \sigma_{yz} & \sigma_{yt} \\ \sigma_{zx} & \sigma_{zy} & \sigma_z^2 & \sigma_{zt} \\ \sigma_{tx} & \sigma_{ty} & \sigma_{tz} & \sigma_t^2 \end{bmatrix}. \tag{45}$$

These parameters can be used in the estimation of geometry, position, and time DOP in order to assess the overall performance of the GPS. Therefore, these coefficients provide useful information regarding the position estimation performance in autonomous flights over urban canyons based on the satellites available at every time interval.

Simultaneously, urban structures are likely to cause multipath effects by reflecting signals inside the urban canyons. As previously mentioned, multipath is a common problem where the error is caused by reflected signals entering the radio-frequency front-end of the receiver (MacGougan et al. 2001). The superposition of the direct signal and reflected signals can either cancel or add an effective multipath, distorting the correlation function used to synchronize incoming signals and adding errors in range measurement. Over moving platforms such as UA operating within urban environments, this problem can be significant and variant in time, due to the diversity of relative obstacles associated with constant changes of geometry.

Finally, UAS mission performance under errors caused by blocking and multipath effects can be dangerous and expensive. Therefore, the simulation tools combined with GPS models presented in this report provide useful information for predictive and preventive planning for urban environment missions.

The simulation environment described in Section 5.2.1 was used to generate a geometric representation based on polygonal shapes and was developed based on the virtual map as presented in Figure 79. The simulation is used for the application of ray-tracing algorithms with projected signal LOS. Plane intersection methods are used over the polygonal shapes to determine the satellites within potential LOS that are obstructed by buildings in the environment.

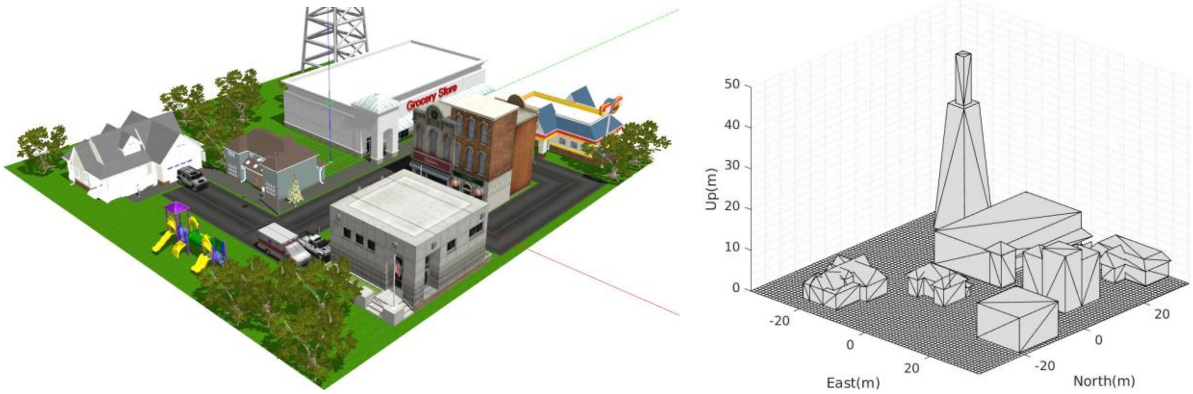

(a) 3D Virtual Environment (b) 3D Polygonal Environment Representation

Figure 79. Simulation environment world.

Evaluation of the visible satellites is performed at every time step of a mission simulation within the World map by using the Ephemeris model and the proposed signal shadowing algorithm. Given initial conditions for the Ephemeris model, it is possible to calculate the visible satellites over the whole map at a given Epoch as shown in Figure 80 being the availability represented as a heat map with the number of directly visible satellites.

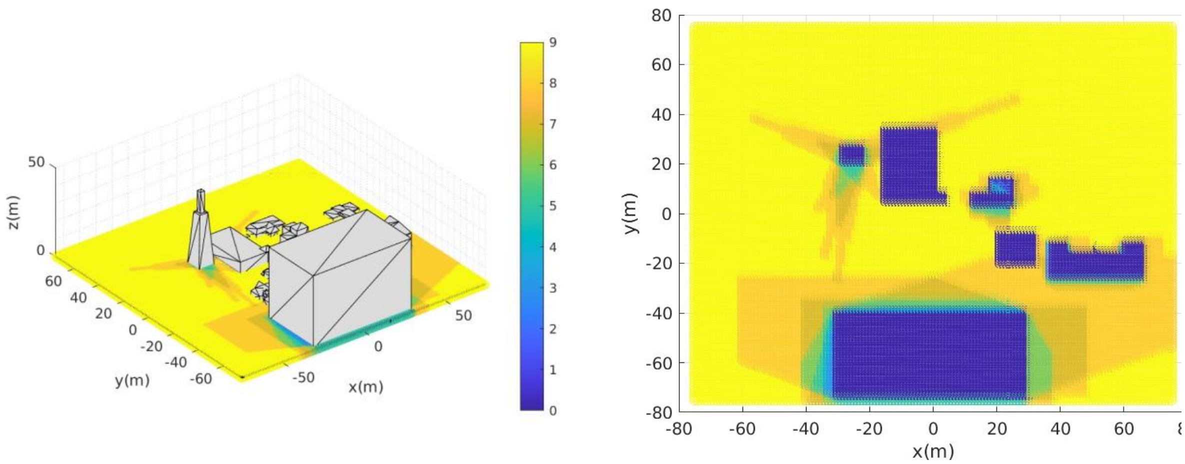

(a) 2D Heatmap visible Satellites (b) 3D Heatmap visible Satellites

Figure 80. Heat map of available satellites within a defined Epoch at 8 m altitude.

Finally, by applying such variance of directly visible satellites from the aircraft's reference frame, a reconfiguration of the optimal satellite geometry is applied for the DOP calculation, resulting in a nonlinear position error covariance of the GPS localization. It is expected that the PDOP value will be severely affected by the change of visible satellites, which can be critical in autonomous missions that require a low constant DOP for safe execution. This covariance of the position uncertainty is therefore reflected in the measurement provided to the navigation system that uses this position information within a loosely coupled INS with GPS.

5.5 Aircraft Navigation Assessment

This section describes multiple scenarios to assess the impact of GPS signal degradation by implementing the proposed GPS model with shadowing and multipath effects. Since multiple noise models provided in this work are based on stochastic approaches, every mission proposed was performed 20 times to provide a probability of collision under the defined GPS and mission conditions. Moreover, it is desired to evaluate the positioning performance under shadowed conditions with and without multipath effects.

5.5.1 Shadowing with no Multipath

The first scenario corresponds to a close UA fly-by to an area previously identified with signal obstructions due to the presence of buildings. The mission provides a set of waypoints that the UA must follow over a period of time. The flight starts at coordinates {0 m, 0 m, 0 m} within the local frame and ends at {30 m, -36 m, 8 m}. This mission is a representative case of package delivery missions.

The PDOP was evaluated along with all the satellites available during the duration of the mission as presented in Figure 81. Due to the close proximity to the highest building, the number of available satellites is reduced to half, showing a direct impact in the PDOP value, and consequently the positioning covariance of the UA. The planar covariance increases drastically with the change of satellites as shown in Figure 82 since this value is directly correlated with the position of the available satellites given (31). Additionally, it is possible to observe that there exists a correlation between the increment of the covariance compared to the number of satellites available as depicted in Figure 83. It is important to note, however, that the covariance is dependent on the geometry rather than the number of available satellites. Hence, it is still possible to observe low covariance values with a low number of satellites.

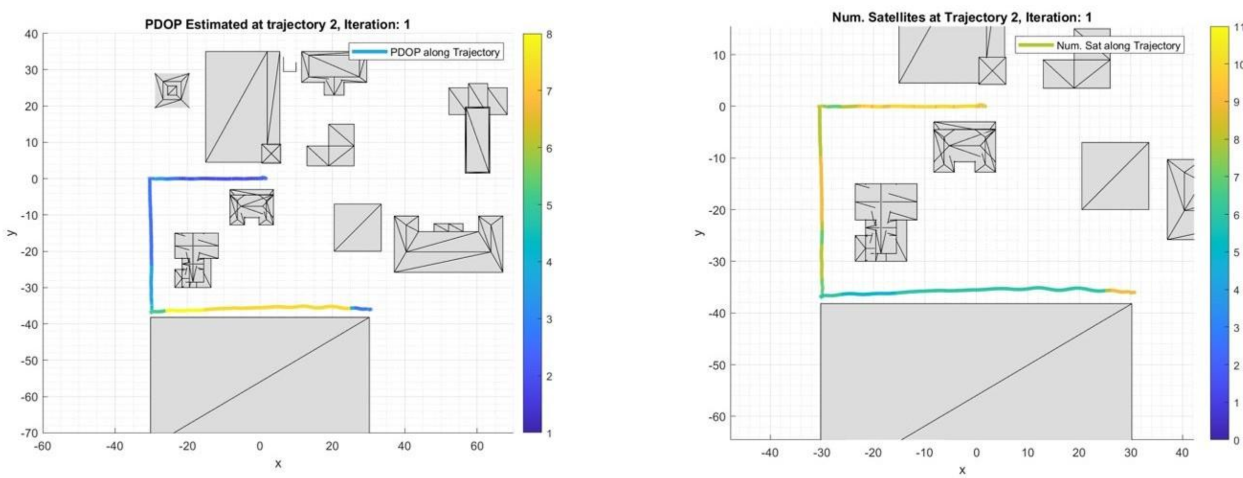

Figure 81. Position Dilution of Precision and number of available satellites. Case 1: Top view of the urban environment.

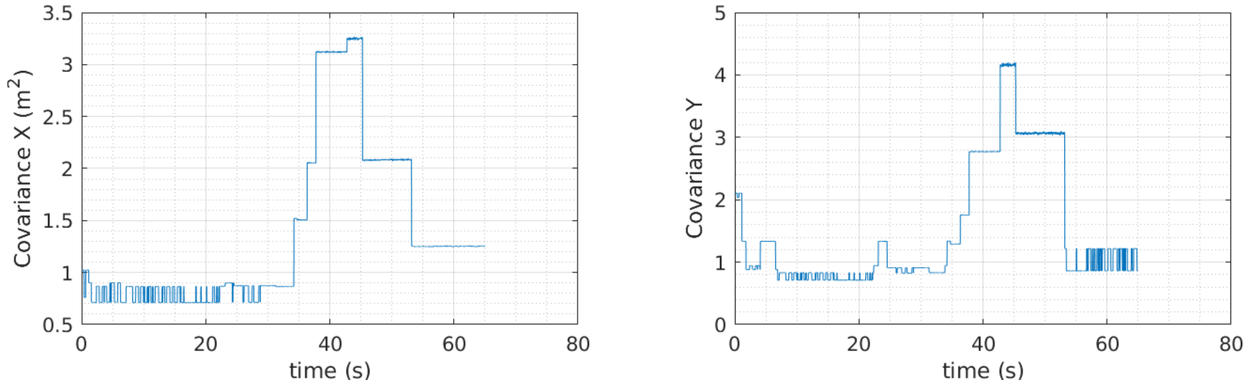

Figure 82. Planar position covariance evolution.

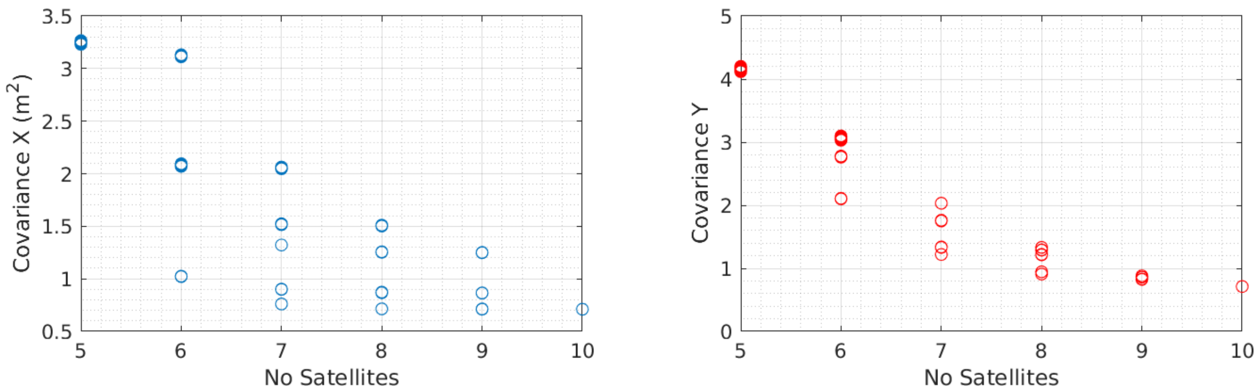

Figure 83. Planar covariance against number of visible satellites.

A collision rate *CR* can be calculated as the number of simulations with collisions over the total number of simulations

$$CR = \frac{\#Collisions}{\#Totalsimulation} 100\%. \tag{46}$$

In this case, the collision rate observed when the UA approaches the building from a 2 m distance with shadowing conditions is 20%, i.e., 4 cases with collisions over 20 runs of the same mission under the defined mission parameters.

5.5.2 Shadowing with Multipath

The multipath effects have a direct correlation with the carrier-to-noise ratio measured by the receiver. This parameter is highly affected by the presence of buildings in the surroundings and narrow elevation angles. As suggested in (Kuusniemi et al. 2007; Deep et al. 2018), there exists a degradation of the carrier-to-noise ratio within urban environments and near challenging obstacles. Therefore, two models for the carrier-to-noise ratio are proposed for simulation purposes as presented in Figure 84, where the model presented for C/N_0 in an urban environment is used at proximity to buildings in order to enhance the noise propagated by multipath effects.

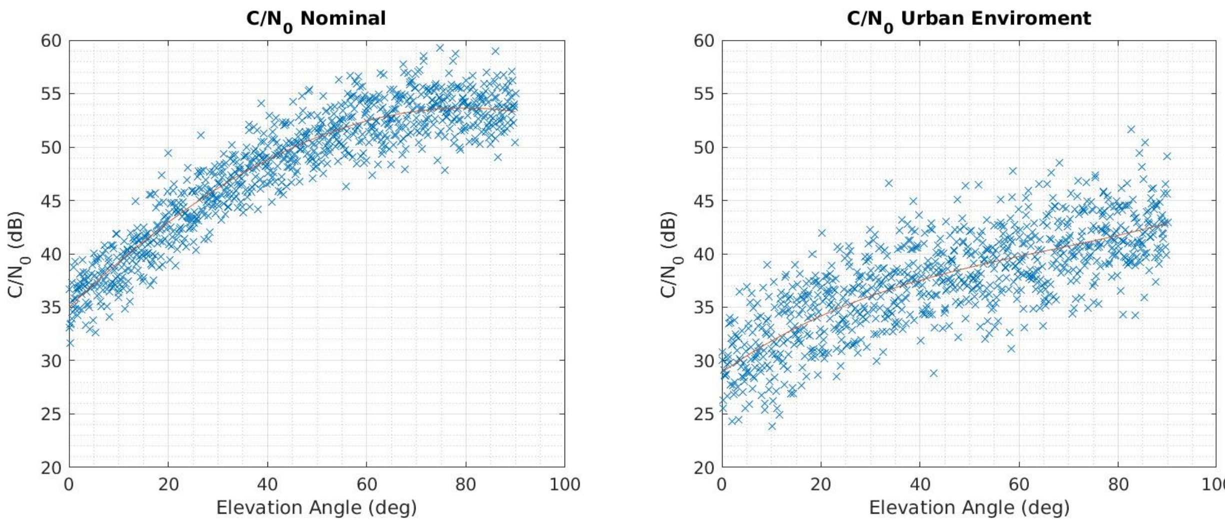

Figure 84. C/N_0 measurement models for multipath characterization.

The second scenario corresponds to a close UA fly-by to an area previously identified with signal obstructions due to the presence of buildings. This case considers the addition of multipath error in the pseudo-range measurement presented in (17) and (18), following the model presented in (26), with variance calculated using (27). Once the aircraft is within close proximity of buildings, the simulation environment changes from the nominal C/N_0 model to the urban environment model presented in Figure 85, in order to recreate the effects of multipath due to building reflections. Similar to Case 1, the mission provides a set of waypoints that the UA follows over a period of time.

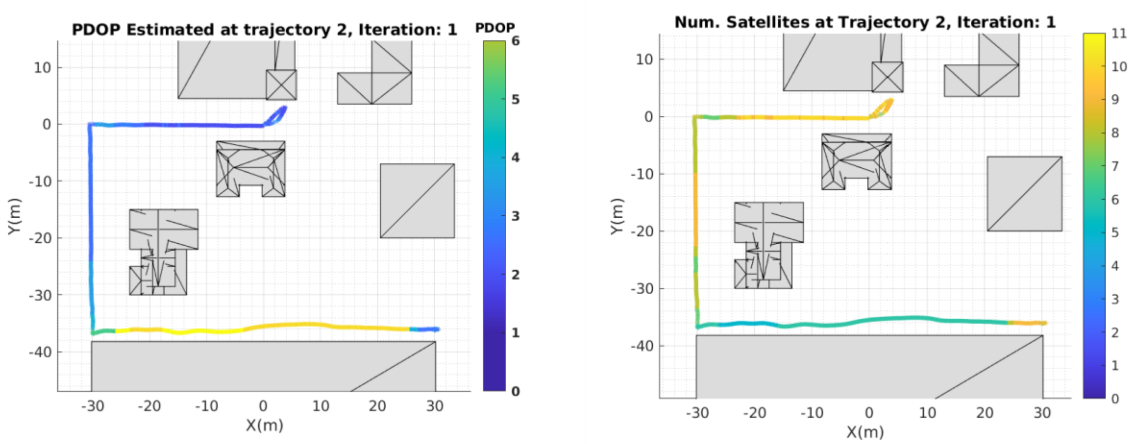

Figure 85. Position Dilution of Precision and number of available satellites. Case 2: Top view of the urban environment.

The covariance in the position estimation error, for the case of multipath effects presented in Figure 86, was observed to be mainly driven by the geometry problem rather than the multipath pseudo-range error. Given the parameters b and a in (26), the order of magnitude of the parameter ϵ oscillates between 5 m and 50 m, which is small compared to the order of magnitude of the geometric range of the UA and the satellites. As a result, it was found that a good geometry of locked satellites can compensate for inclusion of errors due to the multipath effect; therefore, covariance changes are mainly driven by changes in the trilateration due to geometry adjustment from satellite variations. In contrast, for cases observed in Figure 87 for four satellites, the notable variation of the position covariance error can be explained due to a combination of multipath errors over a poor geometry configuration of available satellites.

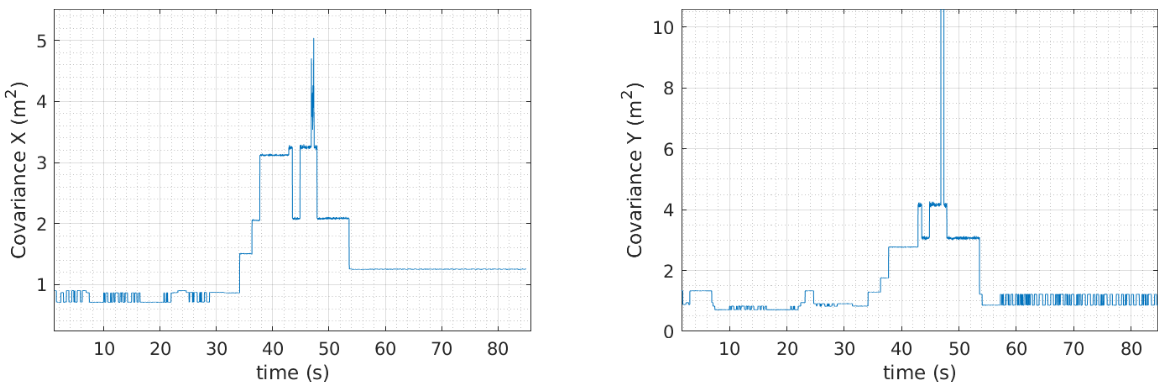

Figure 86. Planar position covariance evolution.

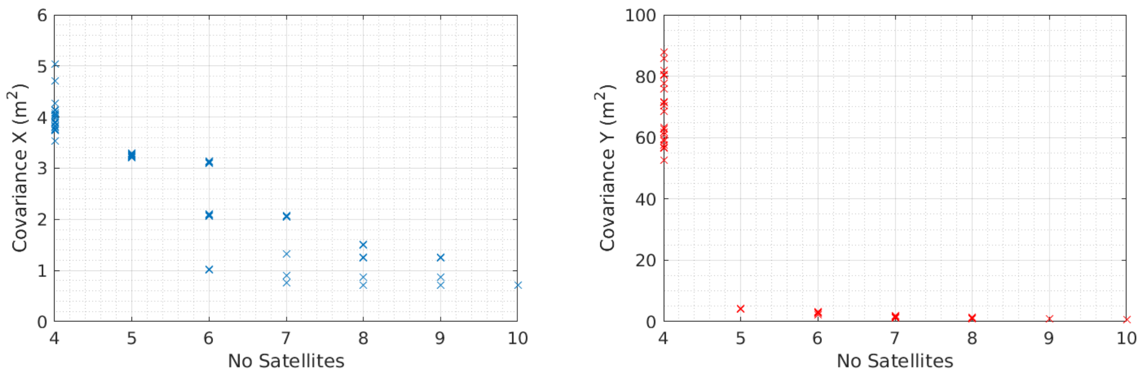

Figure 87. Planar covariance against number of visible satellites.

From the observed magnitude of the multipath error ϵ over the pseudo-range measurement, it is suggested that the correlation and direct influence of multipath error over the position covariance is not significant in the presence of good satellite geometry. Notwithstanding, multipath has a considerable effect with poor satellite geometry, which can often be the case for urban environments with tall buildings. The collision rate observed by approaching the UA to within 2 m of the building with shadowing conditions and multipath effects increased to 55% given 11 cases with collisions over 20 runs of the same mission.

5.5.3 Effects of Flying Between Buildings

The effects of flying UA close to buildings and other structures in urban areas were also studied and analyzed in accordance with GPS signal degradation. In this scenario, the quadcopter in the simulation environment is flown at different distances from the wall of a building and at different altitudes. Multiple Monte Carlo simulations were performed for each case as the satellite geometry changes every iteration. From these data, the collision rate is calculated based on the total number of cases and the number of cases that led to a collision as shown in (46). The trend observed is that the quadcopter can fly closer to the building as the altitude of the quadcopter increases. This is evaluated and results are summarized in Table 26.

Table 26. Collision rate.

		Height from Ground					
Distance from building wall		8 m	12 m	16 m	20 m	24 m	28 m
	2 m	100%	87.5%	87.5%	80%	80%	75%
	4 m	62.5%	30%	20%	15%	10%	10%
	6 m	26.7%	6.7%	5%	0%	0%	0%
	8 m	0%	0%	0%	0%	0%	0%
	10 m	0%	0%	0%	0%	0%	0%

Based on the risk of collision, a 3D representation around the building was created to show the areas in which the quadcopter is most likely to crash. As shown in the Figure 88, the red area represents a no-fly zone for the quadcopter while the green area represents a safe flying zone.

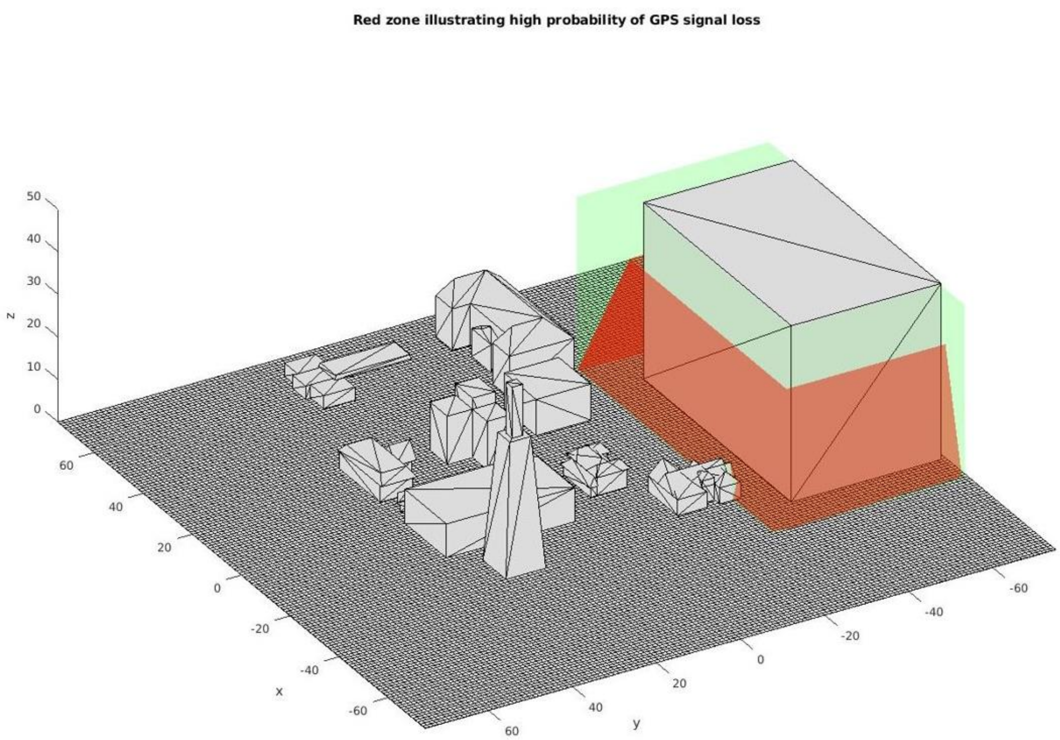

Figure 88. No-fly zone for quadcopter.

Further analysis was performed by flying the aircraft between two tall buildings to observe trajectory following accuracy. For this scenario, the simulation environment and configurations of buildings was modified as shown in Figure 89.

Figure 89. Modified map with two tall buildings.

In this scenario, the aircraft flies exactly between the two buildings that are 28 m apart at altitudes of 2 m and 4 m. The trajectories followed by the quadcopter are shown in Figures 90 and 91.

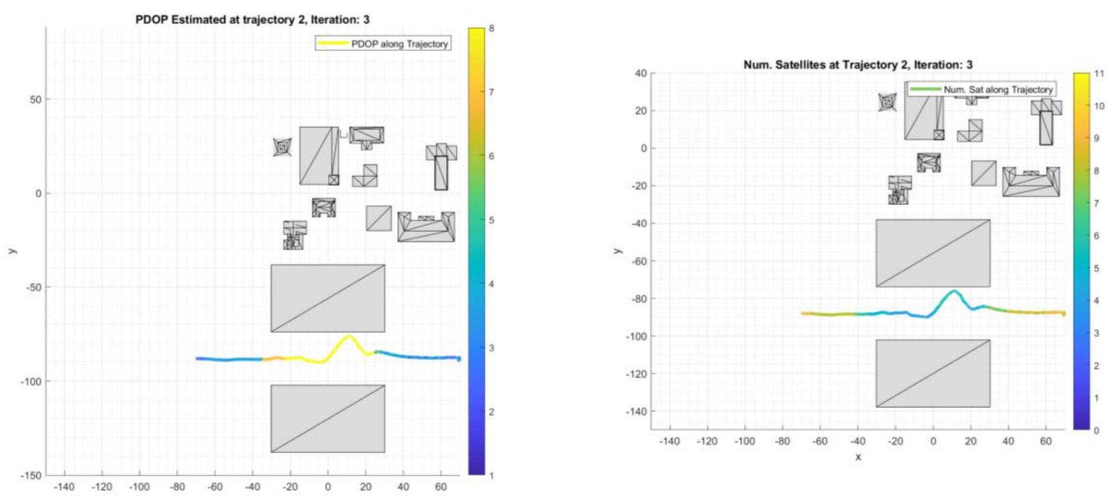

Figure 90. Quadcopter flying at 2 m height.

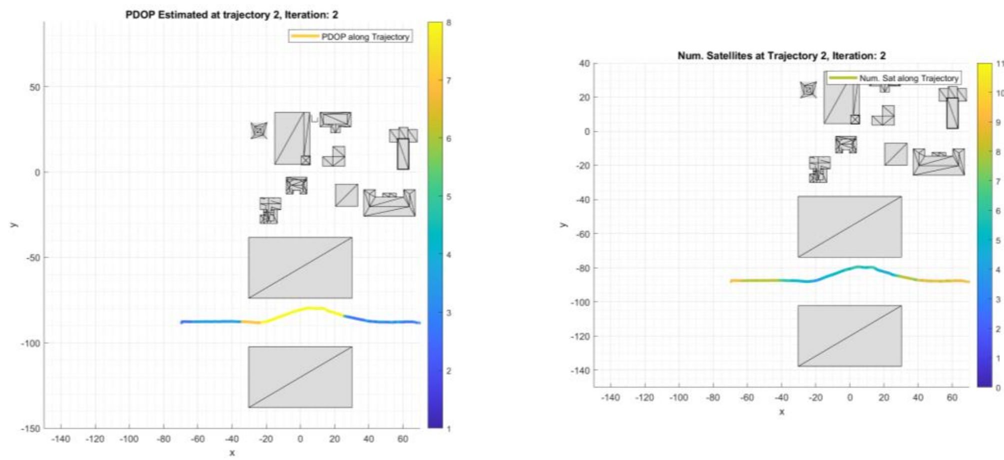

Figure 91. Quadcopter flying at 4 m height.

Based on these results, it is evident that the aircraft's flight performance when flying between buildings improves at higher altitudes. This improvement can be attributed to the increased visibility of satellites and reduced signal obstruction experienced at elevated altitudes. In essence, flying between buildings and at greater heights leads to a noticeable increase in the aircraft's flight capabilities.

5.5.4 Risk Assessment under GPS-Degradation

To complement results presented in Section 5.2.2, a risk assessment is provided considering the UAS operating under GPS-degraded scenarios. These include the risk of flying between buildings when shadowing and multipath effects are present. The rate of fatality *C* was then calculated as combinations of vertical and horizontal separation with respect to the buildings. The parameters for the selected runs are shown in Table 27 following the same quadrotor dynamics, characteristics, and environmental configuration. Using these data, the estimated risk assessment parameters were calculated as shown in Table 27.

Table 27. Simulation parameters for an example of each test case. In the Parameter row, H is height above ground and V is distance from building wall.

Parameter	H=2m, V=8m	H=6m, V=16m	H=28m, V=10m
$\bar{A}_{lethal}$ m^2	552.43	174.34	84.34
P_{fail}	$1x10^{-3}$	$1x10^{-3}$	$1x10^{-3}$
ρ_{people} pp km^{-2}	900.0	900.0	900.0
S	0.195	0.195	0.195
$P_{collide}$	1.0	1.0	1.0
$P_{fatality}$	0.6	0.5	0.22
C (fatalities (flight hr)$^{-1}$)	$5.81x10^{-5}$	$1.52\text{x}10^{-5}$	$0.32\text{x}10^{-5}$

These calculated rates of fatality are consistent with the results presented in Table 25 for nominal and abnormal GPS conditions, such as dropouts or jamming cases. GPS-degradation in the form of shadowing and multipath has a significant effect on the performance of the UAS following a specific path between buildings. As the vertical and horizontal separation of the UAS with respect to the buildings increase, the risk of collision and the rate of fatality decreases.

6 CONCLUSIONS

6.1 Linear Infrastructure—Powerlines

6.1.1 Electromagnetic Fields

6.1.1.1 Single Powerlines

Herein, electric fields generated by EHV transmission lines were estimated for 345, 500, and 765 kV transmission lines. Results were verified using analytical methods.

Minimum estimated safe horizontal and vertical distances are provided. Two approaches can be applied to integrate these distances into safe operating practices. One assumes a level of local awareness and expertise that a UAS flight crew might be expected to have if working directly with a power authority around the transmission lines in question. These distances would be integrated into pre-flight planning for an operation given the normal information required to conduct a safe flight, including ambient weather and forecasts. The other involves abstraction of these results into conservative assumptions and minimum safe distances suitable for an operator, such as a contractor less familiar with the EM fields and field effects in question. Overall, minimum safe distances should likely be calculated as a single, conservative value for a given operation and a given transmission line's characteristics.

6.1.1.2 Parallel Transmission Lines

Numerical simulations were used to analyze the distribution of magnetic fields generated by parallel EHV transmission lines without considering the effect of ground or shield wires. The magnetic field profiles of the 345, 500, and 765 kV transmission lines were analyzed from the perspective of UAS exposure. The details of where the two fields cancel out or reinforce each other were investigated; however, the results of the examined magnetic field profiles for parallel transmission depend upon knowing the relative phase of each of the conductors and loads in the line. The next step in this research will be to apply the proposed model to multi-parallel transmission lines and to compute electric fields, as well as apply it to other high-voltage transmission lines while considering the effects of shields, ground wires, catenaries, and when the ground surface under the transmission lines is irregular.

6.1.1.3 Short-Circuiting Powerlines

A phase-to-phase short circuit results in magnetic fields that are much higher than corresponding nominal transmission line magnetic fields. This results in safe distances that are much larger than they would be if the transmission line were performing nominally.

Because the safe distance is much larger, special care should be taken in the case of short circuit during operations where this type of issue may arise. Normal guidance suggestions indicate that safe distance values might be abstracted into a single conservative value for UAS operators not familiar with the exact specifics of the EM effects; however, the short-circuit situation should be treated and calculated more carefully to provide a balance between the needs of the operation and the larger safe distances. Some of the recommended safe distance values could still be combined into fewer conservative assumptions; however, these adjustments should be made through further careful analysis.

6.1.1.4 Transformers

Two standard distribution transformer configurations were modeled in 3D software. Results were analyzed to define the minimum safe distance boundaries for a UAS to operate around the two transformer configurations. The single-phase transformer had horizontal and vertical safe distances of 2.1 m and 1.5 m, respectively. For three-phase transformers, these distances approximately doubled to 4.1 m (horizontal) and 3.7 m (vertical).

In these cases, transformer effects provide clear guidance for maintaining a safe distance from transformers of this size and performance level. Safe distances may exceed these depending upon the circumstances; however, this should be carefully considered during pre-flight planning or when creating standard operating procedures. Transformers operating at higher performance levels should be evaluated to develop more comprehensive distance values. Likewise, groups of transformers may have to be evaluated for overlapping EM fields, such as at a power substation.

6.1.2 Airflow

6.1.2.1 Wind Effects

A multicopter's ability to maintain course or at least resist further displacement after the initial onset of wind effects is predictable and enables provision of guidelines on minimum distances from hazardous areas where EM effects may further disrupt safe navigation. A minimum distance must be maintained from the unsafe zone surrounding high voltage powerlines for a given crosswind component. There is also a maximum wind component that will exceed the aircraft's performance envelope, resulting in a no-fly decision by the air crew as the ambient conditions exceed the UAS's ability to navigate the area.

A multicopter's type, like other copters, is subject to a reduction in performance envelope given strong headwinds; therefore, a strong quartering headwind or tailwind, or even a strong descending wind, will make it harder for the aircraft to maintain course and distance from unsafe EM distances. This information should be used as part of the pre-flight decision process before launching an inspection mission.

The specific capacity to navigate a mission route will depend upon the aircraft's performance rather than a universal distance. Higher performance will result in the aircraft being able to maintain a closer distance to the unsafe EM area.

6.1.2.2 Wake Vortex Effects

To better understand the effects of a broad cross-section of wake turbulence effects on UAS, wake models were applied in close proximity to power transmission lines when interacting with crewed aircraft—specifically 747, 737, Cessna 172, Thrush 510G, Air Tractor AT502B, and mid-sized helicopter models in forward motion. Wake encounters were constructed to ensure that the UAS flew through aircraft wakes near the center of the rotation shortly after that aircraft's passage. The simulations were executed twice, one with the wake-generating aircraft opposed and roughly head-on to the UAS and then 90° to the UAS.

The results were plausible when compared to previous research and accounting for the difference in fixed-wing performance vs. multirotor performance: as the wake-generating aircraft became smaller, the wake effects on altitude and attitude displacement ranged from major for the 747 to nearly negligible for the 172. The rest of the aircraft wake effects from crewed aircraft sizes of the type expected to be encountered a) at common UAS altitudes and b) in shielded spaces remained easily recoverable to negligible.

The implication for safety-of-flight issues is that there remains a small residual risk of displacement or upset that pushes the aircraft into proximity of transmission lines. Otherwise, the simulations do not currently show elevated risk compared to the risks already inherent in UAS/crewed traffic encounters. The remaining exception would be the effects of helicopter rotor wash pushing down on a UA. This, too, presents a scenario where failures of separation have already occurred. UAS aircraft could certainly be pushed down by sustained rotor wash into a transmission line. The safety failure, however, is that of separation; the UAS aircraft should never have come to be beneath the CA. This prospect, coupled with the other wake turbulence results, points toward planning and effective traffic separation.

The overall need, in this case, is for traffic location and intention awareness. When in a potentially hazardous environment such as power lines, the flight planning and timing of a given mission should be made available to other traffic that may be in the area. For powerline related activities, it can be assumed that the power authority in charge of the transmission lines would be responsible for planning missions to account for this, even in a theoretical case where two different entities, such as contractors, may be at work on the lines. Otherwise, normal guidance on sensor and DAA system equipage should be followed.

Other unusual scenarios exist. One example is the possibility of large aircraft passage like a transport category airplane crossing well above the UAS's path posing a risk, but it is assumed that this is restricted to locations below approach/departure paths near airports. In those scenarios, prudent planning and alternate means of inspection remain likely the best mitigation.

One final future case might be a scenario where many UAS have been granted passage through a power corridor for transport purposes. In this case, a comprehensive rules structure for reserving and blocking off airspace on a timed basis may be the best approach.

6.2 Impacts on GPS Systems

The Global Positioning System is the most widely used technology for positioning applications, thanks to its remarkable accuracy and widespread availability. Nevertheless, due to the inherent properties of the physical phenomena underlying GPS functionality, satellite signals are susceptible to reflections and diffraction, much like any other electromagnetic wave. The manifestation of these effects, commonly referred to as scintillation, multipath interference, and shadowing, can frequently undermine the precision of GPS positioning, ultimately resulting in either a partial or complete loss of signal tracking. Such occurrences can lead to a decline in navigation performance and in the integrity of aerospace systems.

In this task, the research team delved into the quantitative characterization of these effects and their implications for position accuracy across various urban environments. The impact of signal degradation effects was analyzed by evaluating GPS constellation quality metrics such as the DOP. Different models were developed to integrate and evaluate the effects of signal blockage and multipath effects over defined missions. A high-fidelity simulation environment was developed for operation of sUAS across a range of typical and relevant scenarios. Different modules of the simulation and their interaction were described and specific scenarios relevant to these operations were used to perform a preliminary risk assessment associated with these operations.

Autonomous missions designed with high levels of navigation accuracy require low levels of uncertainty, which translates into low DOP values. This becomes achievable when healthy geometries are obtained for the trilateration process and, consequently, a connection with more than seven satellites is commonly needed to obtain enough redundancy to keep DOP low. It is important to note that the geometry of the available satellites is the key factor that influences the DOP. Analysis of multipath effects can be very complex since this becomes a geometric problem applied to antennas in motion given the complex dynamic behavior of sUAS within urban environments. In this task, this limitation was addressed by implementing a stochastic approach to model multipath effects. Numerical simulations revealed that among the various GPS signal degradation types, those posing the highest risks, in descending order, were dropouts, jamming, and a reduced number of satellites (down to four). Thus, GPS integrity should be monitored and addressed for operations where these effects may be realized. This is especially true for operations at low altitudes (≤ 16 m) and close to buildings (e.g., within 6 m). It is noted that impacts associated with altitudes and distances from buildings identified herein have some dependency upon the specific scenarios considered and, thus, a broader analysis to generalize impacts would be valuable.

6.3 Future Work

Future work areas include:

1. For parallel transmission lines, evaluate fields for multi-parallel transmission lines, compute electric fields, and apply the developed model to other high-voltage transmission lines while considering the effects of shields, ground wires, catenaries, and when the ground surface under the transmission lines is irregular.
2. Evaluate safe distances for higher-performing transformers than those considered herein and for groups of transformers.
3. Evaluate of wind and wake vortices on fixed-wing UAS.
4. Generalization of GPS degradation results to provide “rules-of-thumb” for sUAS operations—especially in urban environments.

Bibliography

ABB, 2022: Single phase overhead distribution transformers. Accessed 27 December 2022, https://library.e.abb.com/public/93ad382cf05fe807c1257b130057eeb6/1LCA000003-LTESinglePh overhead 10kVA 167kVA.pdf.

Aerofly Hobbies, 2023: Specifications T-Motor MT2216-09 1100KV V2 Brushless Motor. Accessed 31 October 2023. http://www.aeroflyhobbies.com/24-t-motor-mt2216-12-800kv-v2-brushless-motor.html.

Air Tractor, 2022: Air Tractor | Demand More. Accessed 27 December 2022, https://airtractor.com/.

Almalki, S. J., and S. Nadarajah, 2014: Modifications of the Weibull distribution: A review. *Reliability Eng. & System Safety*, **124**, 32-55.

Autodesk, 2021: Inventor: Powerful mechanical design software for your most ambitious ideas. Accessed 26 December 2022, https://www.autodesk.com/products/inventor/overview.

Ayad, A. N. E. I., W. Krika, H. Boudjella, A. Horch, and F. Benhamida, 2019: Simulation of the electromagnetic field in the vicinity of the overhead power transmission line. *European J. Elect. Eng.*, **21**(1), 49-53.

Azad, A. K., M. G. Rasul, R. Islam, and I. R. Shishir, 2015. Analysis of wind energy prospect for power generation by three Weibull distribution methods. *Energy Procedia*, **75**, 722-727.

Baker, G. H., W. A. Radasky, and J. L. Gilbert, 2019: Electromagnetic Pulse (EMP) Protection and Resilience Guidelines for Critical Infrastructure and Equipment, Version 2.2. National Cybersecurity and Communications Integration Center, 133 pp., https://www.cisa.gov/sites/default/files/publications/19_0307_CISA_EMP-Protection-Resilience-Guidelines.pdf.

Baran, S., and S. Lerch, 2015: Log-normal distribution based Ensemble Model Output Statistics models for probabilistic wind-speed forecasting. *Quart. J. Royal Meteor. Soc.*, **141**, 2289-2299.

Bell Flight, 2022: Bell Products. Accessed 27 December 2022. https://www.bellflight.com/products.

Benarbia, T., and K. Kyamakya, 2022: A literature review of drone-based package delivery logistics. *Sustainability*, **14**, 15 pp.

Bossler, J. D., J. B. Campbell, R. B. McMaster, and C. Rizos, 2010: *Manual of Geospatial Science and Technology*. 854 pp.

Breunig, J., J. Forman, S. Sayed, L. Audenaerd, A. Branch, and M. Hadjimichael, 2019: Modeling risk-based approach for small unmanned aircraft systems. *AUVSI XPONENTIAL 2019: All Things Unmanned*, 1–23.

Brown, J., 2013: Great Northern Transmission Line Project – EMF and Corona Effects Calculations. Power Engineers, 9 pp., https://mn.gov/eera/web/projectfile?legacyPath=/opt/documents/33847/Volume%20II%20Appendix%20I%20Applicants%20Audible%20Noise%20and%20EMF%20Calculations.pdf.

Bruggemann, T., J. Ford, and R. Walker, 2011: Control of aircraft for inspection of linear infrastructure. *IEEE Trans. Control Systems Tech.*, **19**(6), 1397-1409.

Bühringer, M., J. Berchtold, M. Büchel, C. Dold, M. Bütikofer, M. Feuerstein, W. Fischer, C. Bermes, and R. Siegwart, 2010: Inspection of high voltage power lines-A new approach. *Mobile Robotics: Solutions and Challenges*, 455-462.

Chen, D.-Q., X.-H. Guo, P. Huang, and F.-H. Li, 2020: Safety distance analysis of 500 kV transmission line tower UAV patrol inspection. *IEEE Letters in Elect. and Compatible Practices and Appl.*, **2**, 124–128.

COMSOL, 2023: COMSOL Multiphysics. Accessed 31 October 2023. https://www.comsol.com/.

Deep, S., S. Raghavendra, and B. Bharath, 2018: GPS SNR prediction in urban environment. *The Egyptian J. of Remote Sensing and Space Sci.*, **21**(1), 83–85.

DhanaLakshmi, P., L. Kalaivani, and P. Subburaj, 2011: Analysis of magnetic field distribution in power system using finite element method. *2011 Int. Conf. on Comp., Comm. and Electrical Tech. (ICCCET)*, 394-399.

Dutt, V. S. I., G. S. B. Rao, S. S. Rani, S. R. Babu, R. Goswami, and C. U. Kumari, 2009: Investigation of GDOP for precise user position computation with all satellites in view and optimum four satellite configurations. *J. Ind. Geophys. Union*, **13**(3), 139–148.

El Dein, A. Z., 2013: Prediction of Egyptian 500-kV overhead transmission line's radio interference by using the excitation function. *Int. J. of Emerging Electric Power Systems*, **14**(4), 303-308.

EMWorks, 2022: Electromagnetic and Magnetic Simulation Software. Accessed 27 December 2022, https://www.emworks.com/.

EPA, 2011: Exposure Factors Handbook: 2011 Edition. National Center for Environmental Assessment, EPA/600/R-09/052F, 1436 pp.

FAA, 2012: FAA Aerospace Forecast: Fiscal Years 2013-2033. 130 pp. http://www.bv.transports.gouv.qc.ca/per/0965182/10_2013_2033.pdf.

FAA, 2022: Aircraft Characteristics Database. Accessed 27 December 2022. https://www.faa.gov/airports/engineering/aircraft_char_database.

Fernández, R. A. S., S. Dominguez, and P. Campoy, 2017: L 1 adaptive control for wind gust rejection in quad-rotor UAV wind turbine inspection. *Int. Conf. on Unmanned Aircraft Systems (ICUAS)*, 1840-1849.

Fikry, A., S. C. Lim, and M. Z. A. Ab Kadir, 2022: EMI radiation of power transmission lines in Malaysia. *F1000Research*, **10**, 20 pp.

Finneran, S., B. Krebs, and L. Bensman, 2015: Criteria for pipelines co-existing with electric power lines. The INGAA Foundation, Final Report No. 2015-04, 66 pp., https://ingaa.org/wp-content/uploads/2015/10/24732.pdf.

GPS SPS PS Standard, 2020: Global Positioning System Standard Positioning Service Performance Standard, 5th Ed., Office of the Department of Defense, 196 pp.

Gryning, S. E., R. Floors, A. Peña, E. Batchvarova, and B. Brümmer, 2016: Weibull wind-speed distribution parameters derived from a combination of wind-lidar and tall-mast measurements over land, coastal and marine sites. *Boundary-Layer Meteor.*, **159**, 329-348.

Gu, S., W. Chen, J. He, R. Zeng, and G. Xu, 2008: Movement simulation of three-phase short-circuit arcs on distribution lines based on the coupling of magnetic field and motion. *IEEE Trans. Plasma Sci*, **36** (2), 524-529.

Gutierrez, T., A. Cuenca, N. Coulter, H. Moncayo, and B. Steinfeldt, 2022: Development of a simulation environment for validation and verification of small UAS operations. *AIAA SCITECH 2022 Forum*, p. 0060.

Hallock, J. N., G. C. Greene, J. Tittsworth, P. Strande, and F. Y. Wang, 2015: Use of simple models to determine wake vortex categories for new aircraft. *7th AIAA Atmospheric and Space Env. Conf.*, 11 pp.

Hartinger, H., and F. Brunner, 1999: Variances of GPS phase observations: The SIGMA- model. *GPS Solutions*, **2**(4), 35–43.

Hitachi Energy, 2022: Small distribution transformers up to 315 kva. Accessed 27 December 2022. https://www.hitachienergy.com/us/en/offering/product-and-system/transformers/distribution-transformers/liquid-filled-distribution-transformers/small-distribution-transformers-up-to-315-kva.

Henke, R. J., et al., 2009: Framework for Analyzing Separation Distances Between Transmission Lines in Wyoming. ICF International, 120 pp.

Houicher, S., and R. Djekidel, 2021: Calculation of the magnetic field in the vicinity of the overhead transmission lines. *Int. Conf. Digital Techn. and Apps.*, 1529-1538.

Hurt, H. H. Jr., 1965: *Aerodynamics for Naval Aviators*. Office of the Chief of Naval Operations, Aviation Training Division, NAVAIR 00-80T-00, 434 pp.

Isik, O. K., J. Hong, I. Petrunin, and A. Tsourdos, 2020: Integrity analysis for GPS-based navigation of UAVs in urban environment. *Robotics*, **9**(3), 20 pp.

Jyothirmaye, S., V. S. Srinivas, and B. Ramu, 2019: Fast satellite selection techniques and DOPs for multi-GNSS positioning. *2019 URSI Asia-Pacific Radio Science Conference* (AP-RASC), IEEE, 1–4.

Kan, M., S. Okamoto, and J. H. Lee, 2018: Development of drone capable of autonomous flight using GPS. *Proc. of the Int. MultiConference of Eng. and Computer Sci.*, Vol. 2, 5 pp.

Kaplan, E., and C. Hegarty, 2005: *Understanding GPS Principles and Applications*, 2nd Ed., Book News Inc., Artech House, 680 pp.

Katinas, V., M. Marčiukaitis, G. Gecevičius, and A. Markevičius, 2017: Statistical analysis of wind characteristics based on Weibull methods for estimation of power generation in Lithuania. *Renewable Energy*, **113**, 190-201.

Kim, S.-G., E. Lee, I.-P. Hong, and J.-G. Yook, 2022: Review of intentional electromagnetic interference on UAV sensor modules and experimental study. *Sensors*, **22**, 24 pp.

Kos, T., I. Markezic, and J. Pokrajcic, 2010: Effects of multipath reception on GPS positioning performance. *Proc. ELMAR-2010*, 399–402.

Kubo, N., K. Kobayashi, and R. Furukawa, 2020: GNSS multipath detection using continuous time-series C/N0. *Sensors*, **20**(14), 25 pp.

Kumar, R., E. Koley, A. Yadav, and A. S. Thoke, 2014: Fault classification of phase to phase fault in six phase transmission line using Haar wavelet and ANN. *2014 Int. Conf. Signal Proc. and Integrated Networks (SPIN)*, 5-8.

Kuusniemi, H., A. Wieser, G. Lachapelle, and J. Takala, 2007: User-level reliability monitoring in urban personal satellite-navigation. *IEEE Trans. Aerospace and Electronic Systems*, **43**(4), 1305–1318.

Langley, R. B., 1999: Dilution of precision. *GPS World*, **10**(5) 52–59.

Leonardi, M., and E. G. Piracci, 2018: ADS-B degarbling and jamming mitigation by the use of blind source separation. *AIAA/IEEE 37th Digital Avionics Systems Conference*, https://doi.org/10.1109/DASC.2018.8569598.

Li, Y., W. Zhang, P. Li, Y. Ning, and C. Suo, 2021: A method for autonomous navigation and positioning of UAV based on electric field array detection. *Sensors*, **21**(4), 22 pp.

Lisewski, T., and J. Luszcz, 2014: Magnetic field generated by short circuit current in the 110 kV power system. *2014 Int. Symp. on Electromag. Comp.*, 360-363.

Lunca, E., B. C. Neagu, and S. Vornicu 2021: Finite element analysis of electromagnetic fields emitted by overhead high-voltage power lines. *Numerical Methods for Energy Applications*, N. M. Tabatabaei and N. Bizon, Eds., Springer, 795-821.

Lusk, R. M., and W. H. Monday, 2017: An Early Survey of Best Practices for the Use of Small Unmanned Aerial Systems by the Electric Utility Industry. Oak Ridge National Laboratory, ORNL/TM-2017/93, 168 pp., https://info.ornl.gov/sites/publications/files/Pub73072.pdf.

MacGougan, G., G. Lachapelle, R. Nayak, and A. Wang, 2001: Overview of GNSS signal degradation phenomena. *Proc. of the Int. Symp. Kinematic Systems and Geodesy, Geomatics and Navigation*, 87-100.

Matikainan, L., M. Lehtomäki, E., Ahokas, J. Hyyppä, M. Karjalainen, A. Jaakkola, A. Kukko, and T. Heinonen, 2016: Remote sensing methods for power line corridor surveys. *ISPRS J. of Photogrammetry and Remote Sens.*, **119**, 10-31.

MAVIC PRO, 2017: User Manual. 2017.12, Version 2.0, 64 pp.

MD Helicopters, 2022: MD 500E - MD Helicopters. Accessed 27 December 2022. https://www.mdhelicopters.com/md-500e.html.

Medina, D., K. Gibson, R. Ziebold, and P. Closas, 2018: Determination of pseudorange error models and multipath characterization under signal-degraded scenarios. *ION GNSS*, 11 pp.

Mellinger, D., 2012: Trajectory generation and control for quadrotors, University of Pennsylvania, 137 pp, https://core.ac.uk/download/pdf/76383736.pdf.

National Coordinating Center for Communications, 2019: Electromagnetic Pulse (EMP) Protection and Resilience Guidelines for Critical Infrastructure and Equipment. Version 2.2, Arlington, Virginia, 133 pp., https://www.cisa.gov/sites/default/files/publications/19_0307_CISA_EMP-Protection-Resilience-Guidelines.pdf.

Park, J., S. Kim, J. Lee, J. Ham, and K. Oh, 2020: Method of operating a GIS-based autopilot drone to inspect ultrahigh voltage power lines and its field tests. *J. Field Robotics*, **37**, 345–361.

Patrik, A., G. Utama, A. A. S. Gunawan, A. Chowanda, J. S. Suroso, R. Shofiyanti, and W. Budiharto, 2019: GNSS-based navigation systems of autonomous drone for delivering items. *J. Big Data*, **6**(1), 1–14.

Perrotta, G. M., 2015: Characterization of rotor wake in ground effect. *53rd AIAA Aerospace Sciences Meeting*, p. 0370.

Pishgar-Komleh, S. H., A. Keyhani, and P. Sefeedpari, 2015: Wind speed and power density analysis based on Weibull and Rayleigh distributions (a case study: Firouzkooh county of Iran). *Renewable and Sustainable Energy Reviews*, **42**, 313-322.

Rufa, J. R., and E. M. Atkins, 2016: Unmanned aircraft system navigation in the urban environment: A systems analysis. *J. Aerospace Information Systems*, **13**(4), 143–160, https://doi.org/10.2514/1.I010280.

Qiu, Z. B., J. J. Yan, W. J. Xu, and C. P. Hang, 2018: Hybrid prediction of the breakdown voltages of short air gaps with typical electrodes. *High Volt. Eng.*, **44**, 2012–2018.

Rinne, H., 2008: *The Weibull Distribution: A Handbook*. CRC press, 808 pp.

Schiano, F., J. Alonso-Mora, K. Rudin, P. Beardsley, R. Siegwart, and B. Sicilianok, 2014: Towards estimation and correction of wind effects on a quadrotor UAV. *Int. Micro Air Vehicle Conf. and Comp. 2014*, 134-141.

Seregina, L. S., R. Haas, K. Born, and J. G. Pinto, 2014. Development of a wind gust model to estimate gust speeds and their return periods. *Tellus A: Dynamic Meteor. and Ocean.*, **66**, 15 pp.

Shah, S., D. Dey, C. Lovett, and A. Kapoor, 2018: Airsim: High-fidelity visual and physical simulation for autonomous vehicles. *Field and Service Robotics*, M. Hutter and R. Siegward, Eds., Springer, 621-635.

Shu, Z. R., and M. Jesson, 2021: Estimation of Weibull parameters for wind energy analysis across the UK. *J. Renew. and Sust. Energy*, **13**, 18 pp.

Siemans, 2017: Power Engineering Guide. 8th Ed., 569 pp., https://assets.new.siemens.com/siemens/assets/api/uuid:5bfb815b0db95760272f17c1329cc56c0c402686/peg8-final-160812.pdf.

Skog, I., P. and Händel, 2005: A low-cost GPS aided inertial navigation system for vehicle applications. *13th European Signal Processing Conference*, IEEE, 1–4.

Smyrnaios, M., S. Schn, M. Liso, and S. Jin, 2013: Multipath propagation, characterization and modeling in GNSS. *Geodetic Sciences-Obs., Modeling and Applications*, S. Jin, Ed., IntechOpen, 99–125.

Strümpfel, C., E. Schuster, S. Huschbeck, C. Berth, and M. U. de Haag, 2020: Assured multi-mode navigation for urban operations of small UAS. *AIAA Scitech 2020 Forum*, Vol. 1 Part F, https://doi.org/10.2514/6.2020-1945.

Sugumar, R., T. Bruner, K. Silas, T. Haritos, M. Askelson, H. Cathey, and H. Moncayo, 2021: ASSURE A45_A11L.UAS.87 – Shielded UAS Operations: Detect and Avoid (DAA) – Literature Review. USDOT FAA (ASSURE), 76 pp.

Sukkiramathi, K., and C. V. Seshaiah, 2020: Analysis of wind power potential by the three-parameter Weibull distribution to install a wind turbine. *Energy Expl. & Exploitation*, **38**, 158-174.

Suomi, I., and T. Vihma, 2018: Wind gust measurement techniques—From traditional anemometry to new possibilities. *Sensors*, **18**, 27 pp.

Teunissen, P. J., and A. Kleusberg, 2012: *GPS for Geodesy*. Springer Science & Business Media, 650 pp.

Teunissen, P. J., and O. Montenbruck, 2017: *Springer Handbook of Global Navigation Satellite Systems*. Springer, 1292 pp.

Tera Analysis Ltd., 2018: QuickField: Finite Element Analysis System. User's Guide, Version 6.3.1., 248 pp.

Thrush, 2022: Thrush Aircraft. Accessed 27 December 2022. https://thrushaircraft.com/.

Tourab, W., and A. Babouri, 2016: Measurement and modeling of personal exposure to the electric and magnetic fields in the vicinity of high voltage power lines. *Safety and Health at Work*, **7**(2), 102-110.

UAS BVLOS ARC, 2022: Final Report. 381 pp., https://www.faa.gov/regulations_policies/rulemaking/committees/documents/media/UAS_BVLOS_ARC_FINAL_REPORT_03102022.pdf.

Virjoghe, E. O., D. Enescu, M. F. Stan, and C. Cobianu, 2012: Numerical determination of electric field around a high voltage electrical overhead line. *J. Sci. and Arts*, **12**(4), 487-496, http://www.josa.ro/docs/josa_2012_4/c_02_Virjoghe.pdf.

Wang, J., M. P. Stewart, and M. Tsakiri, 1998: Stochastic modeling for static GPS baseline data processing. *J. Surveying Eng.*, **124**(4), 171–181.

Wang, T., C. S. Ruf, B. Block, D. S. McKague, and S. Gleason, 2018: Design and performance of a GPS constellation power monitor system for improved CYGNSS L1B calibration. *IEEE Journal of Selected Topics in Applied Earth Observations and Remote Sensing*, **12**(1), 26–36.

Wang, B. H., D. B. Wang, Z. A. Ali, B. Ting Ting, and H. Wang, 2019: An overview of various kinds of wind effects on unmanned aerial vehicle. *Measurement and Control*, **52**, 731-739.

Wang, B., Z. A. Ali, and D. Wang, 2020: Controller for UAV to oppose different kinds of wind in the environment. *J. Control Science and Eng.*, **2020**, 10 pp.

Wieser, A., and F. K. Brunner, 2000: An extended weight model for GPS phase observations. *Earth, Planets and Space*, **52**(10), 777–782.

Yan, B. W., Q. S. Li, P. W. Chan, Y. C. He, and Z. R. Shu, 2022: Characterising wind shear exponents in the offshore area using Lidar measurements. *Applied Ocean Res.*, **127**, 8 pp.

Yu, T., 2012: GPS Software Attacks. Association for Computing Machinery, Special Interest Group on Security, National Science Foundation (U.S.), p. 1070.

Yuan, W., C. Liu, F. Liu, S. Li, and D. W. K. Ng, 2020: Learning-based predictive beamforming for UAV communications with jittering. *IEEE Wireless Comm. Letters*, **9**, 1970-1974.

Zhang, W., Y. Ning, and C. Suo, 2019: A method based on multi-sensor data fusion for UAV safety distance diagnosis. *Electronics*, **8**(12), 21 pp.

Zioutis, C. K., A. I. Spyropoulos, A. P. Fragias, D. P. Margaris, and D. G. Papanikas, 2010: Influence of helicopter rotor wake modeling on blade airload predictions. *Int. J. Eng.*, **3**(6), 521-537.

Zioutis, X. K., A. I. Spyropoulos, D. P. Margaris, and D. G. Papanikas, 2006: Effects of helicopter rotor wake characteristics on blade airloads. *25th Int. Congress Aeronautical Sci*., 10 pp.